공학박사 학위논문

A study on enhancing the electrical properties of polymer/conductive filler composite

고분자/전도성 충진제 복합체의 전기적 성질 향상에 관한 연구

2016년 2월

서울대학교 대학원

재료공학부

박 지 권

A study on enhancing the electrical properties of polymer/conductive filler composite

지도교수 신 광 선

이 논문을 공학박사 학위논문으로 제출함

2016년 2월

서울대학교 대학원

재료공학부

박 지 권

박지권의 박사 학위논문을 인준함

2016년 2월

위 원 장 윤 재 륜 (인)

부위원장 신 광 선 (인)

위 원 서 용 석 (인)

위 원 유 웅 열 (인)

위 원 홍 상 현 (인)

Abstract
A study on enhancing the electrical properties of polymer/conductive filler composite

Jeekwon Park
School of Materials Science and Engineering
The Graduate School
Seoul National University

Recently, IT devices such as e-books, cellular phones, flat-screen TVs, and digital cameras have become thinner and integrated, and automobiles have been equipped with various electronic devices. These trends have led to issues such as electromagnetic interference and exposure of human beings to electromagnetic waves. Metallic materials have superior electrical conductivity and electromagnetic interference shielding effectiveness (EMI SE). However, they also have some disadvantages, such as their high weight and limited design options due to high material processing costs and a difficulty for complicated molding. While polymers have some advantages such as lightness and ease of processing, they usually have no electrical properties. Therefore it is very important to impart electrical conductivity and EMI shielding property to polymer/filler composites for dramatically widening the range of polymer applications.

As a method of impart the electrically conductivity to polymer, one approach is to have the polymer itself be given an electrical conductivity by providing rigid and conjugated polymer backbone. The current inherently conductive polymers are typically difficult to process owing to their poor mechanical properties, high viscosity, and high melting point. Another approach for imparting electrical

conductivity to insulating polymers is to add electrically conductive filler. One method for compositing electrically conductive filler with insulating polymer is to use metallic fillers with superior electrical conductivity, such as magnesium, aluminum, copper, nickel, silver, and stainless steel. However, except magnesium and aluminum, all these metallic fillers have much higher densities than polymer and their use increases the weight of parts. Magnesium has a low corrosion resistance and need to be treated for corrosion protection. Also for aluminum has a dense oxide layer on the surface, while it has the role of preventing corrosion and oxidation of aluminum, it has a problem of lowering the effectiveness of filler when the aluminum particles are small enough to be composited with polymer.

The most commonly used industrial method is to add carbon fillers such as graphite, carbon black, and carbon fiber (CF), to insulating polymers. Graphite and carbon black have the advantages of low cost, and high electrical conductivity; however, they requires high contents to produce conductivity, causing increase in viscosity, poor degassing behavior, and degradation of processability of the composites. CF has the advantages of high electrical conductivity, high rigidity, and high reinforcing effectiveness in fibrous shape. Similar to graphite and carbon black, they have the disadvantage that a high content of CF increases the viscosity of the composite. This lowers processability and degrades the exterior quality of the product because of CF protruding from the product surface. Carbon nano-fillers such as carbon nanotube (CNT), carbon nanofiber, graphite nanoplatelet, and graphene, are promising alternatives, which can have large effects even when present in small amounts as they have nano-scale dimensions and large specific surface areas. However, they have some limitations such as high cost, poor dispersibility in a polymer matrix due to van der Waals and Coulomb attractions, and limited adding amount due to high specific surface area. Consequently, carbon nano-fillers are significantly effective to reduce the percolation thresholds of the polymer nanocomposites, however, the conductivity values are typically less than 1

S/cm.

For imparting electrical properties to insulating polymer with maintaining the properties of the matrix as much as possible, it is very important to enhance the efficiency of conductive fillers. Therefore, It is needed to understanding the mechanism of producing the electrical properties of the conducting composites and investigate the effects of various factors on the electrical properties. Furthermore, it is also important to understand the synergistic effect and its mechanism of two kinds of fillers.

First of all, for understanding the mechanism of producing the electrical conductivity of electrically conducting polymer composites, the cause of differences in the electromagnetic interference shielding efficiency (EMI SE) of polyamide (PA)/carbon fiber (CF) and polycarbonate (PC)/CF composites at same CF content was explored. As the CF content increases, EMI SE of PA/CF continuously increases, however, that of PC/CF becomes saturated from a CF content 25 wt%. Theoretically electrical conductivity and magnetic permeability effect on EMI SE, their properties were measured. It was found that the magnetic permeability of PA/CF is similar to that of PC/CF but the electrical conductivity of PA/CF is higher than that of PC/CF at CF content over 25wt%. To identify the cause of differences in the electrical conductivity in PA/CF and PC/CF, the length and orientation structure of CF within these composites was observed. It was determined that compared to PC/CF, PA/CF has longer fiber length and more domains where the fiber orientation is random, resulting in higher electrical conductivity.

Secondly, carbon fibers (CF) and two types of carbon nanotubes (CNTs) were investigated using polyamide 6,6 (PA) as a matrix for identifying their synergistic mechanism. One type of CNT was sized with polyurethane (PU-CNT), and the other was not sized (N-CNT). When PA was compounded with each CNT separately, it was found that PU-CNT, which showed better compatibility with PA,

formed looser and larger agglomerates, resulting in better electrical conductivity as compared to N-CNT. To observe the synergistic effect of CF and CNT, PA/CF/CNT composites were examined. At a low CF content, PU-CNT produced significantly synergistic effect while N-CNT did not. However, at a high CF content, both PU-CNT and N-CNT showed synergistic effects due to the improved dispersibility of CNTs. Furthermore, the effect of PU-CNT is more 10 times of that of CF alone, while the effect of N-CNT is just three times of that of CF alone, indicating that the size of CNT agglomerates is also important for synergistic effect. From these results, it is concluded that the two mechanisms producing the synergistic effect of CF and CNT are the formation of a co-supporting network of CNT/CF and the dispersion of CNT by CF.

Lastly, a new method of polymer/low-melting-point metal alloy (LMA)/elongated light metal composite fabrication is proposed to solve problems of polymer/metal composites. The first step is mixing light metal powders with LMA at a temperature above the melting point of the LMA. The second step is cold extrusion of the LMA/light metal powders to fabricate LMA/elongated light metal. Thus, the metal filler with the density of ~4.5 g/cm^3 was obtained. The last step is compounding a polymer with the LMA/elongated light metal at the processing temperature of the polymer above the melting points of the LMA. The effects of the length and the cross-sectional shape of the elongated light metal on the morphology of the LMA/elongated light metal in the polymer matrix were studied, as were electrical conductivities and mechanical properties of the composites. As the length and/or the cross-sectional aspect ratio of the elongated light metal was increased, the domains of LMA/elongated light metal formed more networks so that the electrical conductivity increased, and specific surface area of LMA/elongated light metal increased so that notched Izod impact strength was improved. Thus, the polymer/LMA/elongated light metal composites were fabricated without degrading processability even at 60 vol% metal filler loading

and the electrical conductivities over 10^3 S/cm were achieved.

In this study, the effects of various factors on the electrical properties of the electrical conductive composites were investigated and the synergistic mechanisms of two kinds of fillers were identified. On the basis of these results, a new filler system was proposed, and the electrical conductive polymer composite can be fabricated with enhancement of the electrical and mechanical properties without degrading the processability of the composites.

Keywords: polymer, filler, carbon fiber, carbon nanotube, low melting alloy, light metal fiber, electrical conductivity, electromagnetic shielding

Student Number: 2012-30160

Contents

Chapter 1 Introduction 1

1.1 Composites 1

1.1.1 Definition and classification 1

1.1.2 Electrically conductive reinforcements 6

1.2 Electrical conductivity of composites 12

1.2.1 Percolation theory 12

1.2.2 Models for conducting polymer composites 16

1.3 Electromagnetic interference shielding efficiency 23

1.3.1 Electromagnetic wave 23

1.3.2 Electromagnetic interference shielding mechanism 25

1.3.3 Measurement of electromagnetic interference shielding 29

1.4 Research objectives 32

Bibliography 33

Chapter 2 Polymer/carbon fiber system 37

2.1 Introduction 37

2.2 Experimental 38

2.2.1 Materials 38

2.2.2 Preparation of composite samples 38

2.2.3 Measurements 40

2.3 Results and Discussion 42

2.3.1 Electrical properties of the polymer/CF composites 42

2.3.2 Fiber length and fiber orientation structure in the polymer/CF composites 47

2.4 Conclusions 65
Bibliography 66

Chapter 3 Polymer/carbon nanotube/carbon fiber system.. 68

3.1 Introduction 68
3.2 Experimental 71
3.2.1 Materials 71
3.2.2 Preparation of composite samples 73
3.2.3 Measurements 75
3.3 Results and Discussion 76
3.3.1 Individual effect of CF and CNT 76
3.3.2 Enhancement of the filler efficiency of CF and CNT 84
3.4 Conclusions 94
Bibliography 95

Chapter 4 Polymer/metal filler system 98

4.1 Introduction 98
4.2 Experimental 100
4.2.1 Material selection 100
4.2.2 Preparation of composite samples 106
4.2.3 Measurements 110
4.3 Results and Discussion 113
4.3.1 Max torque during compounding of SAN/Sn-Zn30/Al fiber composites 113

4.3.2 Morphology of LMA/Al fiber in the SAN matrix 115
4.3.3 Electrical properties 125
4.3.4 Mechanical properties 129
4.4 Conclusions 133
Bibliography 134

Chapter 5 Conclusions 137

List of Tables

Table 1.1. Electrically conductive fillers, their merits and demerits 11

Table 1.2. Probability of Cluster Formation in Two- and Three-Dimensional Lattices..... 15

Table 1.3. The models predicting the electrical conductivity. 22

Table 2.1. Electrical properties of PA/CF composites; cal. Represents calculated data obtained using Equations (10-11) 49

Table 2.2. Electrical properties of PC/CF composites; cal. represents calculated data obtained using Equations (10-11) 50

Table 3.1. Percolation parameters of PA/CNT and PA/CF composites. 79

Table 4.1. Processing conditions and densities of the metal fillers prepared. 108

List of Figures

Figure 1.1. Classification of composites according to the matrix materials 3

Figure 1.2. Classification of composites according to the reinforcements 5

Figure 1.3. Dependence of electrical conductivity on filler content 13

Figure 1.4. Schematic representation of three different patterns of contact between fibers: (a) body-to-body, (b) body-to-end, (c) end-to-end. 20

Figure 1.5. Schematic representation of three different types of contact area between fibers: (a) fibers are separated by a thin layer of matrix; (b) fibers have a contact at a single point; and (c) fibers have a flat circle of contact. 21

Figure 1.6. Electromagnetic wave..... 24

Figure 1.7. Schematic showing shielding in conductive plate 27

Figure 1.8. Set-up for electromagnetic shielding efficiency measurement..... 30

Figure 1.9. Specimen for electromagnetic shielding efficiency measurement..... 31

Figure 2.1. Specimens for properties evaluation (a) EMI SE (b) magnetic permeability (c) electrical conductivity 39

Figure 2.2. EMI SE at 1 GHz of PA/CF and PC/CF composites 43

Figure 2.3. Electrical conductivity of PA/CF and PC/CF composites. 45

Figure 2.4. Relative complex magnetic permeability of PA/CF and PC/CF composites: (a) real part and imaginary part, (b) absolute value…..... 46

Figure 2.5. EMI SE (solid line) of composites to SEA (dashed line) and SER (dotted line) at 1 GHz calculated by Equations (10-11): (a) PA/CF, (b) PC/CF. 48

Figure 2.6. Average length of residual fibers in PA/CF and PC/CF composites..... 51

Figure 2.7. Steady shear viscosity of the PA/CF and PC/CF composites 52

Figure 2.8. Cross-sectional SEM images along flow direction: (a) overall view of PA/CF with 35 wt% CF, (b) overall view of PC/CF with 35 wt% CF, (c) core area of PA/CF with 35 wt% CF, (d) skin area of PA/CF

with 35 wt% CF 54
Figure 2.9. Cross-sectional micro-CT image along flow direction 55
Figure 2.10. Micro-CT images according to the distance from the surface of PA/CF 35 wt% 56
Figure 2.11. OM images of the polished surface according to the distance from the surface of PA/CF 35 wt%. 57
Figure 2.12. OM images of the polished surface according to the distance from the surface of PC/CF 35 wt%. 58
Figure 2.13. Orientation function for fibers in PA/CF and PC/CF composites as a function of normalized thickness: (a) 5 wt% CF, (b) 15 wt% CF, (c) 25 wt% CF, (d) 35 wt% CF, (e) 45 wt% CF. 60
Figure 2.14. Thickness corresponding to orientation function values between -0.5 and 0.5 for residual fibers in PA/CF and PC/CF composites..... ...64
Figure 3.1. SEM images of CNTs: (a) PU-CNT, (b) N-CNT. 72
Figure 3.2. Specimens for properties evaluation (a) EMI SE (b) electrical conductivity (c) notched Izod impact strength (d) tensile strength 74
Figure 3.3. (a) Electrical conductivity of PA/CF composites, (b) a log–log plot for electrical conductivity of PA/CF composites as a function of ($p–p_c$) with fit line determined using Equation (1). 77
Figure 3.4. (a) Electrical conductivity of PA/CNT composites, (b) a log–log plot for electrical conductivity of PA/CNT composites as a function of ($p–p_c$) with fit line determined using Equation (1). 78
Figure 3.5. TEM images of PA/CNT composites: (a) PA/PU-CNT 0.5 wt%, (b) at high magnitude, (c) PA/PU-CNT 1.0 wt%, (d) at high magnitude..... 82
Figure 3.6. TEM images of PA/CNT composites: (a) PA/N-CNT 0.5 wt%, (b) at high magnitude, (c) PA/N-CNT 1.0 wt%, (d) at high magnitude 83
Figure 3.7. Electrical conductivity of PA/CF/CNT composites: (a) at overall filler content, (b) at CF 5–15 wt%, (c) at CF 25–35 wt%. 85

Figure 3.8. EMI shielding efficiency at 1GHz of PA/CF/CNT composites: (a) at overall filler content, (b) at CF 5–15 wt%, (c) at CF 25–35 wt%. 86
Figure 3.9. SEM images of factured surface of PA/CF 5 wt%/CNT 1.0 wt% composites: at low magnitude (a) PU-CNT, (b) N-CNT, at medium magnitude (c) PU-CNT, (d) N-CNT, at high magnitude (e) PU-CNT, (f) N-CNT.....87
Figure 3.10. SEM images of the fractured surface of PA/CF 25 wt%/CNT 1.0 wt% composites: at low magnitude (a) PU-CNT, (b) N-CNT, at high magnitude (c) PU-CNT, (d) N-CNT. 88
Figure 3.11. Optical microscopy images of PA/CF/CNT composites: at CF 5 wt% (a) PU-CNT 1.0 wt%, (b) N-CNT 1.0 wt%, at CF 25 wt% (c) PU-CNT 1.0 wt%, (d) N-CNT 1.0 wt%.....90
Figure 3.12. Schematic picture for the mechanism of the synergistic effect of CF and CNT.....91
Figure 3.13. The tensile strength of PA/CF/CNT composites; (a) CF 5 wt%, (b) CF 25 wt%.....92
Figure 3.14. The notched Izod impact Strength of PA/CF/CNT composites; (a) CF 5 wt%, (b) CF 25 wt%. 93
Figure 4.1. The technological process of preparing polymer/LMA/elongated light metal composite.....101
Figure 4.2. (a) Phase diagram of metal alloy, (b) viscosities of ① pure metal and ② metal alloy as a function of temperature. 103
Figure 4.3. (a) Phase diagram of Sn-Zn, (b) phase fraction plot of Sn-Zn30 as a function of temperature. 104
Figure 4.4. Mixture after 10 min mixing under 50 rpm stirring: (a) pure tin and aluminum powder, (b) Sn-Zn30 and aluminum powder.....105
Figure 4.5. Extrusion dies: (a) circle (10), (b) circle (25), (c) rectangular (25). ...107
Figure 4.6. Aluminum (green color) EDS mapping results of extruded Sn-

Zn30/elongated Al (red arrow is the direction of observation in inner picture); (a) C10, (b) C25, (c-d) R25.....109
Figure 4.7. Specimens for properties evaluation (a) EMI SE (b) electrical conductivity (c) notched Izod impact strength (d) flexural modulus.....111
Figure 4.8. Max torque of the Hakke mixer during compounding of the SAN/Sn-Zn30/elongated Al composites. 114
Figure 4.9. SEM and EDS mapping images of SAN/C10 20 vol%; (a) SEM image, (b) ESD image of mixed elements, (c) Al, (d) Zn,(e) Sn.....116
Figure 4.10. SEM and EDS mapping images of SAN/C25 20 vol%; (a) SEM image, (b) ESD image of mixed elements, (c) Al, (d) Zn,(e) Sn.....117
Figure 4.11. SEM and EDS mapping images of SAN/R25 20 vol%; (a) SEM image, (b) ESD image of mixed elements, (c) Al, (d) Zn,(e) Sn.....118
Figure 4.12. SEM and EDS mapping images of SAN/C10 40 vol%; (a) SEM image, (b) ESD image of mixed elements, (c) Al, (d) Zn,(e) Sn.....119
Figure 4.13. SEM and EDS mapping images of SAN/C25 40 vol%; (a) SEM image, (b) ESD image of mixed elements, (c) Al, (d) Zn,(e) Sn.....120
Figure 4.14. SEM and EDS mapping images of SAN/R25 40 vol%; (a) SEM image, (b) ESD image of mixed elements, (c) Al, (d) Zn,(e) Sn.....121
Figure 4.15. SEM and EDS mapping images of SAN/C10 60 vol%; (a) SEM image, (b) ESD image of mixed elements, (c) Al, (d) Zn,(e) Sn.....122
Figure 4.16. SEM and EDS mapping images of SAN/C25 60 vol%; (a) SEM image, (b) ESD image of mixed elements, (c) Al, (d) Zn,(e) Sn.....123
Figure 4.17. SEM and EDS mapping images of SAN/R25 60 vol%; (a) SEM image, (b) ESD image of mixed elements, (c) Al, (d) Zn,(e) Sn.....124
Figure 4.18. Electrical conductivity of SAN/LMA/elongated Al composites 127
Figure 4.19. EMI shielding efficiency of SAN/LMA/elongated Al composites...128
Figure 4.20. Notched Izod impact strength of the SAN/Sn-Zn30/elongated Al

composites. 130
Figure 4.21. SEM images of the fractured surfaces of composites with the metal filler content of 20 vol%; (a) SAN/C10, (b) SAN/C25, (c) SAN/R25..... 131
Figure 4.22. Flexural modulus of the SAN/Sn-Zn30/elongated Al composites.... 132

Chapter 1. Introduction

1.1 Composites

1.1.1 Definition and classification

A composite is a material having two or more distinct constituents or phases [1]. The constituent that is continuous and is often but not always, present in the greater quantity in the composite is termed the matrix. The second constituent is referred to as the reinforcing phase, reinforcement, or filler as it enhances or reinforces the physical and/or chemical properties of the matrix. On the base of this definition, we can easily find composites from the ancient age. The earliest man-made composite materials were straw and mud combined to form bricks for building construction. Ancient brick-making was documented by Egyptian tomb paintings. Wattle and daub is one of the oldest man-made composite materials, at over 6000 years old [2]. Concrete is also a composite material, and is used more than any other man-made material in the world. Modern composite materials evolves from the simplest mixtures of two or more materials to obtain a property that was not there before. The three key historical steps leading to modern composites are the commercial availability of fibreglass filaments in 1935, the development of strong aramid, glass, and carbon fibers in the late 1960s, and the promulgation of analytical methods for structures made from these fibers [3]. These composites have many advantages such as weight reduction (high strength- or stiffness-to-weight ratio), tailorable properties (strength of stiffness can be tailored to be in the load direction), redundant load paths (fiber to fiber), longer life (no corrosion), lower manufacturing costs because of lower part count, inherent damping, and increased (or decreased) thermal or electric conductivity. However,

the composites also have disadvantages such as cost of raw materials and fabrication, possible weakness of transverse properties, weak matrix and low toughness, environmental degradation of matrix, difficulty in attaching, and difficulty with analysis. Therefore, it is necessary to understand the physical and chemical properties of materials, the compositing processes, and the advantages and disadvantages of compositing them.

For understanding composites, the major classes of composites that exist today can be categorized from two points of view, matrix and reinforcements. According to the matrix materials, the composites can be classified as polymer matrix composites (PMCs), metal matrix composites (MMCs), ceramic matrix composites (CMSs), and carbon-carbon composites (CCCs) as can be seen in Figure 1.1 [3].

(1) Polymer matrix composites (PMCs)

PMCs are the most developed class of composite materials in that they have found widespread application, can be fabricated into large, complex shapes, and have been accepted in a variety of aerospace and commercial applications. They are constructed of components such as glass fiber or graphite bound together by an organic polymer matrix. These reinforced plastics are a synergistic combination of high-performance reinforcements and matrices.

(2) Metal matrix composites (MMCs)

MMCs consist of metal alloys reinforced with continuous fibers, whiskers (a version of short fibers that are in the form of single crystals), or particulates (fine particles, as distinct from fibers). Because of their use of metals as matrix materials, they have a higher temperature resistance than PMCs but in general are heavier. They are not as widely used as PMCs but are finding increasing application in many areas.

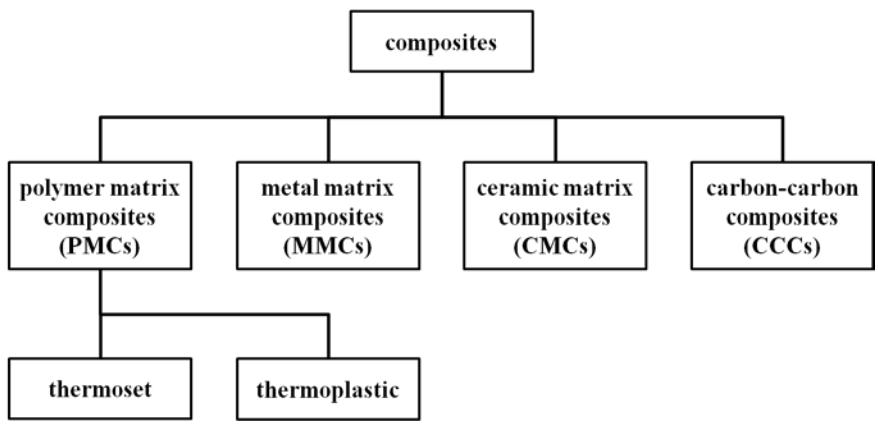

Figure 1.1. Classification of composites according to the matrix materials.

(3) Ceramic matrix composites (CMCs)

Monolithic ceramic materials have a natural high-temperature resistance but also have fundamental limitations in structural applications owing to their propensity for brittle fracture. The incorporation of a reinforcement, for example, ceramic fiber reinforcement, into the ceramic matrix can improve the forgivability of the material by allowing cracking to be retarded by the fiber-matrix interfaces. CMSs are a class of structural materials with reinforcements such as SiC fibers embedded in a ceramic matrix such as Al_2O_3, Si_3N_4 or SiC. The reinforcements can be continuous fibers, chopped fibers, small discontinuous whisker platelets, or particulates. They have the potential for high-temperature application above 1649℃.

(4) Carbon-carbon composites (CCCs)

CCCs consist of carbon reinforcements embedded in a carbonaceous matrix. Preliminary processing is very much like that for PMCs, but the organic matrix is subsequently heated up to the point where it is converted to carbon. Carbon-carbon is a superior structural material for applications where resistance to very high temperatures and thermal shock is required. No other material has higher specific strength properties (strength-to-density ratio) at temperatures in excess of 1371℃.

Figure 1.2 represents a classification scheme for composites according to the reinforcements [1]. The geometry of the reinforcing phase is one of the major parameters in determining the effectiveness of the reinforcements; in other words, the properties of composites are a function of the shape and dimensions of the reinforcement. We usually describe the reinforcement as being either fiber or particulate.

Particulate reinforcements have dimensions that are approximately equal in all directions. The shape of the reinforcing particles may be spherical, cubic, platelet

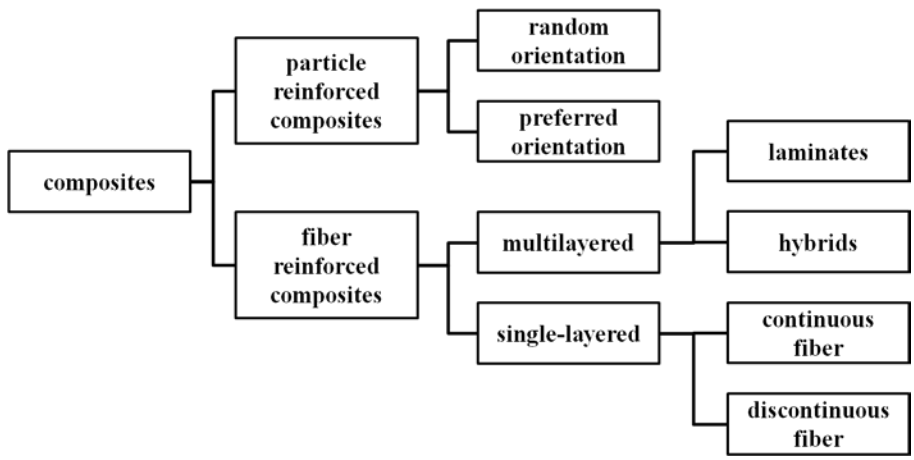

Figure 1.2. Classification of composites according to the reinforcements.

or any regular or irregular geometry. The arrangement of the particulate reinforcement may be random or with a preferred orientation, and this characteristics is also used as a part of the classification shceme.

A fibrous reinforcement is characterized by its length being much greater than its cross-sectional dimension. However, the ratio of length to the diameter, known as the aspect ratio, can vary considerably. In single-layered composites long fibers with high aspect ratios give what are called continuous fiber reinforced composites, whereas discontinuous fiber composites are fabricated using short fibers of low aspect ratio.

Multilayered composites are another category of fiber reinforced composites. These are classified either laminates or hybrids. Laminates are sheet constructions which are made by stacking layers in a specified sequence. Hybrids are usually multilayered composites with mixed fibers and are becoming commonplace. The fibers may be mixed in a ply or layer by layer and these composites are designed to benefit from the different properties of the fibers employed.

1.1.2 Electrically conductive reinforcements

A lot of materials can be used as reinforcements (or fillers) if they have a particular property for a targeted application and no drawback in compositing process. Therefore, I focus on electrically conducting polymer composites and cover electrically conductive fillers that attract attentions recently from both scientific and engineering points of view. The broad classification of fillers used to increase the conductivity of the polymers are carbon based materials that include carbon black (CB), graphite, graphite nanoplatelet (GNP), graphene, carbon fiber (CF), carbon nanofiber (CNF), carbon nanotube (CNT), and metals such as copper flakes and fibers, silver flakes, nickel flakes, stainless steel fibers, aluminum fibers, flakes, and powder.

(1) Carbon black (CB)

Carbon black (CB), a particulate form of carbon is widely used in tires, elastomers (rubber), plastics, inks, and paint. In plastics, carbon black is used as a colorant, as a stabilizer to protect the polymer from UV radiation, as reinforcement, and to improve the electrical conductivity of the material [4]. The typical electrical resistivity of carbon black is about 10^{-2}-10^{-3} Ωcm and may vary depending on the morphology, particle size, and preparation conditions. CBs having smaller aggregates, higher structures, and less volatiles are good for their use as filler in a conductive polymer composite. Carbon black particles with larger surface area and high degree of branching (allowing it to contact a larger amount of polymer) can impart good electrical conductivity in composites.

(2) Graphite

Synthetic graphite has got a variety of applications in drilling, coatings, foundry, and fuel cell bipolar plates and more importantly as conductive fillers in rubber and plastic compounds [5]. It can be produced by using a high temperature treatment on carbon materials such as calcined petroleum coke and coal tar pitches which contain highly graphitizable forms of carbon. Several steps involved are mixing, molding, and baking operations before being heat-treated at high temperatures (2,500–3,000℃). The high temperature vaporizes the volatile impurities, yielding a product of high purity
(99% or more), high thermal conductivity, and low electrical resistivity (10^{-5}-10^{-6} Ωcm).

(3) Graphite nanoplatelet (GNP)

Natural flakes of graphite can be exfoliated to obtain graphite nanoplatelet (GNP), with thickness as low as few nanometers. GNP is a cost effective,

lightweight alternative to metals and carbon-based electrically conductive fillers (CNT and CNF). Graphite does not bear any net charge and thus is different from silicate clay minerals. In its natural form, no reactive ion groups exist on the graphene layers and as a result, it is impossible to intercalate monomers into the graphite galleries by ion exchange reactions as is possible for the layered silicates. However, graphite is readily intercalated and can host various atoms, molecules, metal complexes and salts between the expanded graphene sheets to form graphite intercalation compounds (GICs). So far, GNPs are mainly obtained from sulfuric acid-intercalated graphite and graphene oxide (GO) [6]. GNP has low electrical resistivity (10^{-5}-10^{-6} Ωcm) similar to that of graphite.

(4) Graphene

The crystal lattice of graphite consists of stacks of parallel two dimensional graphene sheets [6]. Graphene sheets are basically the single carbon layer stacked up in graphite structure carbon atoms tightly bonded with each other in hexagonal ring forms. Five routes are available for the preparation of graphene. The first involves chemical vapor deposition (CVD) of monolayer of graphite on transition metal surfaces. The second route is the micromechanical exfoliation of graphite and involves peeling of the graphene from graphite using “Scotch” tape. The “Scotch” tape is then dipped in acetone to release the graphene which are subsequently captured on a silicon wafer with a SiO2 layer on top. The third route involves the epitaxial growth of graphene on electrically insulating substrates like silicon carbide. However, the second and third methods are unsuitable for large scale preparation of graphene for the fabrication of polymer nanocomposites. Chemical reduction of GO present in the colloidal suspension with reducing agents like hydrazine or hydrazine derivatives is necessary to convert the electrically insulating GO layers back to conducting graphene which are suitable for composite applications. The final route by which bulk quantities of graphene can be prepared

is by thermally reducing GO. Due to the zero density of states at the Dirac points, electronic conductivity is actually quite low. However, the Fermi level can be changed by doping (with electrons or holes) to create a material that is potentially better at conducting electricity.

(5) Carbon fiber (CF)

CF is a pure form of carbon (>90 wt%) wherein all the C-atoms are arranged in sheets of hexagonal rings. It can be obtained by the pyrolysis of suitable precursor materials such as polyacrylonitrile (PAN) and petroleum pitch. It is an attractive reinforcing material due to its greater specific strength and specific modulus with a low linear coefficient of thermal expansion [5]. CF has low electrical resistivity (10^{-3}-10^{-4} Ωcm)

(6) Carbon nanofiber (CNF)

CNFs are hollow fibers with one of the dimensions in the nanometer scale. They are made by the catalytic decomposition of hydrocarbon gases or carbon monoxide over metal particles such as nickel, cobalt, iron, at temperatures above the range of 1000℃±6400℃ [7]. The diameters of these nanofibers vary between 50 and 300 nm with electrical resistivity values as good as metals (10^{-5}-10^{-6} Ωcm).

(7) Carbon nanotube (CNT)

Carbon nanotubes (single walled and multiwalled) are hollow tubes made from sheets of graphite. They are used in multiple applications and in polymers they are mainly used to increase electrical conductivity and improve the mechanical properties. Owing to their high electrical conductivity (10^{-5}-10^{-6} Ωcm) and large surface area, carbon nanotubes (CNTs) are better than conventional fillers for polymer composites [6]. The disadvantage is that the CNTs have a higher cost compared to conventional fillers . Reinforcement of CNT in polymer matrix can

improve electrical conductivity as well as the mechanical properties of the composite at a relatively lower level of loading that is unlikely to other fillers.

(8) Metal fillers

Metal fillers, which are good electrically conductive materials, can be used as conductive filler as well (< 10^{-6} Ωcm). For metal fillers, there are magnesium, aluminum, nickel, copper, silver and stainless steel, etc [8-10]. These metal fillers, except for magnesium and aluminum, tend to increase the overall weight of composites due to their high densities, and they also yield a poor processability when large amounts are added. Magnesium has a low corrosion resistance and need to be treated for corrosion protection [11]. In the case of aluminum, a dense oxidation layer formed on the surface increases the electrical resistivity of the composite [12].

Table 1.1 summarizes the electrical resistance, density, merit, and demerit of electrically conductive fillers that can be used for electrically conducting polymer composites.

Table 1.1. Electrically conductive fillers, their merits and demerits

	Merit	Demerit
CB ($2.1\ g/cm^3$, 10^{-2}-$10^{-3}\ \Omega cm$)	Having smaller aggregates, higher structures, and less volatiles, relatively cheaper	High percolation threshold (requires high filler loading), at high loading particles tend to slough
Graphite ($2.3\ g/cm^3$, 10^{-5}-$10^{-6}\ \Omega cm$)	Lightweight alternative to metal, CNT and CNF; relatively cost-effective	Poor filler matrix adhesion
Graphene ($1.7\ g/cm^3$,)	Excellent electrical properties	Very expensive
CF ($1.8\ g/cm^3$, 10^{-3}-$10^{-4}\ \Omega cm$)	High strength and modulus, low linear coefficient of thermal expansion, lighter than steel	Bundling and debonding effects, poor dispersion and distribution
CNF ($2.0\ g/cm^3$, 10^{-5}-$10^{-6}\ \Omega cm$)	Improved electrical conductivity at a relatively lower level of loading (low percolation threshold)	Dispersion and distribution difficulties, agglomerates, higher cost compared to conventional fillers
CNT ($1.8\ g/cm^3$, 10^{-5}-$10^{-6}\ \Omega cm$)	Low percolation threshold, unlike other fillers, improve the mechanical properties of the composite	Dispersion and distribution difficulties, agglomerates, quite expensive
Metal (7-$8\ g/cm^3$, $< 10^{-6}\ \Omega cm$) except light metal	Least electrically resistant material; ideal choice as conductive filler	Processing at high filler loading is challenging due to their high density and poor dispersion; formation of non conductive oxide layers that reduce the electrical conductivity

1.2 Electrical conductivity of composites

The modeling of the electrical properties of electrically conducting polymer composites provides insights into the important factors, which control their electrical behavior. In this section, many existing models and theories for electrical conductivity prediction, including their fundamental concepts and the relevant equations are dealt with.

1.2.1 Percolation theory

To understand the concept of electrical conductivity in a composite, it is important to comprehend the theory of percolation and percolation threshold. The percolation threshold is the point where there are enough fillers in the composite to start forming conductive networks. These conductive networks form a continuous path that allows electricity to pass easily through a composite, thus increasing the electrical conductivity. The formation of conductive network can be explained in terms of percolation theory. The electrical conductivity in a composite system is dependent on the amount of conductive filler used. To explain the conductivity of blends, several models have been proposed based on the factors such as the specific conductivity of the filler particles, volume fraction of the conductive phase, the probability of the development of at least a one-dimensional conductive network and the interfacial interactions at the boundary between the individual filler particles and the polymeric matrix. However, no such model exists that may explain all of the different results of experimental studies. Moreover, these models do not account for the influence of different processing parameters on percolation phenomena.

There are three stages of electrical conductivity as illustrated in Figure 1.3. At low filler concentrations, filler particles act like conductive islands in the sea of

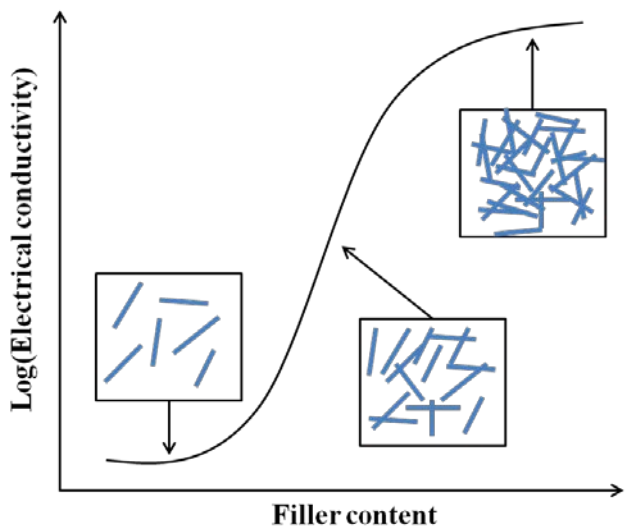

Figure 1.3. Dependence of electrical conductivity on filler content.

electrically insulating polymer matrix. The electrical conductivity of composite at this stage is close to that of the polymer matrix used in the composite. Upon further introduction of fillers, the conductive particles become more crowded and are more likely to come in contact with each other. At a critical volume concentration, known as the percolation threshold, most of the filler particles get in contact with their neighboring particles, thereby forming a conductive bridges or continuous network. An electrical charge now can flow without encountering the high resistance of the polymer.

At percolation threshold, the electrical conductivity of the composite will increase rapidly with only a small change in the amount of filler as a result of threshold conductive bridges being formed in the composites. After the percolation threshold has been reached the electrical conductivity will flatten and approach the electrical conductivity of the fillers used in the composite.

The essence of percolation theory is to determine how a given set of sites, regularly or randomly positioned in some space, is interconnected [13]. Inherent to the theory is the fact that at some critical probability, called the percolation threshold, a connected network of sites is formed which spans the sample, causing the system to "percolate." In 1957, Broadbent and Hammersley [14] introduced the term "percolation theory" and used a geometrical and statistical approach to solve the problem of fluid flow through a static random medium. Initial work focused on the determination of the percolation thresholds in simple two and three-dimensional geometries. Two types of percolation were considered: site percolation, where sites in a lattice are either filled or empty, or bond percolation, where all the sites in a lattice are occupied, but are either connected or not. Table 1.2 presents calculated values of the percolation threshold for different lattices [15].

The percolation theory has been used to interpret the behavior in a mixture of conducting and nonconducting components [16]. The sudden transition in such materials from insulator to conductor is evidence of a percolation threshold.

Table 1.2. Probability of Cluster Formation in Two- and Three-Dimensional Lattices.

Dimension	Lattice	Site percolation threshold	Bond percolation threshold
2	Honeycomb	0.6962	0.65271
	Square	0.59275	0.50000
	Triangular	0.50000	0.34729
3	Simple cubic	0.3117	0.2492
	Body-centered cubic	0.2450	0.1785
	Face-centered cubic	0.1980	0.1190

A simple power law describes the relation between composite conductivity and conductive filler concentration in the vicinity of the percolation threshold:

$$\sigma_c = \sigma_f(p - p_c)^t \quad (1)$$

where σ_c is the electrical conductivity of the composite, σ_f is the electrical conductivity of the filler, p is the volume fraction of the filler, p_c is the percolation threshold and t is a critical exponent related to the dimensionality of the system. This equation is valid at concentrations above the percolation threshold, i.e., when $p > p_c$. The value of the critical exponent, t is dependent on the dimensions of the lattice: t is approximately 1.3 in two dimensional system and t is approximately 2 in three dimensional system.

1.2.2 Models for conducting polymer composites

(1) Nielsen model

Equations similar to those used to estimate the elastic modulus of composites were extended to calculate the electrical and thermal conductivities of two phase systems [17]. The electrical conductivity, σ_c, is defined as

$$\sigma_c = \sigma_m \left[\frac{1+ABp}{1-Bp}\right] \quad (2)$$

where

$$B = \frac{\frac{\sigma_f}{\sigma_m}-1}{\frac{\sigma_f}{\sigma_m}+A} \quad (3)$$

$$\psi = 1 + \left(\frac{1-p_{max}}{p_{max}^2}\right)p \quad (4)$$

and A is a function of the aspect ratio of the particles. σ_m is the electrical conductivity of matrix. For polymer composite systems, B is essentially equal to 1. The ψ term can be calculated by knowing the maximum packing fraction of particles, while A is found from tabulated values. p_{max} is maximum packing fraction of particles.

(2) McCullough Model

A generalized combining rule for transport properties was modified for application to percolation transport mechanisms [18]. The equation predicts the composite conductivity in either the longitudinal, transverse, or normal directions. It has the following form:

$$\sigma_{ci} = p\sigma_f + (1-p)\sigma_m - \left[\frac{\lambda_i p(1-p)(\sigma_f-\sigma_m)^2}{V_{fi}p+V_{mi}\sigma_m}\right] \quad (5)$$

where V_{fi} and V_{mi} are defined as

$$V_{fi} = (1-\lambda_i)p + \lambda_i(1-p) \quad (6)$$

$$V_{mi} = \lambda_i p + (1-\lambda_i)(1-p) \quad (7)$$

The λ_i term is a chain length factor which is dependenton the aspect ratio of the particles.

(3) Effective medium theory

The effective medium theory replaces the inhomogeneous medium found in an actual composite with a homogeneous "effective" medium. For a conductive composite, the original lattice consisting of randomly distributed conductances is replaced by a lattice of similar symmetry but where the conductances are regularly placed so that the electrical properties are, on average, identical for each situation [19]. Taya and Ueda [20] proposed the following formula for the electrical conductivity:

$$\sigma_c = \sigma_m\left[1 + \frac{p(\sigma_f-\sigma_m)[(S_{11}+S_{33})(\sigma_f-\sigma_m)+2\sigma_m]}{2(\sigma_f-\sigma_m)^2(1-p)S_{11}S_{33}+ \sigma_m(\sigma_f-\sigma_m)(2-p)(S_{11}-S_{33})}\right] \quad (8)$$

For fiber composites:

$$S_{11} = \frac{ld^2}{2(l^2-d^2)^{3/2}}\left[\frac{l}{d}\left(\frac{l^2}{d^2}-1\right)^{1/2} - cosh^{-1}\frac{l}{d}\right] \quad (9)$$

$$S_{22} = S_{11} \tag{10}$$

$$S_{33} = 1 - 2S_{22} \tag{11}$$

where *1* is fiber length, *d* is fiber diameter. The model did not predict a percolation threshold and was insensitive to changes in the fiber aspect ratio.

(4) Fiber contact model

The fiber contact model of Weber and Kamal can be used for calculating the volume resistivity of fiber-reinforced composites [21]. The model is based on studies of Batchelor and O'Brien about thermal and electrical conductivities of particle-filled materials [22]. Weber and Kamal have expended the model for fiber-reinforced materials. Microstructural parameters, such as filler concentration and dimensions, aspect ratio and orientation of fibers, were taken into account. In their model, the conductivity of the matrix was estimated to be so low that it did not have any influence on the conductivity of the composites. The electrical conductivity can be defined as:

$$\sigma_c = \sigma_m + \frac{4\beta p \sigma_f d_c l \cos^2\theta}{\pi d^2 X} \tag{12}$$

where d_c is the diameter of contact area, Θ is orientation angle of fiber, β is the fraction of fiber participating in percolation cluster and 0 below the percolation threshold.

$$X = \frac{1}{0.59+0.15m} \tag{13}$$

where m is the number of fiber contacts. In the model, it is assumed that a contact between fibers is not a perfect end-to-end contact, but rather an end-to-body or body-to-body type as can be seen in Figure 1.4 [23]. The area of contact for these two latter cases is much smaller than in a perfect end-to-end alignment, which therefore thas an effect on the entire conductivity of the composite. Besides, the fiber contact model is based on the fact that the particles have a flat circle of contact in Figure 1.5 (c). The fiber can also be separated by a thin layer of matrix,

in which the conductivity increases as the gap between the fibers is reduced in Figure 1.5 (a). Therefore, this fiber-contact type is not suitable for modeling the electrical conductivity. The diameter of this contact circle d_c is obviously small and today it is not possible to measure this value accurately. The value of the contact circle d_c can be estimated by fitting the experimental data to the model calculations when using a particular d_c value for all materials with different fiber loadings.

These models are summarized with regard to factors for the electrical conductivity of composites in Table 1.3.

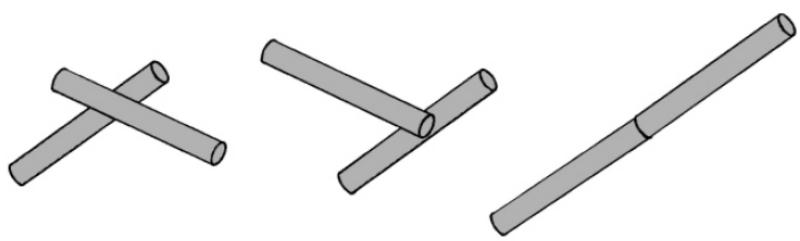

(a) (b) (c)

Figure 1.4. Schematic representation of three different patterns of contact between fibers: (a) body-to-body, (b) body-to-end, (c) end-to-end [23].

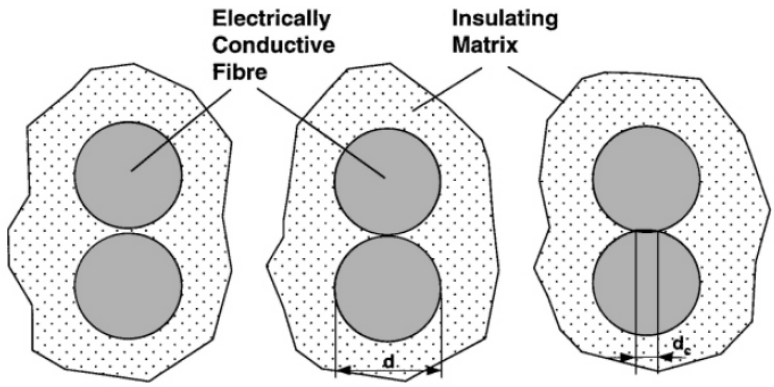

(a) (b) (c)

Figure 1.5. Schematic representation of three different types of contact area between fibers: (a) fibers are separated by a thin layer of matrix; (b) fibers have a contact at a single point; and (c) fibers have a flat circle of contact [23].

Table 1.3. The models predicting the electrical conductivity.

	Conductivity of Fillers	Volume Fraction	Aspect Ratio	Percolation Threshold	Fiber Orientation
Nielsen Model	**O**	**O**	**O**		
McCullough Model	**O**	**O**	**O**		
Effective Medium Model	**O**	**O**	**O**		
Fiber Contact Model	**O**	**O**	**O**	**O**	**O**

1.3 Electromagnetic interference shielding efficiency

1.3.1 Electromagnetic wave

Recently, IT devices such as e-books, cellular phones, flat-screen TVs, and digital cameras have become thinner and integrated, and automobiles have been equipped with various electronic devices. These trends have led to issues such as electromagnetic interference (EMI) and exposure of human beings to electromagnetic (EM) waves [24-26]. Therefore, needs for conducting polymer composite with performance of EMI shielding is significantly grow up recently.

The electromagnetic waves are synchronized oscillations of electric and magnetic fields that propagate at the speed of light through a vacuum as can be seen in Figure 1.6. The oscillations of the two fields are perpendicular to each other and perpendicular to the direction of energy and wave propagation, forming a transverse wave. Electromagnetic waves can be characterized by either the frequency or wavelength of their oscillations to form the electromagnetic spectrum, which includes, in order of increasing frequency and decreasing wavelength: radio waves, microwaves, infrared radiation, visible light, ultraviolet radiation, X-rays and gamma rays. James Clerk Maxwell first formally postulated electromagnetic waves. These were subsequently confirmed by Heinrich Hertz. Maxwell derived a wave form of the electric and magnetic equations, thus uncovering the wave-like nature of electric and magnetic fields and their symmetry.

Electromagnetic waves were predicted by the classical laws of electricity and magnetism, known as Maxwell's equations [27]. Maxwell’s equations in free space are as:

$$\nabla \cdot \mathbf{E} = 0 \tag{14}$$

$$\nabla \times \mathbf{E} = -\frac{\partial \mathbf{B}}{\partial t} \tag{15}$$

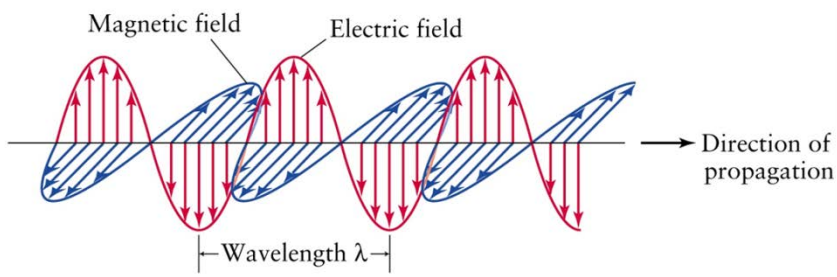

Figure 1.6. Electromagnetic wave.

$$\nabla \cdot \mathbf{B} = 0 \tag{16}$$

$$\nabla \times \mathbf{B} = \mu_0 \epsilon_0 \frac{\partial \mathbf{E}}{\partial t} \tag{17}$$

where **E** is the electric field, **B** is the magnetic field, μ_0 is the magnetic permeability in free space, ϵ_0 is the permittivity in free space. From equation (15):

$$\nabla \times (\nabla \times \mathbf{E}) = \nabla \times \left(-\frac{\partial \mathbf{B}}{\partial t}\right) \tag{18}$$

Evaluating the left hand side:

$$\nabla \times (\nabla \times \mathbf{E}) = \nabla(\nabla \cdot \mathbf{E}) - \nabla^2 \mathbf{E} = -\nabla^2 \mathbf{E} \tag{19}$$

Evaluating the right hand side:

$$\nabla \times \left(\frac{\partial \mathbf{B}}{\partial \mathrm{t}}\right) = -\frac{\partial}{\partial t}(\nabla \times \mathbf{B}) = -\mu_0 \epsilon_0 \frac{\partial^2 \mathbf{E}}{\partial t^2} \tag{20}$$

Equations (19) and (20) are equal, so this results in a vector-valued differential equation for the electric field:

$$\nabla^2 \mathbf{E} = \mu_0 \epsilon_0 \frac{\partial^2 \mathbf{E}}{\partial t^2} \tag{21}$$

Applying a similar pattern results in similar differential equation for the magnetic field:

$$\nabla^2 \mathbf{B} = \mu_0 \epsilon_0 \frac{\partial^2 \mathbf{B}}{\partial t^2} \tag{22}$$

Equations (21) and (22) are the wave equations of electromagnetic wave.

1.3.2 Electromagnetic interference shielding mechanism

Shielding effectiveness is the ratio of impinging energy to the residual energy. When an electromagnetic wave pass through a shield, absorption and reflection takes place. Residual energy is part of the remaining energy that is neither reflected nor absorbed by the shield but it is emerged out from the shield. All electromagnetic waves consist of two essential components, a magnetic field (**B**) and an electric field (**E**) as shown in Figure 1.6. These two fields are perpendicular to each other and the direction of wave propagation is at right angles to the plane

containing the two components. The relative magnitude depends upon the waveform and its source. EMI shielding consists of two regions, the near field shielding region and far field shielding region. When the distance between the radiation source and the shield is larger than $\lambda/2\pi$ (where λ is the wavelength of the source), it is in the far field shielding region. The electromagnetic plane wave theory is generally applied for EMI shielding in this region. When the distance is less than $\lambda/2\pi$, it is in the near field shielding and the theory based on the contribution of electric and magnetic dipoles is used for EMI shielding.

Shielding effectiveness (SE) is the ratio of the field before and after attenuation of electric and magnetic field and can be expressed as [28]:

$$SE = 20\log\left(\frac{E_t}{E_i}\right) \tag{23}$$

$$SE = 20\log\left(\frac{B_t}{B_i}\right) \tag{24}$$

where the subscripts t and i refer to the transmitted and incident waves.

The attenuation of an electromagnetic wave occurs by three mechanisms as shown in Figure 1.7.: Absorption (A), Reflection (R), Multiple reflection (MR). Thus shielding efficiency is the sum of all the tree terms [29]:

$$\text{EMI SE} = S_{ER} + S_{EA} + SE_{MR} \tag{25}$$

$$SE_R = 20\log\left|\frac{\eta_0}{4\eta_s}\right| \tag{26}$$

$$SE_A = 20\log\left|e^{d/\delta}\right| \tag{27}$$

$$SE_{MR} = 20\log\left|1 - e^{-2d/\delta}\right| \tag{28}$$

where SE_R represents SE due to reflection, SE_A represents SE due to absorption, and SE_{MR} represents SE due to multi-reflection. η_0 is impedance in free space and η_s is impedance of the shielding material. d is the width of the medium and δ is skin depth and is shown in Equation (29):

$$\delta = \frac{1}{\sqrt{\pi f \mu \sigma}} \tag{29}$$

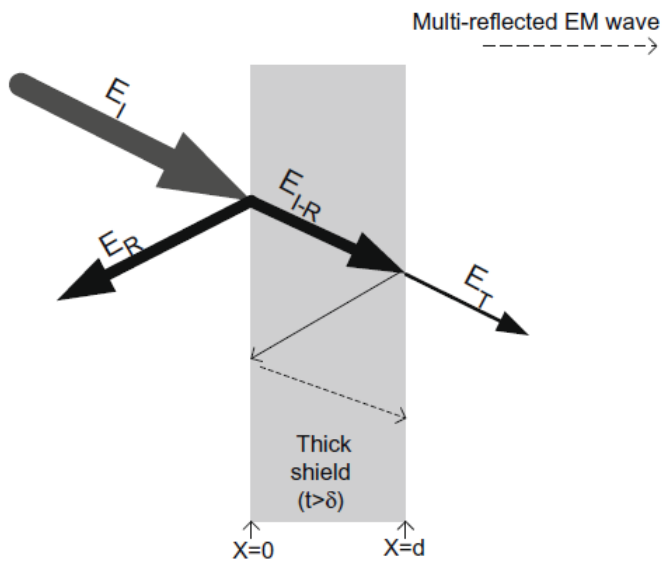

Figure 1.7. Schematic showing shielding in conductive plate [29].

where f is the EM wave frequency, μ is the magnetic permeability of the medium, and σ is the electrical conductivity of the medium. Impedance can be considered to be given by Equation (30):

$$\eta = \frac{|\mathbf{E}|}{|\mathbf{B}|} = \sqrt{\frac{j\omega\mu}{\sigma + j\omega\epsilon}} \tag{30}$$

where |E| is the electric field amplitude and |H| is the magnetic field amplitude. ω is the angular frequency of EM wave and ϵ is the permittivity of the medium. σ is 0 on EM wave in free space; therefore, η_0 is given by Equation (31):

$$\eta_0 = \sqrt{\frac{\mu_0}{\epsilon_0}} = 337\ \Omega \tag{31}$$

where μ_0 is the magnetic permeability in free space (1.26×10^{-6} H/m) and ϵ_0 is the permittivity in free space (8.85×10^{-12} F/m). For an electrically conductive material, $\sigma >> \omega\epsilon$; this relation results in Equation (32) given below:

$$\eta_S = \sqrt{\frac{j\omega\mu}{\sigma}} \tag{32}$$

If the width of the shielding material is amply greater than the skin depth, the contribution due to multi-reflection can be ignored. Then, substituting Equations (29), (30), and (32) into Equations (26) and (27), contributions such as those given by Equations (33) and (34) contribute to EMI SE.

$$SE_R = 39.5 + 10\log\left|\frac{\sigma}{2\pi f j\mu}\right| \tag{33}$$

$$SE_A = 8.7d\left|\sqrt{\pi f\mu\sigma}\right| \tag{34}$$

As can be seen from Equations (33) and (34), Electrical conductivity and magnetic permeability effect on EMI SE. When electrical conductivity increases, both SE_R and SE_A increase, however when magnetic permeability increase, SE_R decreases and SE_A increases.

1.3.3 Measurement of electromagnetic interference shielding

According to ASTM D4935-10 specification a coaxial transmission line test method is utilized for measuring the EMI shielding effectiveness [30]. The test system is illustrated in Fig. 1.8 [31], which is consisted of a shielding effectiveness tester. Circular test specimens molded by center gate with 133 mm in diameter are needed to be prepared according to ASTM D4935-10 specification as shown in Fig. 1.9. SE is usually expressed in decibels (dB) by the following equation:

$$SE = 10\log\frac{P_1}{P_2} \tag{35}$$

where P_1 is the received power with the material present, P_2 is the received power without the material present.

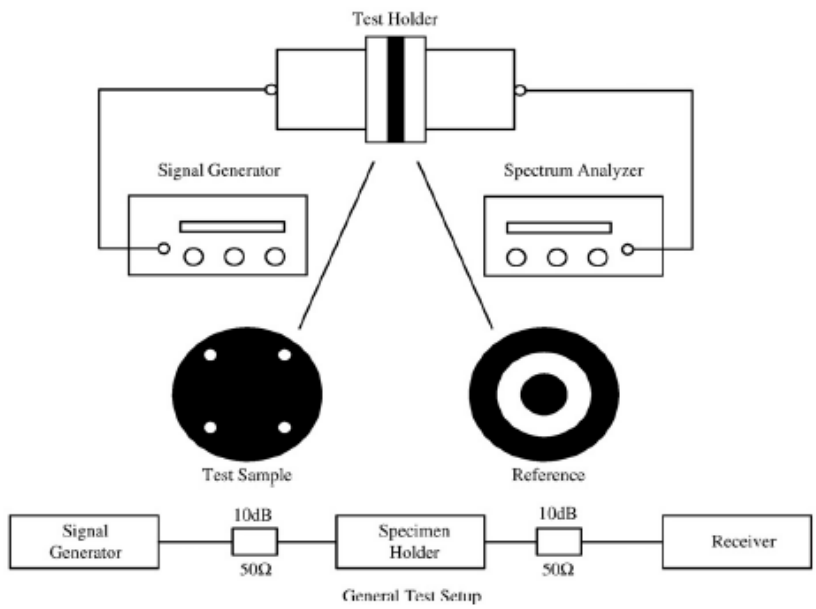

Figure 1.8. Set-up for electromagnetic shielding efficiency measurement [31].

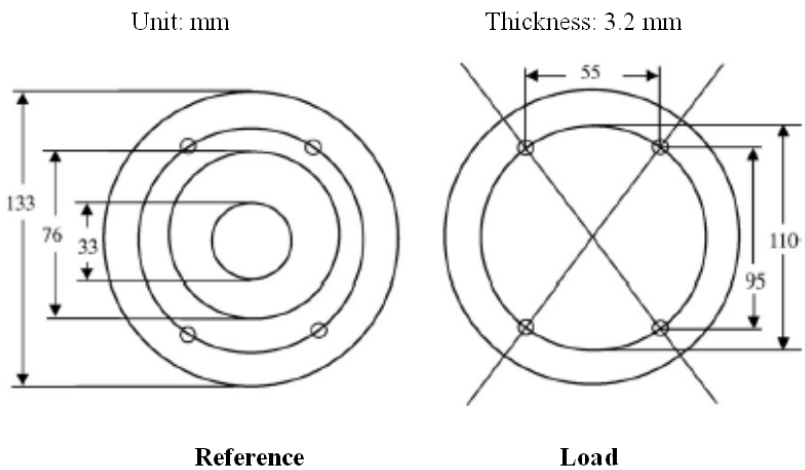

Figure 1.9. Specimen for electromagnetic shielding efficiency measurement.

1.4 Research objectives

Recently, IT devices such as e-books, cellular phones, flat-screen TVs, and digital cameras have become thinner and integrated, and automobiles have been equipped with various electronic devices. These trends have led to issues such as electromagnetic interference and exposure of human beings to electromagnetic waves. Metallic materials have superior electrical conductivity and electromagnetic interference (EMI) shielding effectiveness. However, they have some disadvantages too, such as their high weight and limited design options due to high material processing costs and a difficulty for complicated molding. While polymers have some advantages such as lightness and ease of processing, there are usually no electrical properties. Therefore it is very important to impart electrical conductivity and EMI shielding property to polymer/filler composites for dramatically widening the range of polymer applications.

The objectives of this research are to understand the mechanism of electrical properties of electrically conductive polymer composites and propose new approach to enhance the efficiency of conductive fillers for more effective polymer composites for human beings. This study consist of three parts. One is polymer/carbon fiber system, investigating the influence of fiber length and fiber orientation structure within polymer/carbon fiber composites on their EMI shielding efficiency to help better understand the behavior of EMI SE of these composites fabricated by commercial processes. Next, polymer/carbon fiber/ carbon nanotube system is selected, to understand the mechanism of the synergistic effect produced by a mixture of carbon fiber and carbon nanotube. Lastly, I propose new composite system, polymer/low-melting-point metal alloy (LMA)/light metal fiber composite system.

Bibliography

[1] Matthews F. L., Rawling R. D.: Composite materials: Engineering and science. Chapman & Hall, London (1994).

[2] Shaffer, G. D.: An Archaeomagnetic Study of a Wattle and Daub Building Collapse. Journal of Field Archaeology, 20, 59-75 (1993).

[3] Schwartz M. M.: Composite Materials. Prentice-Hall, New Jersey (1997).

[4] Donnet J. B., Bansal R. C., Wang M. J.: Carbon black: Science and technology. 2nd ed., Marcel Dekker, New York (1993).

[5] Pierson H. O.: Handbook of carbon, graphite, diamond and fullerens. Noyes Publications, New Jersey (1993).

[6] Sengupta R., Bhattacharya M., Bandyopadhyay S., Bhowmick A. K.: A review on the mechanical and electrical properties of graphite and modified graphite reinforced polymer composites. Progress in Polymer Science, 36, 638-670 (2011).

[7] Hammel E., Tang X., Schmitt T., Mauthner K., Eder A., Potschke P.: Carbon nanofibers for composite applications. Carbon, 42, 1153-1158 (2004).

[8] Bigg D. M.: Mechanical, thermal, and electrical properties of metal fiber-filled polymer composites. Polymer Engineering & Science, 19, 1188-1192 (1979).

[9] Li Y. J., Xu M., Feng J. Q., Dang Z. M.: Dielectric behavior of a metal-polymer composite with low percolation threshold. Applied Physics Letters, 89, 072902 (2006).

[10] Bloor D., Donnelly K., Hands P. J., Laughlin P., Lussey D.: A metal–polymer composite with unusual properties. Journal of physics D: Applied Physics, 38, 2851-2860 (2005).

[11] Kumar A. M., Kwon S. H., Jung H. C., Shin K. S.: Corrosion protection performance of single and dual Plasma Electrolytic Oxidation (PEO) coating for aerospace applications. Materials Chemistry and Physics, 149-150, 480-486 (2015).

[12] Song J. H., Nam K. S., Moon J. I., Choi Y. J., Lim D. Y.: Influence of the duty cycle on structural and mechanical properties of oxide layers on Al-1050 by a plasma electrolytic oxidation process. Metals and Materials International, 20, 451-458 (2014).

[13] Pike G. E., Seager C. H.: Percolation and conductivity: A computer study. I. Physical Review B, 10, 1421-1434 (1974).

[14] Broadbent S. R., Hammersley J. M.: Percolation processes I. crystals and mazes. Mathematical Proceedings of the Cambridge Philosophical Society, 53, 629-641 (1957)

[15] Stauffer D., Aharony A.: Introduction to percolation theory. 2nd Ed., Taylor and Francis, London (1994).

[16] Kirkpatrick S.: Percolation and conduction. Reviews of Modern Physics, 45, 574-588 (1973).

[17] Nielsen L. E.: The thermal and electrical conductivity of two-phase systems. Industrial & Engineering Chemistry Fundamentals, 13, 17-20 (1974).

[18] McCullough R. L.: Generalized combining rules for predicting transport properties of composite materials. Composites Science and Technology, 22, 3-21 (1985).

[19] Sherman R. D., Middleman L. M., Jacobs S. M.: Electron transport processes in conductor-filled polymers. Polymer Engineering & Science, 23, 36-46 (1983).

[20] Taya M., Ueda N.: Prediction of the in-plane electrical conductivity of a misoriented short fiber composite: fiber percolation model versus effective medium theory. Journal of Engineering Materials and Technology, 109, 252-256 (1987).

[21] Weber M., Kamal m. R.: Estimation of the volume resistivity of electrically conductive composites. Polymer Composites, 18, 711-725 (1997).

[22] Batchelor G. K., O'Brien R. W.: Thermal or electrical conduction through a

granular material. Proceeding of the Royal Society of London A, 355, 313-333 (1977).

[23] Taipalus R., Harmia T., Zhang M. Q., Friedrich K.: The electrical conductivity of carbon-fibre-reinforced polypropylene/polyaniline complex-blends: experimental characterization and modeling. Composites Science and Technology, 61, 801-814 (2001).

[24] Inskip P.D., Hoover R. N., Devesa S. S.: Brain cancer incidence trends in relation to cellular telephone use in the United States. Neuro Oncology, 12, 1147-1151 (2010).

[25] Shrestha M., Raitanen J., Salminen T., Lahkola A., Auvinen A.: Pituitary tumor risk in relation to mobile phone use: A case-control study. Acta Oncology, 54, 1159-1165 (2015).

[26] Kim H. S., Kim Y. J., Lee Y. H., Lee Y., Choi H. D., Pack J., Kim N., Ahn T. H.: Effect of whole-body exposure to the 848.5 MHz code division multiple access (CDMA) electromagnetic field on adult neurogenesis in the young, healthy rat brain. International Journal of Radiation Biology, 91, 354-359 (2015).

[27] Moliton A.: Basic electromagnetism and materials. Springer, New York (2007).

[28] Geetha S., Kumar S. K. K., Rao C. R. K., Vijayan M., Trivedi D. C.: EMI Shielding: Methods and Materials—A Review. Journal of Applied Polymer Science, 112, 2073-2086 (2009).

[29] Al-Saleh M. H., Sundararj U.: Electromagnetic interference shielding mechanisms of CNT/polymer composites. Carbon, 47, 1738-1746 (2009).

[30] ASTM D4935-10: Standard Test Method for Measuring the Electromagnetic Shielding Effectiveness of Planar Materials, USA (2010).

[31] Chen C. S., Chen W. R., Chen S. C., Chien R. D.: Optimum injection molding processing condition on EMI shielding effectiveness of stainless steel

fiber filled polycarbonate composite. International Communication in Heat and Mass Transfer, 35, 744-749 (2008).

Chapter 2. Polymer/carbon fiber system

2.1 Introduction

In current years composites based on carbon fibers (CFs) are becoming one of the greater priority due to their low density with much higher strength [1-3]. It is reported that carbon fiber has much lower density than steel and thus provides lightweight structural materials with advanced properties. Accordingly, they are considered as the most interesting fillers for advanced applications of composites. Lightweight automobile components made up of carbon fiber reinforced composites results in weight savings and therefore major savings in the energy. Other applications include electrical conductive fillers, rechargeable batteries, fuel cell electrodes, lightweight panelling, lightweight concrete, and asphalt.

In this section, I investigated the influence of fiber length and fiber orientation structure within polymer/CF composites on their electromagnetic interference shielding efficiency (EMI SE) to help better understand the behavior of EMI SE of these composites fabricated by commercial processes. I used a crystalline polymer (polyamide 6,6) and an amorphous polymer (polycarbonate) which are used commonly in industrial fields. Polymer/CF composites were fabricated using commercial processes (extrusion and injection) in industrial fields. EMI SE, electrical conductivity, magnetic permeability of polymer/CF composites were measured. In addition, Fiber length and fiber orientation structure in the specimen of polymer/CF composite were observed. Consequently the effects of fiber length and fiber orientation structure of polymer/CF composites on the EMI SE were investigated in this study.

2.2 Experimental

2.2.1 Materials

CF was used as conductive filler. CF used was PX35CA0250-65 with a diameter of 7 μm and a cutting length of 6 mm; it was sized with polyurethane provided by Zoltek (Canada). As matrix material, polyamide 66 (PA) and polycarbonate (PC) were used. PA used was Leona-1200 provided by Asahi Kasei Co. Ltd. (Japan) and had the following properties: melting temperature 260°C; glass transition temperature 65°C; melt flow index 125 g/10 min (270°C, 2.16 kg); and density 1.14 g/cm^3. PC used was SC-1190 provided by Samsung SDI Co., Ltd. and had the following properties: glass transition temperature 130°C; melt flow index 19 g/10 min (300°C, 1.2 kg); and density 1.20 g/cm^3.

2.2.2 Preparation of composite samples

Conductive composite pellets were fabricated using a twin extruder (JSW, Japan) with an L/D ratio of 44 and a diameter of 45 mm. For this, matrix material polymers and carbon fiber were compounded at 290°C with a feeding rate of 60 kg/h and a screw velocity of 200 rpm. The content of CF was varied among 5, 15, 25, 35, 45 wt% to produce PA/CF and PC/CF composites. These prepared pellets were dried at 120℃ for 2 h in a dehumidifying dryer. Further, using an injection machine with a diameter of 40 mm and a loading capacity of 150 ton (Woojin Selex, Korea), 152.4 × 152.4 × 3.2 mm plates were produced at the barrel temperature of 300°C and the mold temperature of 80°C. The specimens were fabricated as shown Figure 2.1.

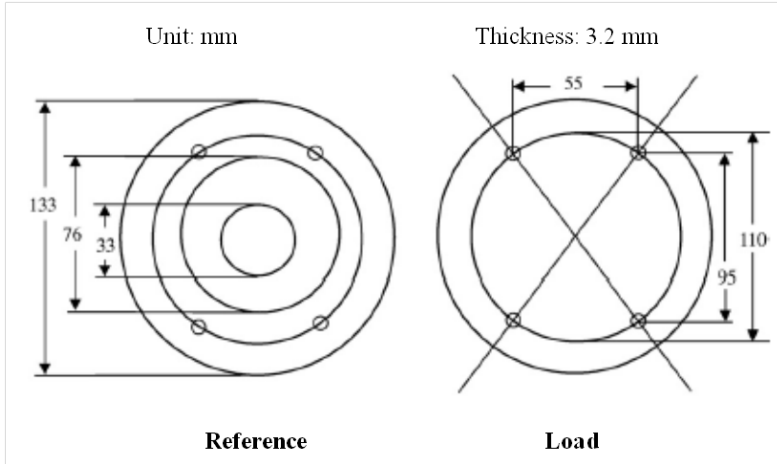

(a)

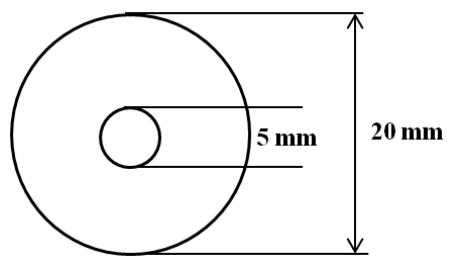

(b)

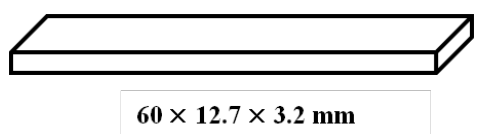

(c)

Figure 2.1. Specimens for properties evaluation (a) EMI SE (b) magnetic permeability (c) electrical conductivity

2.2.3 Measurements

The morphology of CFs in the polymer matrix was observed by field-emission scanning electron microscopy (FE-SEM; SU-70, Hitachi, Japan). Steady shear viscosity was measured using capillary rheometer (Rheograph 120, Goettfert, Germany) with diameter 1 mm and length 30 mm die at 300 ℃. For samples with an electrical conductivity higher than 10^{-7} S/cm, the electrical conductivity was measured by a four-point probe method at room temperature. The dimensions of the sample for electrical conductivity measurements were 60 mm×12.7 mm×3.2 mm. A constant current was applied using a source meter (2400, Keithley, USA) to the outer probes of the four contacts, and the corresponding voltage was measured between inner probes using a nanovolt meter (2182, Keithley, USA). For samples with an electrical conductivity lower than 10^{-7} S/cm, the measurements were performed by a two-point probe method using only a source meter. EMI SE at room temperature was measured using E8362B (Agilent, USA) according to the method described in ASTM D4935. For measuring the average length of CFs remaining in PA/CF specimens, 1 g specimen was collected and dissolved in trifluoroacetic acid (TFA) for over 24 h at room temperature, and the solvent was then removed through filtering. From the remaining CFs, 500 were randomly selected for length measurement to obtain the average length using optical microscopy (OM; VHX-600E, Keyence, Japan). For PC/CF specimens, chloroform was selected as the solvent and other processes were conducted identically as in the case of PA/CF specimens. A Micro-CT system (Skyscan, 1172, Bruker, USA) was used to explore the micro structure of composites. A source voltage was 43 kV, which was powerful enough to obtain 3D images. The data from Micro-CT were analyzed quantitatively by using a image analysis tool (Dataviewer, Bruker, USA). For better visual analysis, the images obtained from the Micro-CT were reconstructed into 3D microstructures by using a image tool (CT Vox, Bruker, USA). For determining the CF orientation within a specimen, its cross-sectional image from the top and in a direction perpendicular to the polymer flow direction was obtained using OM. 200 CFs were sampled and their orientation relative to the

flow direction was measured. Equation (1) was then used to obtain the orientation function (OF) [4]:

$$OF = 2 < \cos^2\theta > -1 \quad (1)$$

where θ is the angle between the flow direction and CF and $< \cos^2\theta >$ is the number-average value. An orientation function value of 1 represents a parallel orientation to the flow direction; 0 represents a random orientation, and -1 represents a perpendicular orientation to flow direction.

2.3 Results and discussion

2.3.1 Electrical properties of the polymer/CF composites

As can be seen in Figure 2.2, PA/CF and PC/CF presented different behaviors of EMI SE according to increasing CF content. For PA/CF, as the CF content increased, EMI SE continuously increased; however, for PC/CF, EMI SE increased until a CF content of 25 wt%, beyond which EMI SE became saturated. The trend of EMI SE of PA/CF is similar to the Keith et al.'s results [5]. The trend of EMI SE of PC/CF is similar to the trend of EMI SE of PC/ABS (9/1) with CF in the report of Huang et al [6]. The cause of the EMI SE saturation was not discussed because the main aim in Huang et al.'s study was the effect of nickel coated CF. To investigate this in more detail, we explored the factors that contribute to EMI SE. EMI SE can be divided into three contributions, as given by Equations (2-5) [7]:

$$\text{EMI SE} = \text{SE}_\text{R} + \text{SE}_\text{A} + \text{SE}_\text{MR} \tag{2}$$

$$\text{SE}_\text{R} = 20\log\left|\frac{\eta_0}{4\eta_\text{s}}\right| \tag{3}$$

$$\text{SE}_\text{A} = 20\log\left|e^{d/\delta}\right| \tag{4}$$

$$\text{SE}_\text{MR} = 20\log\left|1 - e^{-2d/\delta}\right| \tag{5}$$

where SE_R represents SE due to reflection, SE_A represents SE due to absorption, and SE_MR represents SE due to multi-reflection. η_0 is impedance in free space and η_s is impedance of the shielding material. d is the width of the medium and δ is skin depth and is shown in Equation (6):

$$\delta = \frac{1}{\sqrt{\pi f \mu \sigma}} \tag{6}$$

where f is the EM wave frequency, μ is the magnetic permeability of the medium, and σ is the electrical conductivity of the medium. Impedance can be considered to be given by Equation (7):

$$\eta = \frac{|\text{E}|}{|\text{B}|} = \sqrt{\frac{j\omega\mu}{\sigma + j\omega\epsilon}} \tag{7}$$

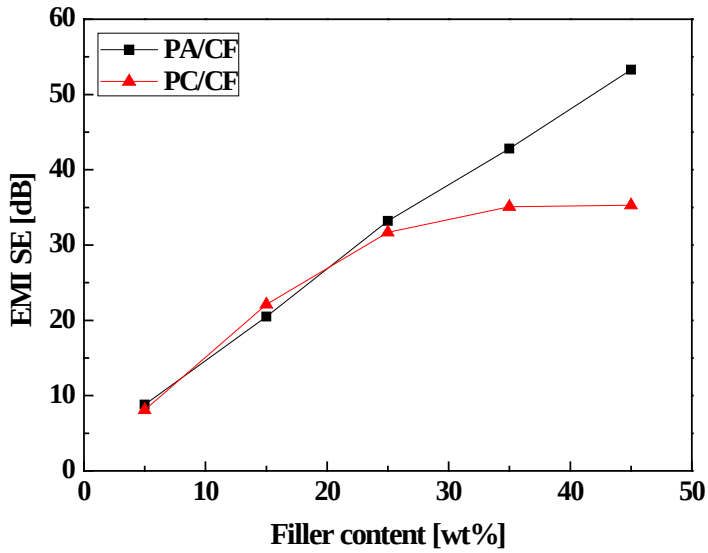

Figure 2.2. EMI SE at 1 GHz of PA/CF and PC/CF composites

where |E| is the electric field amplitude and |B| is the magnetic field amplitude. ω is the angular frequency of EM wave and ϵ is the permittivity of the medium. σ is 0 on EM wave in free space; therefore, η_0 is given by Equation (8):

$$\eta_0 = \sqrt{\frac{\mu_0}{\epsilon_0}} = 337\ \Omega \tag{8}$$

where μ_0 is the magnetic permeability in free space (1.26×10^{-6} H/m) and ϵ_o is the permittivity in free space (8.85×10^{-12} F/m). For an electrically conductive material, $\sigma >> \omega\epsilon$; this relation results in Equation (9) given below:

$$\eta_s = \sqrt{\frac{j\omega\mu}{\sigma}} \tag{9}$$

If the width of the shielding material is amply greater than the skin depth, the contribution due to multi-reflection can be ignored. Then, substituting Equations (6), (8), and (9) into Equations (3-4), contributions such as those given by Equations (10-11) contribute to EMI SE.

$$\mathrm{SE_R} = 39.5 + 10\log\left|\frac{\sigma}{2\pi f j\mu}\right| \tag{10}$$

$$\mathrm{SE_A} = 8.7d\left|\sqrt{\pi f\mu\sigma}\right| \tag{11}$$

As you can be seen from Equations (10-11), both Electrical conductivity and magnetic permeability effect on EMI SE. When electrical conductivity increases, both SE_R and SE_A increase, however, when magnetic permeability increase, SE_R decreases and SE_A increases.

The electrical conductivity and complex magnetic permeability at 1 GHz of PA/CF and PC/CF were measured, and the results are shown in Figures 2.3 and 2.4. For magnetic permeability, both PA/CF and PC/CF presented the decrease of the real part and the increase of the imaginary part at CF content over 25 wt%, so the absolute values of magnetic permeability kept similar values at overall CF content. As CF content increased, the electrical conductivity of PA/CF increased consistently, but the increase in the electrical conductivity of PC/CF slowed down at CF content over 25 wt%; moreover, it is considered that the EMI SE of PC/CF was saturated at CF content over 25 wt%. The values of EMI SE, SER, and SEA were calculated using Equations (10-11) on the basis of the measured electrical conductivity and magnetic permeability values for PA/CF and PA/CF in Figure 2.5.

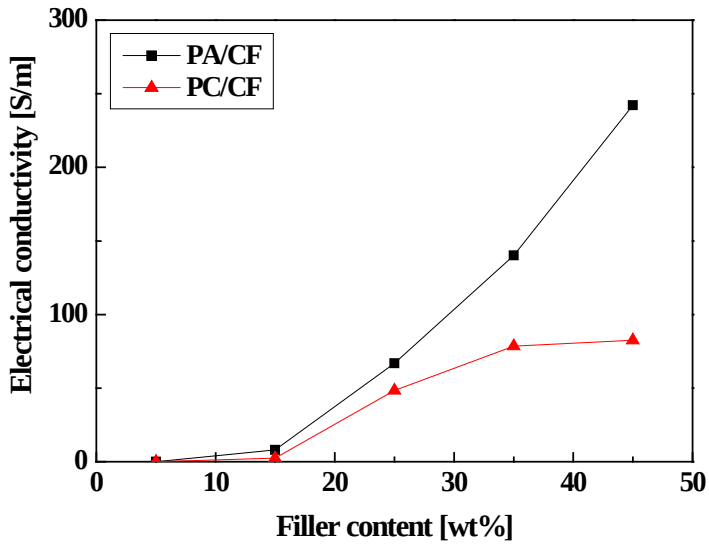

Figure 2.3. Electrical conductivity of PA/CF and PC/CF composites.

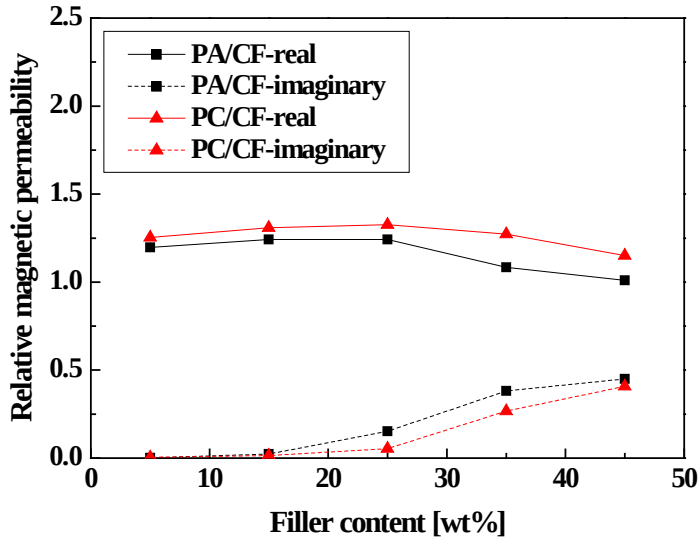

(a)

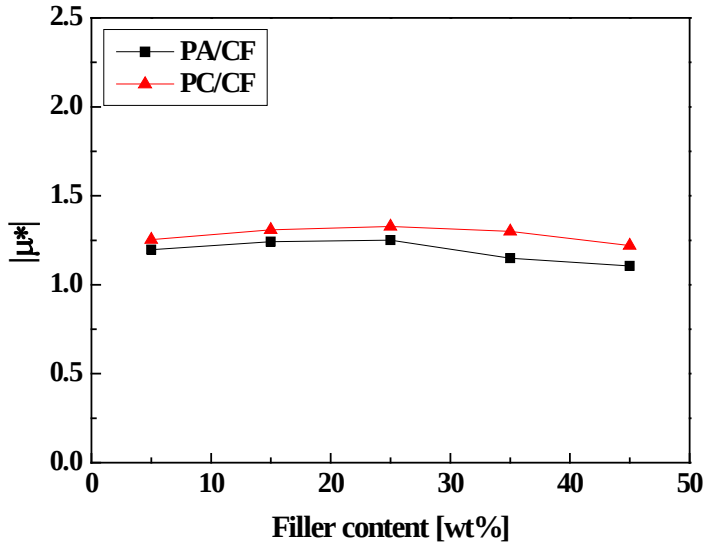

(b)

Figure 2.4. Relative complex magnetic permeability of PA/CF and PC/CF composites: (a) real part and imaginary part, (b) absolute value.

In the case of PA/CF, as the CF content increase, both absorption and reflection SE increases, the gradient of the increase in absorption SE being larger than that for reflection SE. However, for PC/CF, both reflection and absorption SE saturated. In particular, the absorption SE of PC/CF was smaller than that of PA/CF. Consequently the difference of the electrical conductivity of PA/CF and PC/CF composites is the main cause of the difference in EMI SE of them. As can be seen in Tables 2.1 and 2.2, the calculated values of EMI SE were similar to the experimentally measured values, and this observation backs up the abovementioned interpretation.

2.3.2 Fiber length and fiber orientation structure in the polymer/CF composites

Fiber length and fiber orientation structure within the composites was studied to determine the cause of differences in the electrical conductivity of PA/CF and PC/CF composites containing identical CF. First, as a factor that could influence electrical conductivity, the residual fiber length within the composites was measured and the results are shown in Figure 2.6. The average fiber length decreased with an increase in the CF content, and the average fiber length of PC/CF was shorter than that of PA/CF. The CFs were broken owing to shear, and as shown in Figure 2.7, with an increase in the CF content, viscosity increased, causing greater shear [8]. Moreover, because PC/CF had higher viscosity than PA/CF, it is considered that the residual fiber length in PC/CF was shorter than that in PA/CF owing to higher shear. However, in both polymers, the average CF length decreased with increasing CF content and showed a linear behavior. Therefore, it was concluded that the average CF length cannot fully explain the fact that there was a small increment in the electrical conductivity of PC/CF at CF content over 25 wt%.

To find other factor, the fiber orientation within the composites was also examined. For this, cross sections of the specimens were observed in the flow direction by using SEM.

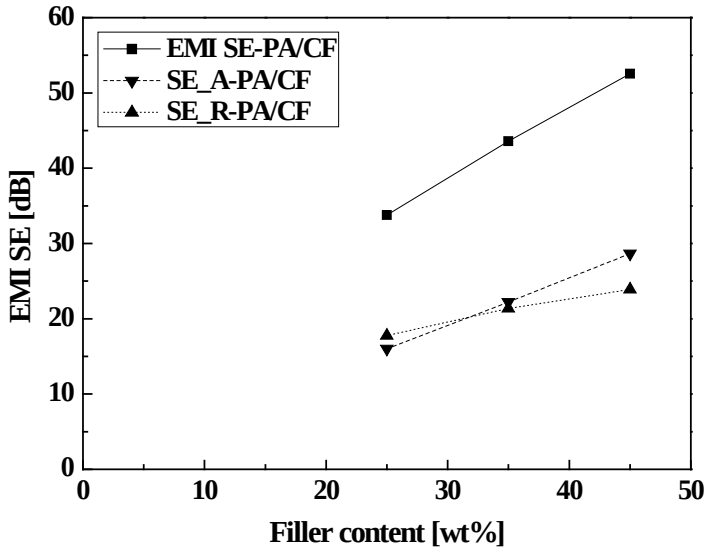

(a)

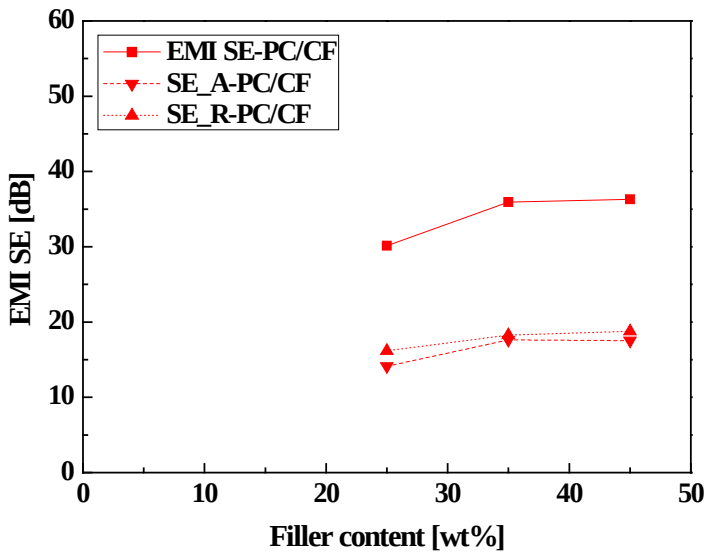

(b)

Figure 2.5. EMI SE (solid line) of composites to SE_A (dashed line) and SE_R (dotted line) at 1 GHz calculated by Equations (10-11): (a) PA/CF, (b) PC/CF.

Table 2.1. Electrical properties of PA/CF composites; cal. represents calculated data obtained using Equations (10-11)

CF content [wt%]	σ [S/m]	μ_r'	μ_r''	$\lvert\mu_r^*\rvert$	EMI SE [dB]	EMI SE -cal. [dB]	SE_A-cal. [dB]	SE_R-cal. [dB]
5	1.01×10^{-5}	1.20	0.001	1.20	8.8	-	-	-
15	7.92×10^{0}	1.24	0.023	1.24	20.5	-	-	-
25	6.68×10^{1}	1.24	0.153	1.25	33.2	33.8	16.0	17.8
35	1.40×10^{2}	1.08	0.382	1.15	42.8	43.6	22.2	21.4
45	2.42×10^{2}	1.01	0.450	1.11	53.3	52.6	28.7	23.9

Table 2.2. Electrical properties of PC/CF composites; cal. represents calculated data obtained using Equations (10-11)

CF content [wt%]	σ [S/m]	μ_r'	μ_r''	$\lvert\mu_r^*\rvert$	EMI SE [dB]	EMI SE -cal. [dB]	SE_A-cal. [dB]	SE_R-cal. [dB]
5	1.20×10^{-4}	1.25	0.004	1.25	8.1	-	-	-
15	2.50×10^{0}	1.31	0.014	1.31	20.1	-	-	-
25	4.83×10^{1}	1.33	0.054	1.33	31.7	30.1	14.1	16.1
35	7.80×10^{1}	1.27	0.267	1.30	35.1	35.9	17.6	18.3
45	8.20×10^{1}	1.15	0.407	1.22	35.3	36.3	17.5	18.7

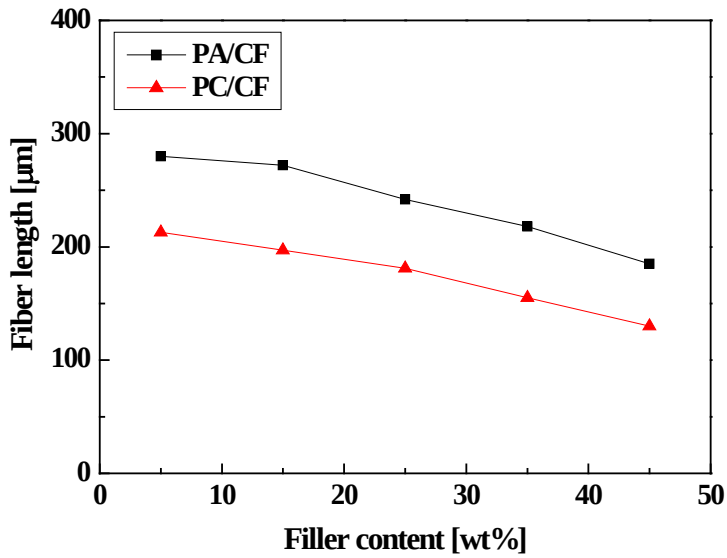

Figure 2.6. Average length of residual fibers in PA/CF and PC/CF composites

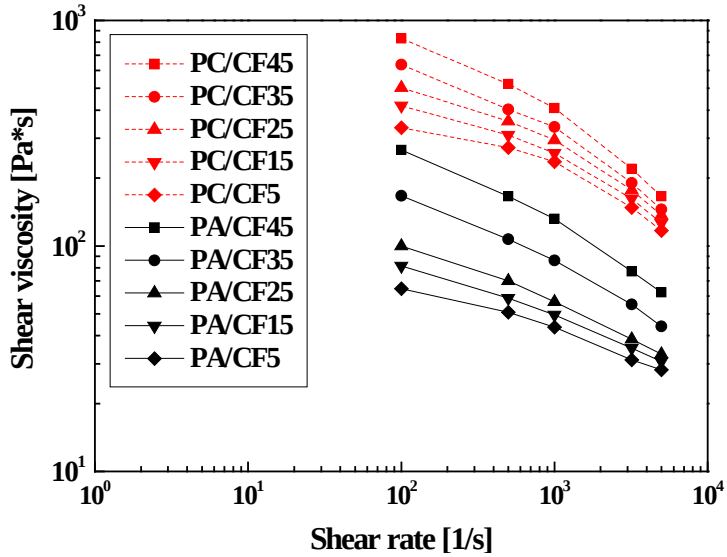

Figure 2.7. Steady shear viscosity of the PA/CF and PC/CF composites

As shown in Figure 2.8, the CFs in the skin area of specimen were oriented along the flow direction but the CFs in the center area of the specimen were oriented perpendicular to the flow direction. This shows that when the composite melt moves through the mold, shear was at its maximum at the wall surface or nearby and decreased with increasing distance from the wall surface [9]. It can be concluded that a selective orientation to the flow direction for CFs closer to the wall surface was attributed to shear distribution. For the center area of the specimen, the effect of shear disappeared and as solidification occurred in the wall surface area, the composite melt flowed inside and CFs were oriented perpendicular to the flow direction due to elongation flow [10]. In addition, as can be seen in Figure 2.8, the core area thickness of PC/CF was lower than that of PA/CF, which is because compared to PA/CF, the viscosity of PC/CF was higher and it had a larger area of shear influence. Moreover, solidification in PC/CF occurred more quickly owing to a higher glass transition temperature and this resulted in a thicker skin layer where fibers were oriented in the flow direction.

To observe the fiber orientation in more detail, the micro-CT test was conducted. Figure 2.9 shows that the CFs in the skin area of specimen were oriented along the flow direction but the CFs in the center area of the specimen were oriented perpendicular to the flow direction, which is consistent with the results of SEM in Figure 2.8. These results indicated that the fiber orientation changed according to the distance from the surface within the composite. Therefore, the fiber orientation was measured according to the distance from the surface using micro-CT as shown in Figure 2.10. Furthermore, the specimens were polished to remove surface thickness by 0.1 mm and the fiber orientation was measured using OM as shown in Figures 2.11 and 2.12. From these results, the CFs were oriented in the flow direction near the top surface, and as the distance from the surface increased, they became disordered. However, at the center, they were oriented perpendicular to the flow direction, but as the distance increased further, they became disordered again. Near the bottom surface, they again became oriented along the flow direction. These observations are quantified via an orientation function (OF) versus normalized thickness for PA/CF and PC/CF, as shown in Figure 2.13.

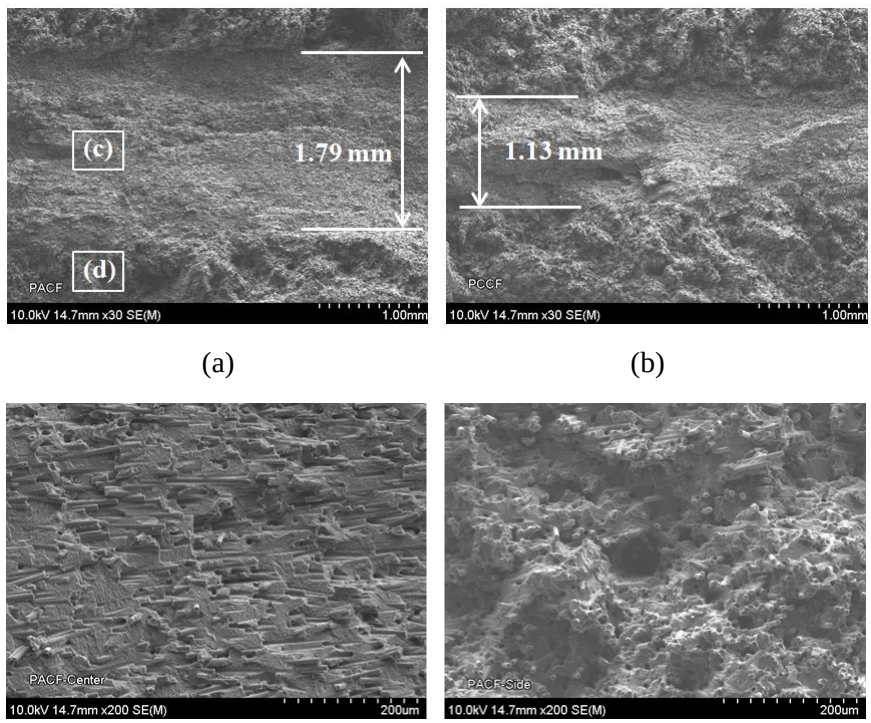

(a) (b)

(c) (d)

Figure 2.8. Cross-sectional SEM images along flow direction: (a) overall view of PA/CF with 35 wt% CF, (b) overall view of PC/CF with 35 wt% CF, (c) core area of PA/CF with 35 wt% CF, (d) skin area of PA/CF with 35 wt% CF

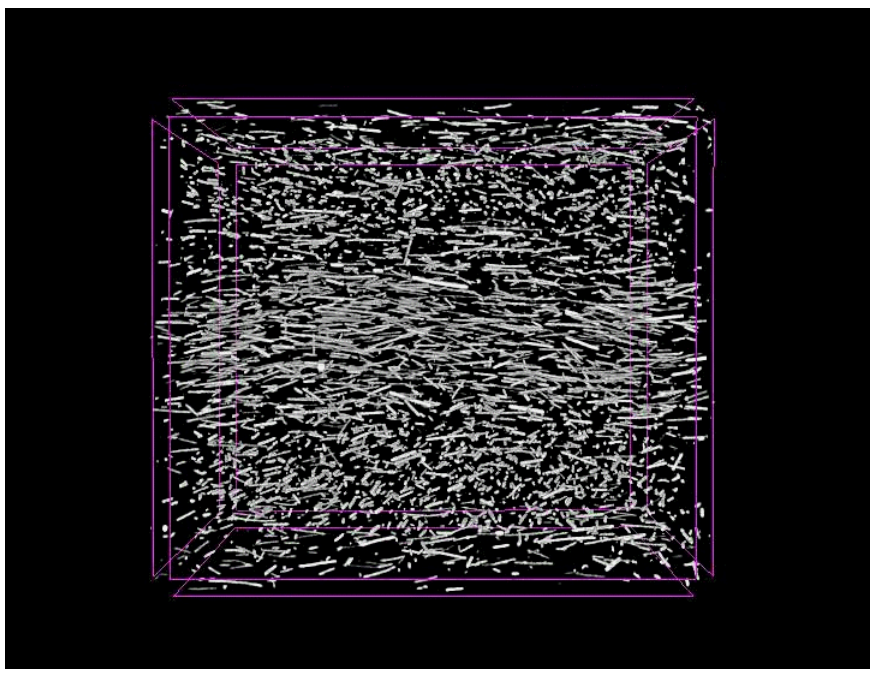

Figure 2.9. Cross-sectional micro-CT image along flow direction

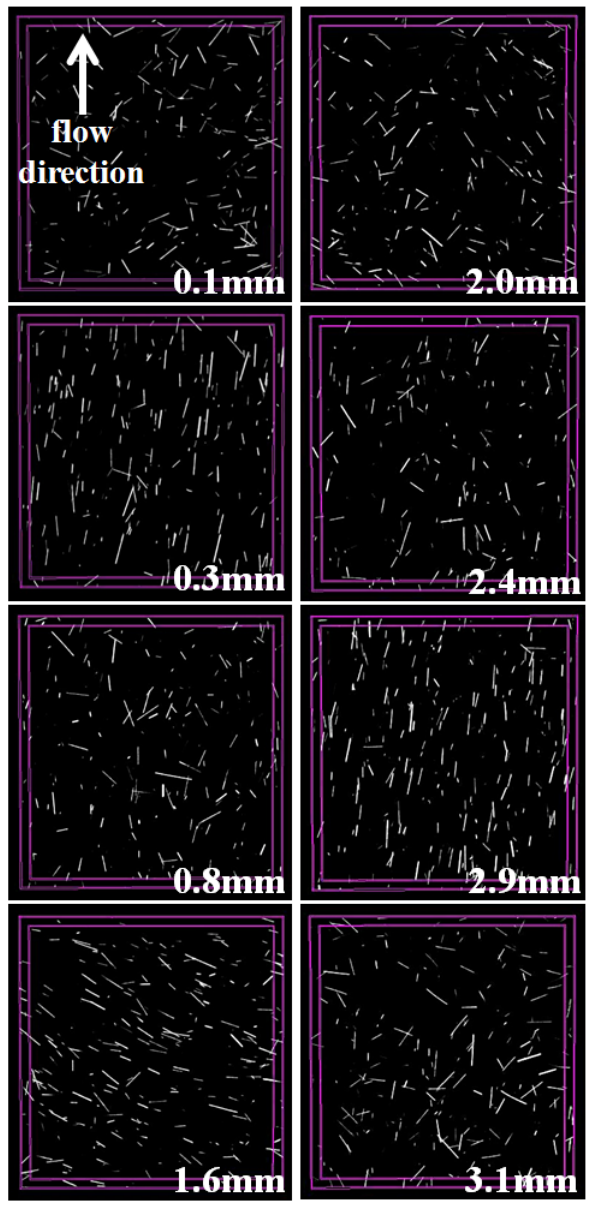

Figure 2.10. Micro-CT images according to the distance from the surface of PA/CF 35 wt%

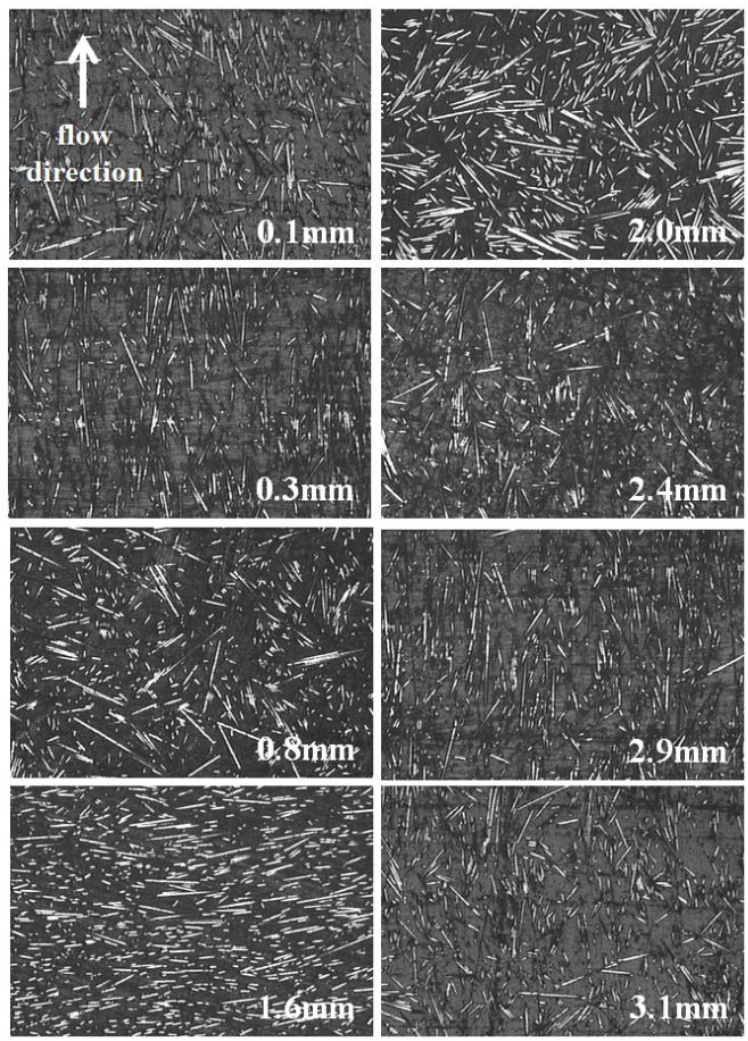

Figure 2.11. OM images of the polished surface according to the distance from the surface of PA/CF 35 wt%.

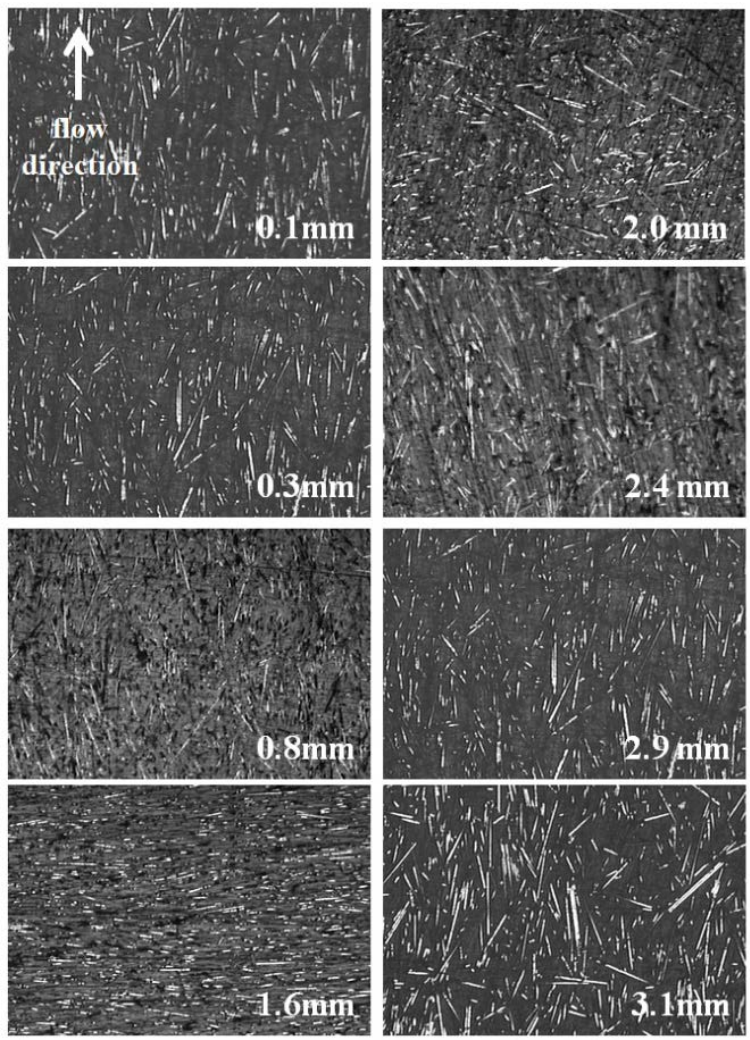

Figure 2.12. OM images of the polished surface according to the distance from the surface of PC/CF 35 wt%.

At the surface (normalized thickness = 0 or 1), the orientation function value was positive and CFs were oriented along the flow direction; however, in the center area (normalized thickness = 0.5), the value of OF was negative and CFs were oriented perpendicular to the flow direction. These results are identical to those discussed previously for the skin and center areas; this also shows that the orientation of CFs continuously changed from the surface to the center area. For the CF content range of 5–15 wt%, the orientation of CFs at the surface was weaker than that for CF content over 25 wt%, and the differentiation between skin and core areas was not clear. Relatively, at 15 wt% CF, PC/CF had stronger orientation at the surface than PA/CF. This was attributed to the higher viscosity of PC/CF than that of PA/CF; this resulted in higher shear as well as larger shear getting transferred to CFs, resulting in stronger orientation. At CF content over 25 wt%, the differentiation between skin and center areas became clear and it was confirmed that as the CF content increased, the orientation at the surface (along the flow direction) and that at the center (perpendicular to the flow direction) became clearer and more prominent. If the thickness of the center area is considered as the domain that was not influenced by shear (OF is under 0), the core thickness of PA/CF is thicker than that of PC/CF. This result is identical to that obtained through SEM analysis as shown in Figure 2.8. Further, the fiber orientation in the skin and core areas of PA/CF was weaker than the corresponding orientations in PC/CF. This observation can be attributed to lesser shear transferred to the surface lesser area under shear influence in PA/CF; this resulted in a thicker core layer that caused a decreased effect on the orientation by the elongation flow. The domains of PA/CF and PC/CF in which the orientation was disordered were identified. In Figure 2.14, the thickness at which the absolute value of OF is under 0.5 is shown. At the CF content under 25 wt%, the thickness (given by OF; -0.5–0.5) of PA/CF was smaller than the corresponding thickness of PC/CF. However, at the CF content over 25 wt%, this trend was reversed, i.e., the thickness of PA/CF was greater than that of PC/CF. As the fiber orientation became disordered, the probability of contact between CFs increased, and this could in turn increase the electrical conductivity of the composites [11].

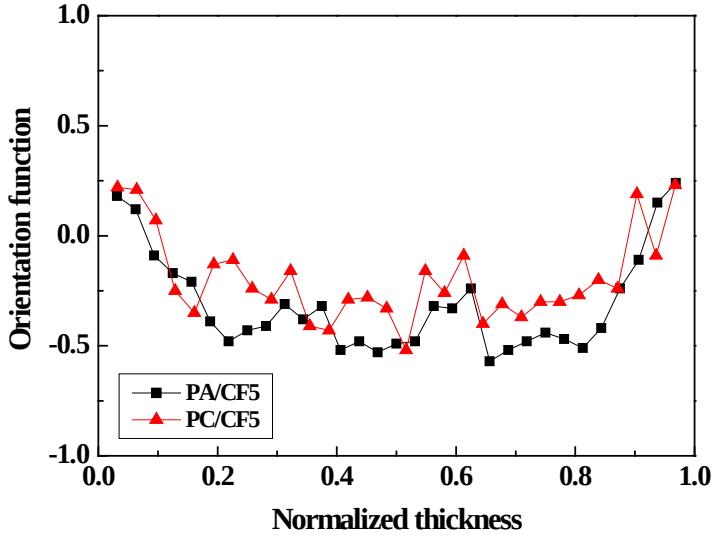

(a)

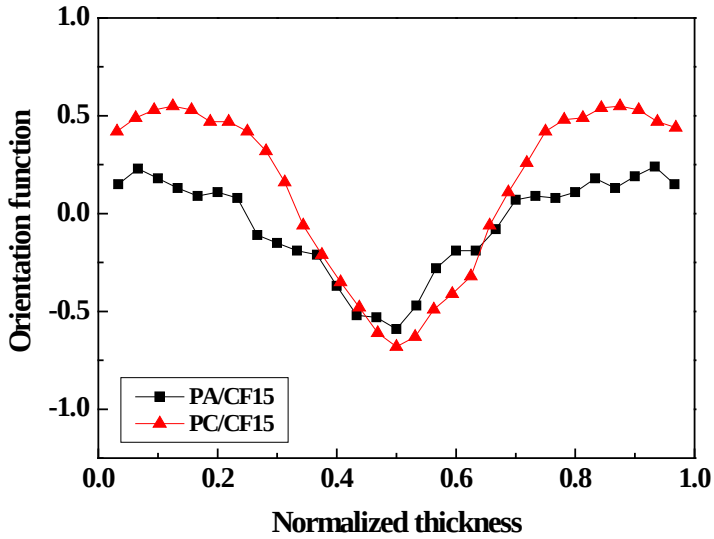

(b)

Figure 2.13. Orientation function for fibers in PA/CF and PC/CF composites as a function of normalized thickness: (a) 5 wt% CF, (b) 15 wt% CF, (c) 25 wt% CF, (d) 35 wt% CF, (e) 45 wt% CF.

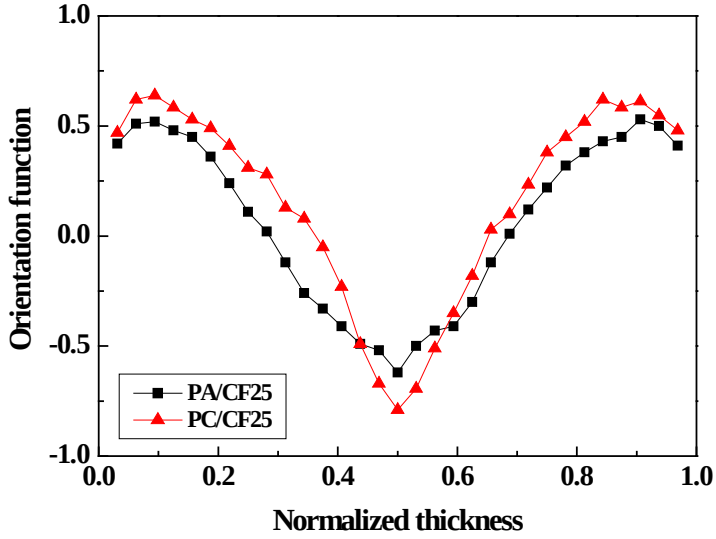

(c)

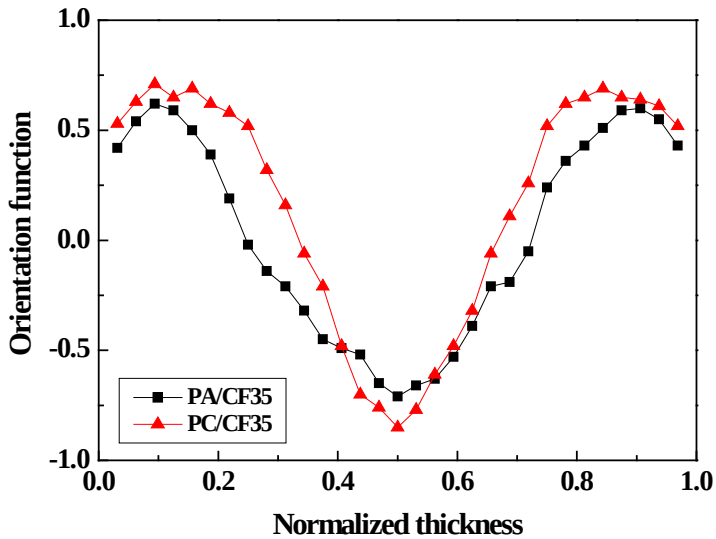

(d)

Figure 2.13. Orientation function for fibers in PA/CF and PC/CF composites as a function of normalized thickness: (a) 5 wt% CF, (b) 15 wt% CF, (c) 25 wt% CF, (d) 35 wt% CF, (e) 45 wt% CF. (continued)

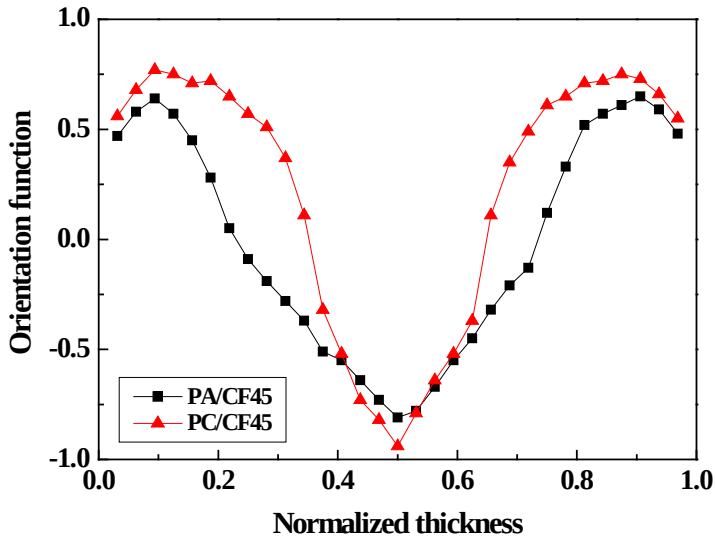

(e)

Figure 2.13. Orientation function for fibers in PA/CF and PC/CF composites as a function of normalized thickness: (a) 5 wt% CF, (b) 15 wt% CF, (c) 25 wt% CF, (d) 35 wt% CF, (e) 45 wt% CF. (continued)

Moreover, the longer residual fiber length in PA/CF than PC/CF could also increase the electrical conductivity of the composites [12]. Therefore, it is considered that the electrical conductivity of PA/CF with CF content over 25 wt% was greater than that of PC/CF.

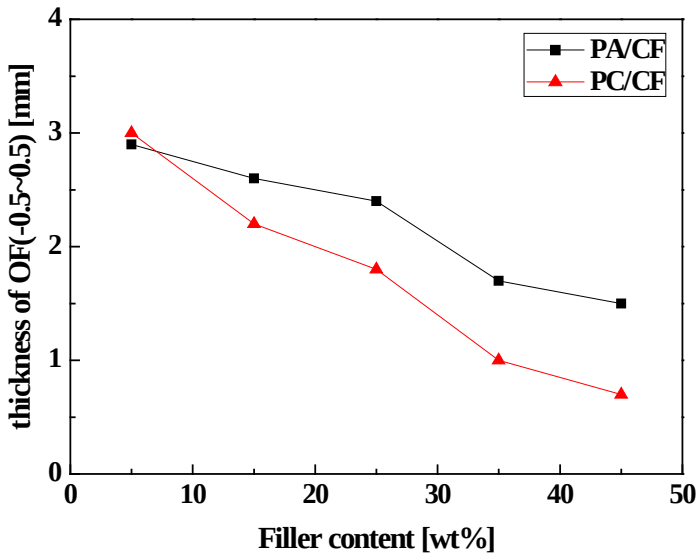

Figure 2.14. Thickness corresponding to orientation function values between -0.5 and 0.5 for residual fibers in PA/CF and PC/CF composites

2.4 Conclusions

In this section, the cause of differences in EMI SE of PA/CF and PC/CF composites according to their CF content was explored. As the CF content increased, EMI SE of PA/CF continuously increased but the increase in EMI SE of PC/CF slowed down from a CF content of 25 wt%. Theoretically electrical conductivity and magnetic permeability effect on EMI SE, the magnetic permeability of PA/CF is similar to that of PC/CF, however, the electrical conductivity of PA/CF is higher than that of PC/CF at CF content over 25wt%. The fiber length and fiber orientation structure within the composites were observed to identify the differences in the electrical conductivity increase in PA/CF and PC/CF. It was found that compared to PA/CF, PC/CF showed a shorter fiber length and fewer domains in which the fiber orientation was random, and this resulted in less electrical conductivity increase in PC/CF. The obtained theoretical and experimental results on fiber content, length, and orientation were compared with the corresponding values obtained using previous electrical conductivity models [11-14], and it was found that no models provided similar results. To interpret the results of this study in more detail, a new model is required that would take into consideration fiber content, length, and orientation structure.

Bibliography

[1] Chung D. D. L.: Comparison of submicron-diameter carbon filaments and conventional carbon fibers as fillers in composite materials. Carbon, 39, 1119-1125 (2001).

[2] Dani A., Ogale A. A.: Electrical percolation behavior of short-fiber composites: Experimental characterization and modeling. Composites Science and Technology, 56, 911-920 (1996).

[3] Deng S. H., Zhao J. J., Lin Q. F., Fan C. J., Zhou X. D.: Formation of interfacial network structure via photo-crosslinking in carbon fiber/epoxy composites. Express Polymer Letters, 8, 505-516 (2014).

[4] Taipalus R., Jarmia T., Zhang M. Q., Friedrich K.: The electrical conductivity of carbon-fibre-reinforced polypropylene/polyaniline complex-blends: experimental characterisation and modeling. Composites Science and Technology, 61, 801-814 (2001).

[5] Keith J. M., Janda N. B., King J. A., Perger W. F., Oxby T. J.: Shielding Effectiveness Density Theory for Carbon Fiber/Nylon 6,6 Composites. Polymer Composites, 26, 671-678 (2005).

[6] Huang C. Y., Wu C. C.: The EMI shielding effectiveness of PC/ABS/nickel-coated-carbon-fibre composites. European Polymer Journal, 36, 2729-2737 (2000).

[7] Al-Saleh M. H., Sundararj U.: Electromagnetic interference shielding mechanisms of CNT/polymer composites. Carbon, 47, 1738-1746 (2009).

[8] Kitano T., Kataoka T., Shirota T.: An empirical equation of the relative viscosity of polymer melts filled with various inorganic fillers. Rheologica Acta, 20, 207-209 (1981).

[9] Alsten J. A., Granick S.: Shear rheology in a confined geometry: polysiloxane melts, Macromolecules, 23, 4856-4862 (1990).

[10] Pathanasiou T. D., Guell D. C.: Flow-induced alignment in composite

materials. Woodhead Publishing Ltd, Cambridge (1997).

[11] Weber M., Kamal M. R.: Estimation of the volume resistivity of electrically conductive composites. Polymer Composites, 18, 711-725 (1997).

[12] Nielsen L.E.: The thermal and electrical conductivity of two-phase systems. Industrial & Engineering Chemistry Fundamentals, 13, 17-20 (1974).

[13] McCullough R. L.: Generalized combining rules for predicting transport properties of composite materials. Composites Science and Technology, 22, 3-21 (1985).

[14] Xue Q.: The influence of particle shape and size on electric conductivity of metal–polymer composites. European Polymer Journal, 40, 323-327 (2004).

Chapter 3. Polymer/carbon nanotube/carbon fiber system

3.1 Introduction

In previous section, polymer/carbon fiber system was investigated, indicating that the length and orientation structure of carbon fiber within polymer significantly effect on the electrical properties of the composites. It is supposed that controlling these factors can enhance the efficiency of conductive fillers. Furthermore, another method to enhance the efficiency of conductive fillers is to combine two kinds of fillers for producing a synergistic effect.

The most commonly used industrial method is to add carbon fillers such as graphite, carbon black, and carbon fiber (CF), to insulating polymers. Graphite and carbon black have the advantages of low cost, and high electrical conductivity [1-3]; however, they requires high contents to produce conductivity, causing increase in viscosity, poor degassing behavior, and degradation of processability of the composites. CF has the advantages of high electrical conductivity, high rigidity, and high reinforcing effectiveness in fibrous shape [4-5]. Similar to graphite and carbon black, they have the disadvantage that a high content of CF increases the viscosity of the composite. This lowers processability and degrades the exterior quality of the product because of CF protruding from the product surface. Carbon nano-fillers such as carbon nanotube (CNT), carbon nanofiber, graphite nanoplatelet, and graphene, are promising alternatives, which can have large effects even when present in small amounts as they has nano-scale dimensions and large specific surface areas [6-8]. However, they have some limitations such as high cost, poor dispersibility in a polymer matrix due to van der Waals and Coulomb attractions, and limited adding amount due to high specific surface area.

Consequently, carbon nano-fillers are significantly effective to reduce the percolation thresholds of the polymer nanocomposites, however, the conductivity values are typically less than 1 S/cm [9-11].

One of methods to solve these problems is to combine two different kinds of carbon fillers such as CNT/carbon black, CNT/graphite nanoplatelet, graphite/CF, carbon black/CF, and CNT/CF. These approaches can increase the efficiency of fillers by producing a synergistic effect. When mixed, two or more kinds of fillers cooperate in creating a co-supporting conductive network that lowers the percolation threshold and improves electrical properties. For polymer/CNT/carbon black composites, when carbon black particles were added into nanocomposites containing CNTs, the gaps between the CNTs were effectively filled and the CNTs were linked together, resulting in the formation of conducting networks [12-13]. It can reduce percolation threshold of the composites. However, once the conducting networks were formed above the percolation threshold, the addition of hybrid fillers contributed little to enhancement of the conductivity. In the case of polymer/CNT/graphite nanoplatelet, by incorporating small amounts of CNTs, the electrical conductivity enhanced drastically by several orders of magnitudes and the percolation threshold was lowered due to the formation of a hybrid CNT/graphite nanoplatelet network with naturally enahnced properties [14]. Addition of CF into polymer/graphite or carbon black composites enhanced the electrical conductivity as multi-scale carbon fillers form the effective three-dimensional conductive pathway and electrons are transported over long distances by CFs with little loss of energy [15-17].

In this section, CF and CNT were selected as conductive fillers because both CF and CNT have high efficiency as conductive filler due to fibrous shapes, CF can be used as structural reinforcement due to its high stiffness, and CNT is one of the most commercially used nano-fillers. It is obvious that polymer/CF/CNT composites have great importance from both scientific and engineering points of

view. The aim of this section is to understand the mechanism of the synergistic effect produced by a mixture of CF and CNT. CF and two types of CNTs with different compatibility with polymer were studied. Differences in the CNT agglomerate size and wettability according to the CNT–polymer compatibility were determined through transmission electron microscopy (TEM) and scanning electron microscopy (SEM). The synergistic effect on electrical properties and mechanical properties was investigated. The mechanisms producing the synergistic effect between CF and CNT were identified.

3.2 Experimental

3.2.1 Materials

CF and two types of CNTs were used in this study. The CF used was PX35CA0250-65 supplied by Zoltek (Canada); they had a diameter of 7 μm and a cutting length of 6 mm. CNS PU-encapsulated flakes (PU-CNT) supplied by Applied Nanostructured Solutions, LLC (USA), which was sized with polyurethane as the CNTs were grown in an aligned form, was used [18]. Another type of CNT, CM-150 (N-CNT), supplied by Hanwha Chemical Corp. (Republic of Korea), in which nanotubes were entangled with each other because of their synthesis via the chemical vapor deposition method using a general floating catalyst reactor, was used. As can be seen in Figure 3.1, PU-CNTs were not entangled with each other because they were grown in an aligned form, whereas N-CNTs were entangled with each other.

As the matrix material, polyamide 6,6 (PA), supplied by Leona-1200 of Asahi Kasei Co., Ltd. (Japan), was employed. It had the following properties: melting temperature, 260°C; melt flow index, 125 g/10 min (270°C, 2.16 kg); and density, 1.135 g/cm^3.

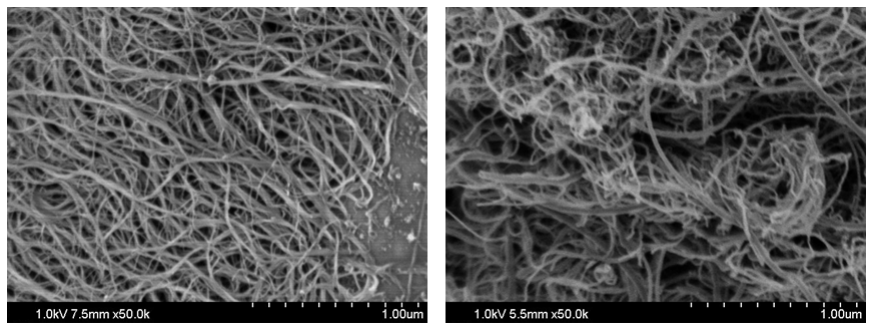

(a) (b)

Figure 3.1. SEM images of CNTs: (a) PU-CNT, (b) N-CNT.

3.2.2 Preparation of composite samples

Conductive composite pellets were fabricated by compounding PA with conductive fillers at a feeding rate 60 kg/h and a screw velocity of 200 rpm at 280°C by using a twin extruder (JSW, Japan) with an L/D ratio of 44 and a diameter of 45 mm. To identify the characteristics of CF and CNTs experiments were conducted in which each filler was added to PA separately. PA/PU-CNT composites were fabricated by varying the PU-CNT content to 0.2, 0.5, 0.7, and 1.0 wt% (0.125, 0.312, 0.437, and 0.625 vol%, respectively) in PA. PA/N-CNT composites were fabricated under the same conditions as described above but with N-CNT instead of PU-CNT. Further, PA/CF composites were fabricated by varying the CF content to 5, 15, 25, 35, and 45 wt% (3.17, 9.89, 17.2, 25.1, and 33.7 vol%, respectively) in PA. Furthermore, samples were fabricated by mixing CF and CNT to observe their synergistic effect. PA/CF5/PU-CNT composites were fabricated with a CF content of 5 wt% and then varying the PU-CNT content to 0.2, 0.5, and 1.0 wt% in PA. PA/CF5/N-CNT composites were fabricated under the same conditions as described above. Additionally, PA/CF25/PU-CNT composites were fabricated with a CF content of 25 wt% and then varying the PU-CNT content to 0.2, 0.5, and 1.0 wt% in PA. PA/CF25/N-CNT composites were also fabricated under the same conditions as described above. The fabricated pellets were dried at 120°C for 2 h in a dehumidifying dryer, and specimens were fabricated for property evaluation at 290°C by using a 40-mm diameter and 150-ton injection machine (Woojin Selex, Republic of Korea). The specimens were fabricated as shown Figure 3.2.

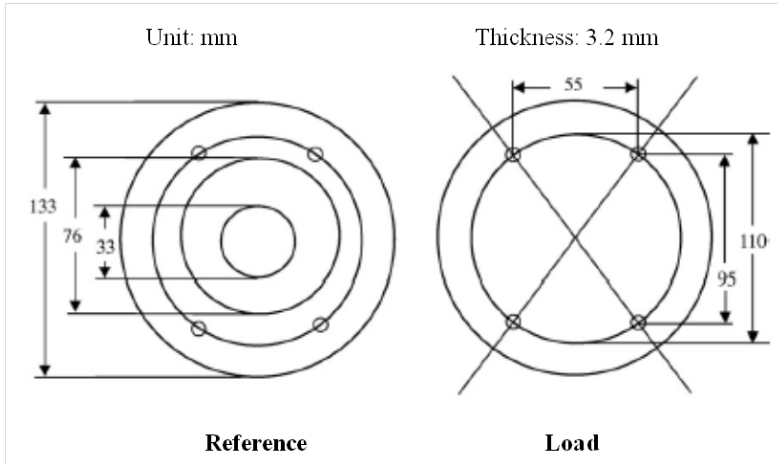

(a)

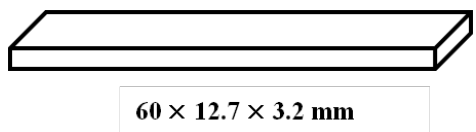

(b)

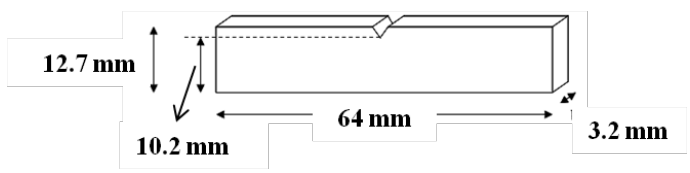

(c)

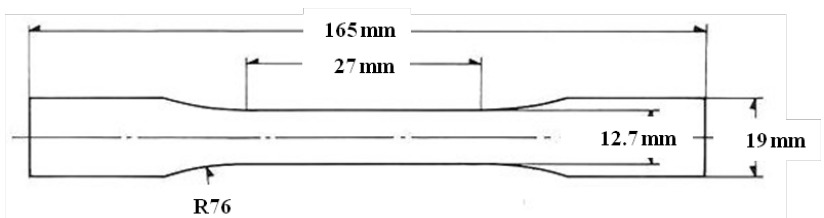

(d)

Figure 3.2. Specimens for properties evaluation (a) EMI SE (b) electrical conductivity (c) notched Izod impact strength (d) tensile strength

3.2.3 Measurements

The morphology of CNT and CF in the PA matrix was observed using transmission electron microscope (TEM; JEM-1400, JEOL, Japan) and field-emission scanning electron microscopy (FE-SEM; SU-70, Hitachi, Japan). For samples with an electrical conductivity higher than 10^{-7} S/cm, the electrical conductivity was measured by a four-point probe method at room temperature. The dimensions of the sample for electrical conductivity measurements were 60 mm×12.7 mm×3.2 mm. A constant current was applied using a source meter (2400, Keithley, USA) to the outer probes of the four contacts, and the corresponding voltage was measured between inner probes using a nanovolt meter (2182, Keithley, USA). For samples with an electrical conductivity lower than 10^{-7} S/cm, the measurements were performed by a two-point probe method using only a source meter. Electromagnetic interference shielding efficiency (EMI SE) of the composites at room temperature was measured using E8362B (Agilent, USA) according to the method described in ASTM D4935. The notched Izod impact strength of the composites was measured according to the ASTM D256 test method by using DG-1B (Toyoseki, Japan). The thickness of the test specimen was about 3.2 mm. Its tensile strength was measured according to ASTM D638 (UTM, 5969, Instron, USA). The crosshead speed was 5 mm/min, and the specimen was the type I of the dog-bone-shaped specimen with 3.2 mm.

3.3 Results and discussion

3.3.1 Individual effect of CF and CNT

In order to determine the characteristics of CF, PU-CNT, and N-CNT as conductive fillers, the electrical conductivity of composites fabricated by adding each of the fillers separately was measured. As shown in Figures 3.3 and 3.4, PA/PU-CNT composites showed better electrical conductivity than PA/N-CNT composites. PA/CF composites showed lower electrical conductivity than PA/PU-CNT and PA/N-CNT even at 3.17 vol% but showed higher electrical conductivity than both at content above 9.89 vol%. The percolation equation, which considers the percolation phenomena of each of the fillers, is given by Equation (1) [19]:

$$\sigma_c = \sigma_f(p - p_c)^t \quad (1)$$

where σ_c is the electrical conductivity of the composite, σ_f is the electrical conductivity of the filler, p is the volume fraction of the filler, p_c is the percolation threshold and t is a critical exponent related to the dimensionality of the system. On the basis of the abovementioned experimental data, percolation parameters for the conductive fillers were acquired and are listed in Table 1.

PU-CNT and N-CNT had significantly lower percolation thresholds than CF because CNT has a larger aspect ratio than CF. However, although the electrical conductivity of CNT (~10^5 S/cm [20]) is larger than that of CF (~10^3 S/cm [21]), the filler conductivity of PA/CNT was lower than that of PA/CF. Chang et al. estimated the percolation threshold on the basis of the excluded volume theory and reported that assuming a CNT diameter of 15 nm and a length of 3 μm results in a theoretical value of the percolation threshold between 0.34 and 0.68 vol%. In their experiment, the percolation threshold was smaller than its theoretical value (p_c = 0.02 vol%) and the filler conductivity was also smaller than the electrical conductivity of CNT (σ_f = 14.5 S/cm) [6].

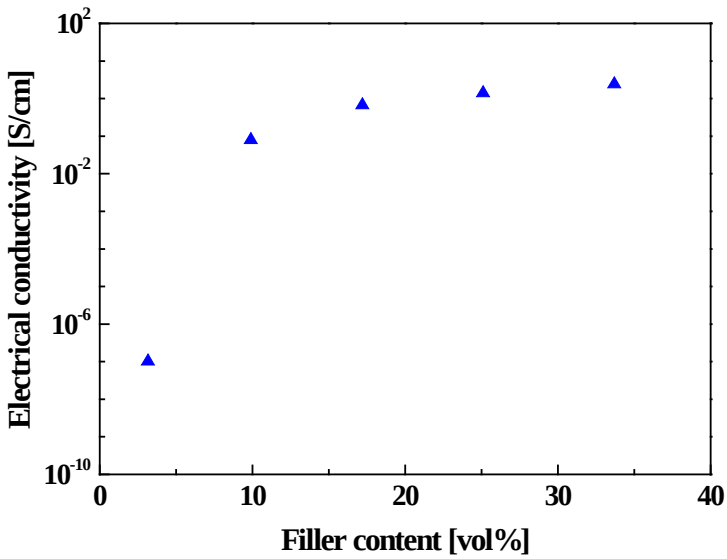

(a)

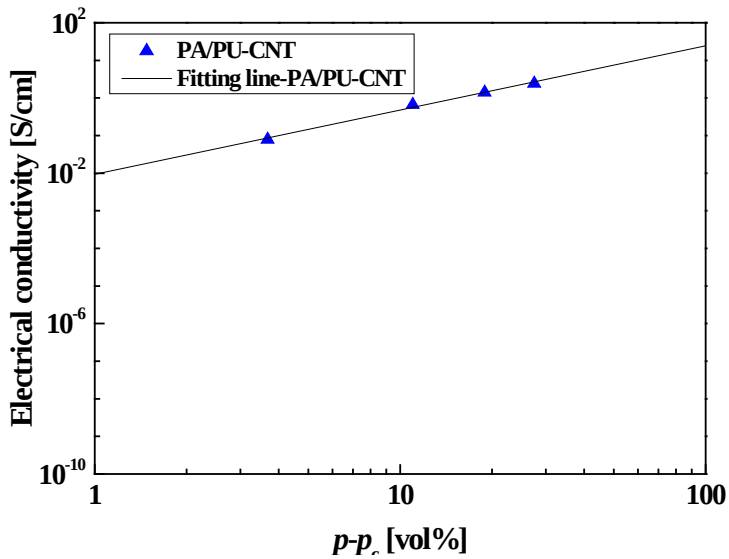

(b)

Figure 3.3. (a) Electrical conductivity of PA/CF composites, (b) a log–log plot for electrical conductivity of PA/CF composites as a function of (p–p_c) with fit line determined using Equation (1).

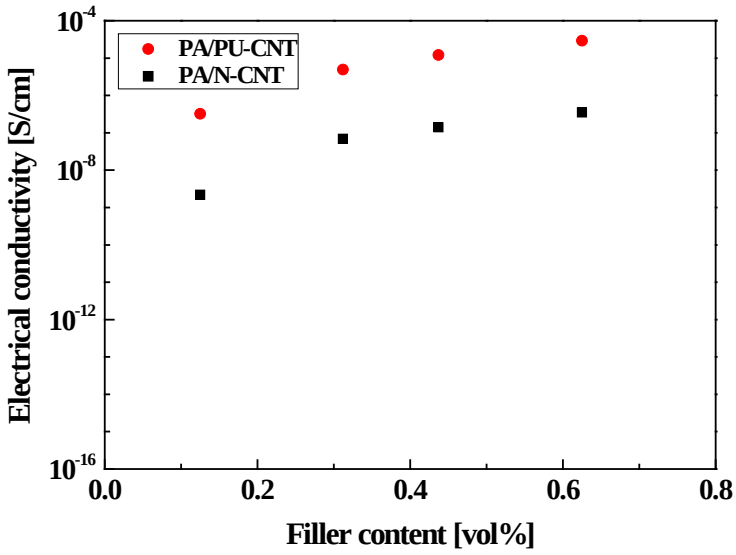

(a)

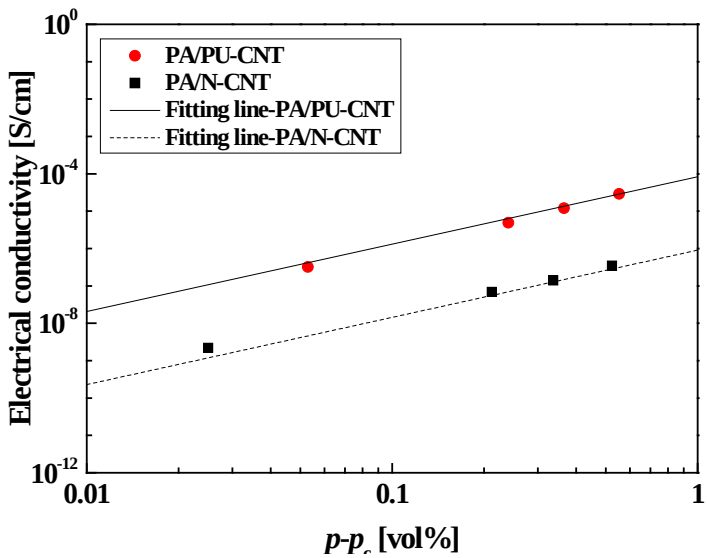

(b)

Figure 3.4. (a) Electrical conductivity of PA/CNT composites, (b) a log–log plot for electrical conductivity of PA/CNT composites as a function of (p–p_c) with fit line determined using Equation (1).

Table 3.1. Percolation parameters of PA/CNT and PA/CF composites.

	p_c (vol.%)	σ_f (S/cm)	t
CF	6.21	$9.29*10^{-3}$	1.71
PU-CNT	0.072	$8.28*10^{-5}$	1.91
N-CNT	0.11	$9.12*10^{-7}$	1.64

This result was attributed to the decreasing filler conductivity with increasing effective volume. This was because the volume fraction of CNT to reach the percolation threshold decreased with increasing effective volume as electron hopping exceeded the effective volume of CNT and the filler conductivity decreased to become equal to the overall effective volume conductivity [22]. Similarly, the percolation threshold of filler with a large aspect ratio can be calculated using Equation (2) according to the excluded volume theory [23]:

$$1 - \exp\left(-\frac{1.4\,V}{V_e}\right) \leq p_c \leq 1 - \exp\left(-\frac{2.8\,V}{V_e}\right) \quad (2)$$

where V is the volume of a single filler and V_e is the excluded volume, which is defined as the volume surrounding an object that cannot penetrate other objects of the same shape. Fillers with a randomly oriented fiber shape have volumes given by Equation (3) [24]:

$$V_e = \frac{4\pi}{3}D^3 + 2\pi D^2 L + \frac{\pi}{2}DL^2 \quad (3)$$

where D is the filler diameter and L is the filler length. Assuming that the CF diameter and length are 7 and 100 μm, respectively, the theoretical value of the percolation threshold can be estimated, and it will be within the range 3.7–7.2 vol%. For CF, the calculated percolation threshold matches the theoretical one, and in contrast with CNT, its increase in the effective volume due to electron hopping is not very large; moreover, the decrease in the filler conductivity is small, and thus, its filler conductivity is larger than that of CNT.

To determine the cause of this phenomenon in more detail, the morphology of the PA/PU-CNT and PA/N-CNT composites was observed via TEM. As shown in Figures 3.5 and 3.6, agglomerates of PU-CNT were formed and were larger than those of N-CNT; however, the agglomerates of PU-CNT were less dense than those of N-CNT. This is because PU-CNT was sized with polyurethane, and thus, the compatibility with the PA matrix was better, thereby facilitating distribution and forming larger agglomerates. The size of the agglomerates seemed to be

determined by the compatibility between the filler and matrix rather than by the filler content [7]. Even when the filler content was increased from 0.312 vol% (Figures 3.5 (a) and 3.6 (a)) to 0.625 vol% (Figures 3.5 (c) and 3.6 (c)), the size of the agglomerates did not significantly change except for showing a difference between PU-CNT and N-CNT. The size of the PU-CNT agglomerates was 10–40 μm, whereas that of the N-CNT agglomerates was 3–15 μm. Thus, PU-CNT formed larger agglomerates, resulting in the larger effective volume and forming the more efficient electrical conductive network [25-26].

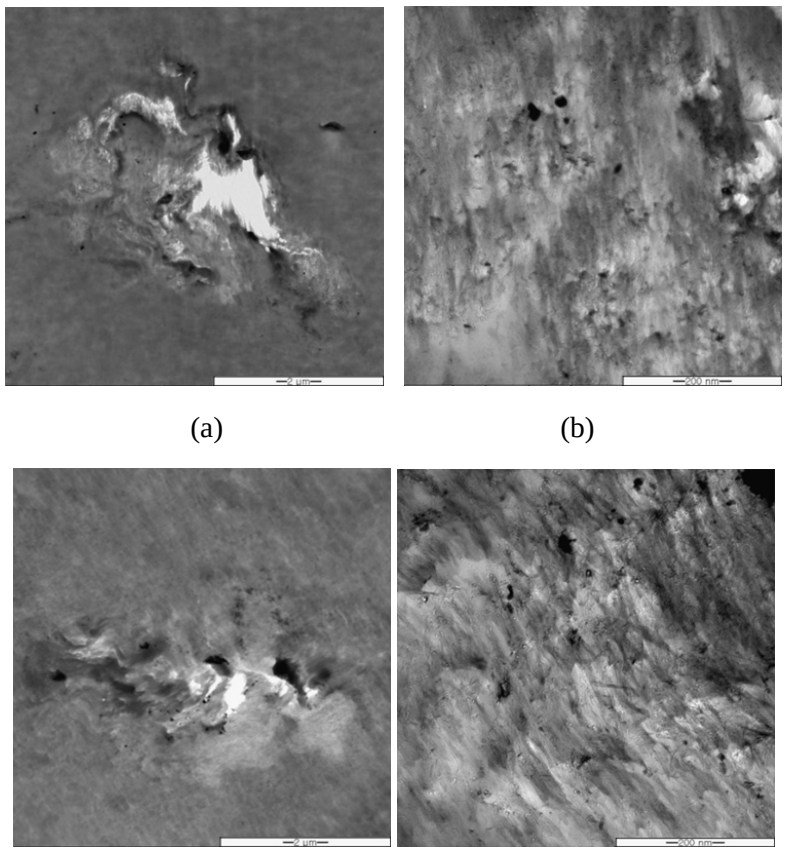

(a) (b)

(c) (d)

Figure 3.5. TEM images of PA/CNT composites: (a) PA/PU-CNT 0.5 wt%, (b) at high magnitude, (c) PA/PU-CNT 1.0 wt%, (d) at high magnitude

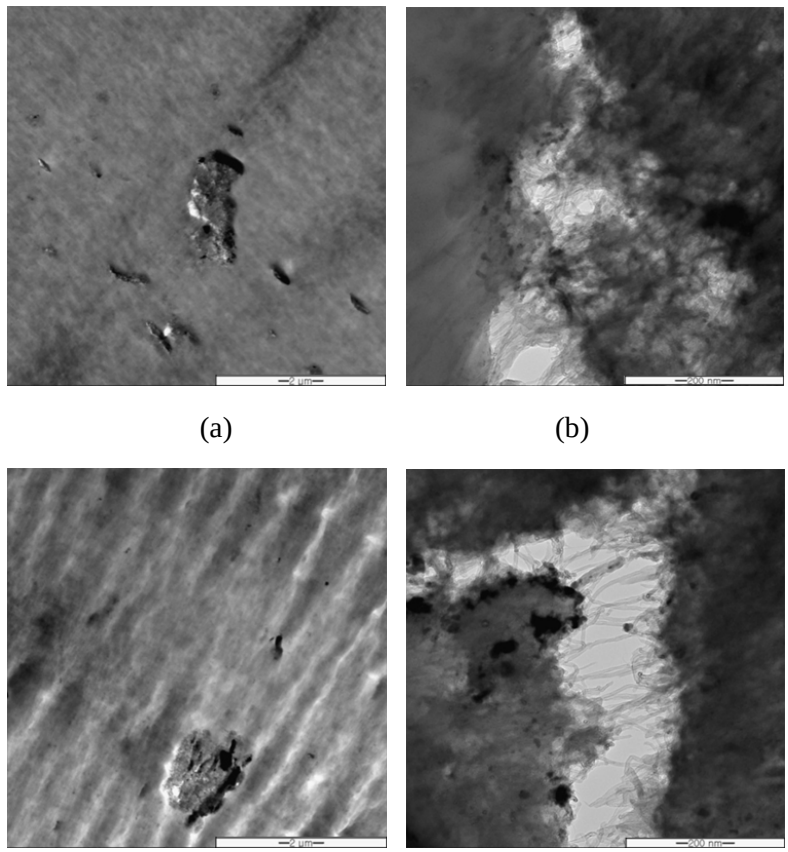

(a) (b)

(c) (d)

Figure 3.6. TEM images of PA/CNT composites: (a) PA/N-CNT 0.5 wt%, (b) at high magnitude, (c) PA/N-CNT 1.0 wt%, (d) at high magnitude

3.3.2 Enhancement the filler efficiency of CF and CNT

To observe the synergistic effect of CF and CNT, they were added to PA simultaneously, and the electrical conductivity of the resulting PA/CF/CNT composites were measured. With respect to two compositions, CF 3.17 vol% (which was less than the CF percolation threshold) and CF 17.2 vol% (which was higher than the CF percolation threshold), experiments were conducted by varying the CNT content to 0.125, 0.312, and 0.625 vol%. In addition, experiments were conducted on PA/CF composites for comparative evaluation. As shown in Figures 3.7 and 3.8, both the electrical conductivity and EMI shielding efficiency showed a synergistic effect due to CF and CNT. PU-CNT showed larger efficiency than CF for CF content of 3.17 and 17.2 vol%. On the contrary, N-CNT showed efficiency comparable to that of CF when the CF content was 3.17 vol%, and showed higher efficiency than that of CF when the CF content was 17.2 vol%. However, the efficiency of N-CNT was lower than that of PU-CNT. This was due to the difference between the compatibilities of PU-CNT and N-CNT with PA, as shown in Figures 3.5 and 3.6.

In order to observe CNT in the PA/CF/CNT composites, PA/CF/CNT samples were cooled using liquid nitrogen. The samples fractured in this process without plastic deformation, and the fractured surfaces were then observed via SEM. Figure 3.9 shows samples containing CF 3.17 vol% and CNT 0.625 vol%; here, agglomerates of PU-CNT and N-CNT can also be observed. Because of the fractured surfaces, the size of the agglomerates could not be evaluated accurately. However, this result reaffirmed that PU-CNT were better impregnated with PA than N-CNT. As shown in Figure 3.10, it was difficult to observe agglomerates through SEM when the CF content was 17.2 vol%; moreover, both PU-CNT and N-CNT were distributed over PA.

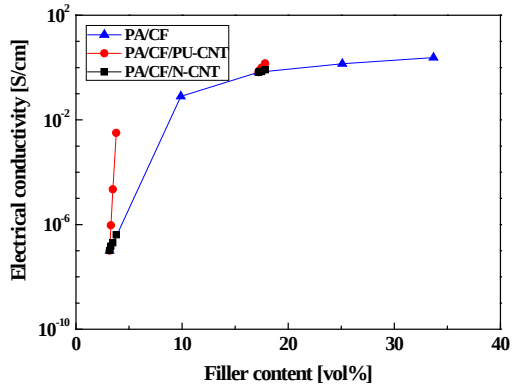

(a)

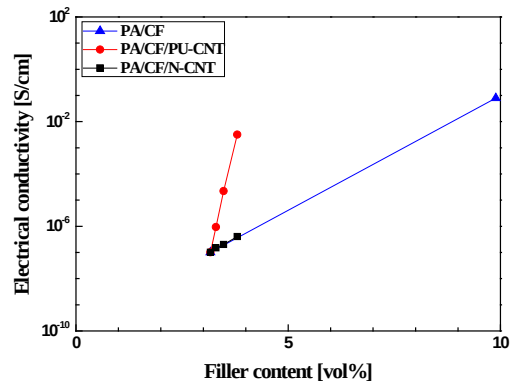

(b)

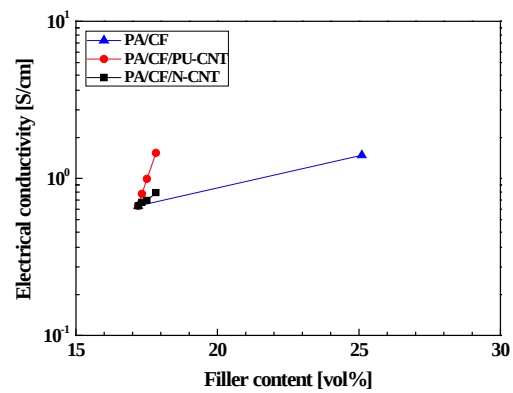

(c)

Figure 3.7. Electrical conductivity of PA/CF/CNT composites: (a) at overall filler content, (b) at CF 5–15 wt%, (c) at CF 25–35 wt%.

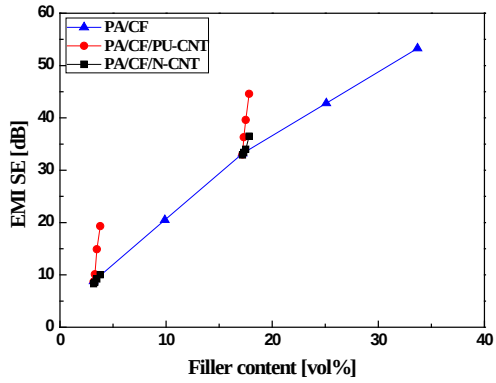

(a)

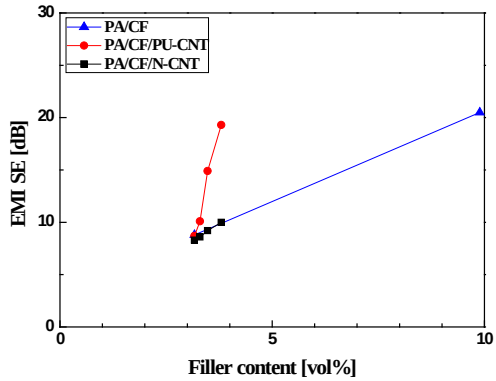

(b)

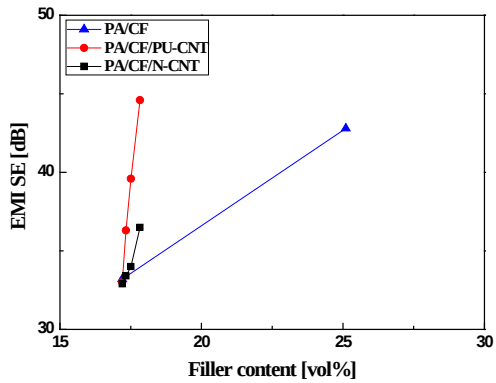

(c)

Figure 3.8. EMI shielding efficiency at 1GHz of PA/CF/CNT composites: (a) at overall filler content, (b) at CF 5–15 wt%, (c) at CF 25–35 wt%.

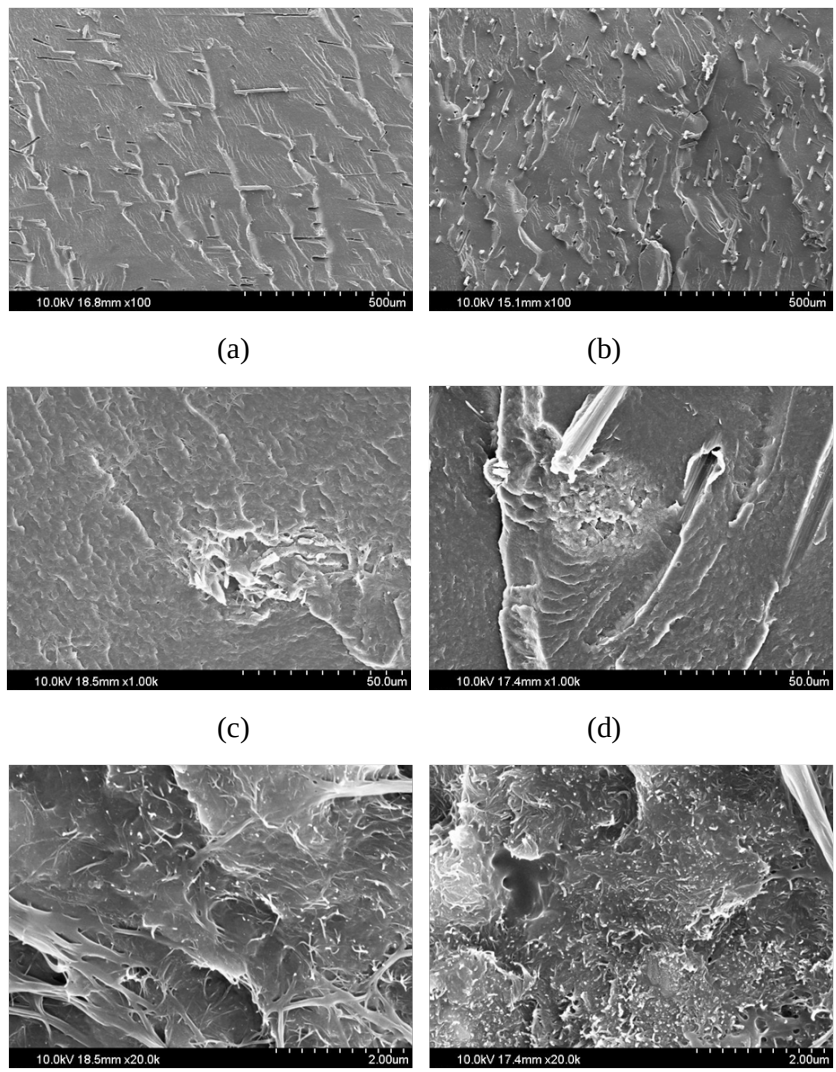

Figure 3.9. SEM images of factured surface of PA/CF 5 wt%/CNT 1.0 wt% composites: at low magnitude (a) PU-CNT, (b) N-CNT, at medium magnitude (c) PU-CNT, (d) N-CNT, at high magnitude (e) PU-CNT, (f) N-CNT

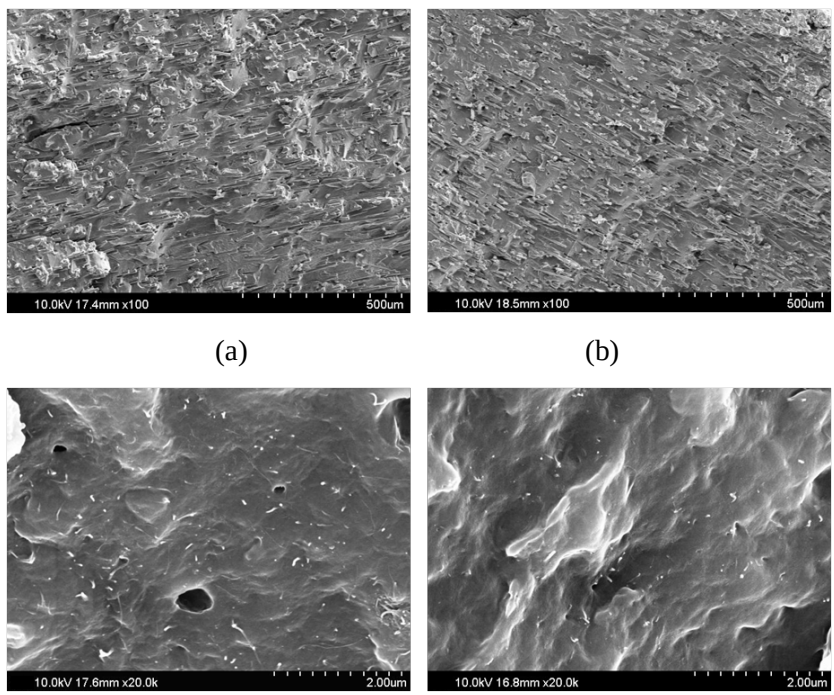

Figure 3.10. SEM images of the fractured surface of PA/CF 25 wt%/CNT 1.0 wt% composites: at low magnitude (a) PU-CNT, (b) N-CNT, at high magnitude (c) PU-CNT, (d) N-CNT.

To determine whether CNT agglomerates existed in the composites when the CF content was 17.2 vol%, PA/CF/CNT composites were hot-pressed and a thin film was fabricated, thereby allowing observation of CNT agglomerates by using an optical microscope. As shown in Figure 3.11, in PA/CF/PU-CNT composites, agglomerates were observed under CF 3.17 vol% but no agglomerates were observed under CF 17.2 vol%. On the contrary, in PA/CF/N-CNT composites, agglomerates were observed under both CF 3.17 and 17.2 vol%, and they were smaller than those observed in PA/CF/PU-CNT composites. As the CF content increased, CNT distribution improved owing to the increase of the matrix viscosity and the physical contact between CF and CNT agglomerates. The agglomerates of N-CNT were smaller than those of PU-CNT, and thus, the distribution effect due to CF was less significant. As a result, N-CNT produced a lesser synergistic effect than PU-CNT, whereas some synergistic effect was obtained at CFs 17.2 vol% and N-CNT 0.625 vol%, which may have some distribution effect. Figure 3.12 shows the mechanism of the synergistic effect of CF and CNT schematically.

Additionally, the tensile strength and notched Izod impact strength of the PA/CF/CNT composites were measured. As shown in Figures 13 and 14, PU-CNT had good compatibility with PA; this facilitated their impregnation and addition to PA, resulting in a reinforcing effect. However, N-CNT showed degradation in mechanical properties owing to low compatibility with PA [27]. Improvements in the mechanical properties were also observed to be more in PU/CNT than in PA/CF when the N-CNT distribution was achieved owing to a large CF content (PA/CF 17.2 vol%/CNT 0.625 vol%).

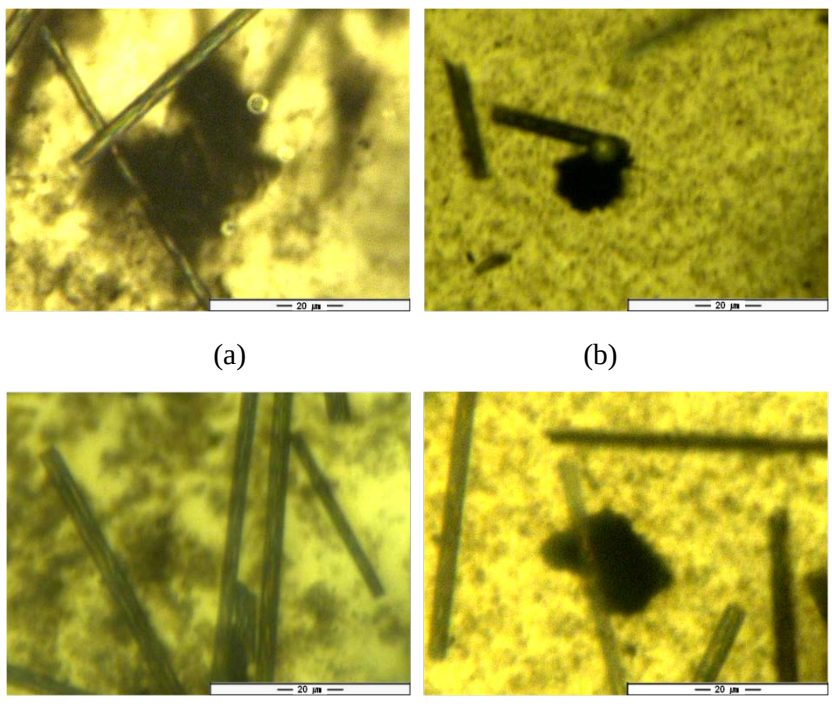

(a) (b)

(c) (d)

Figure 3.11. Optical microscopy images of PA/CF/CNT composites: at CF 5 wt% (a) PU-CNT 1.0 wt%, (b) N-CNT 1.0 wt%, at CF 25 wt% (c) PU-CNT 1.0 wt%, (d) N-CNT 1.0 wt%.

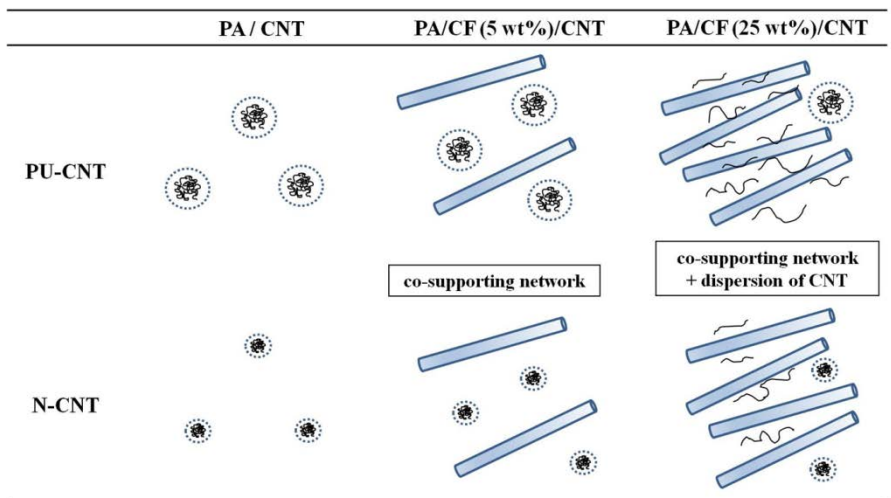

Figure 3.12. Schematic picture of enhancing the filler efficiency of CF and CNT.

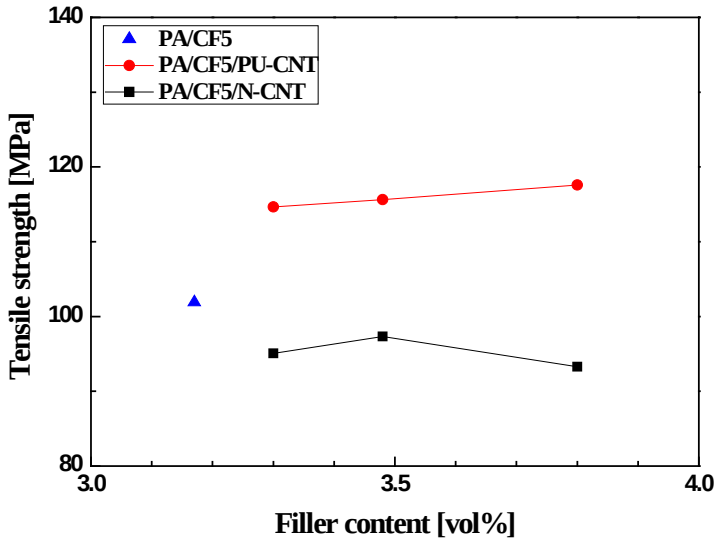

(a)

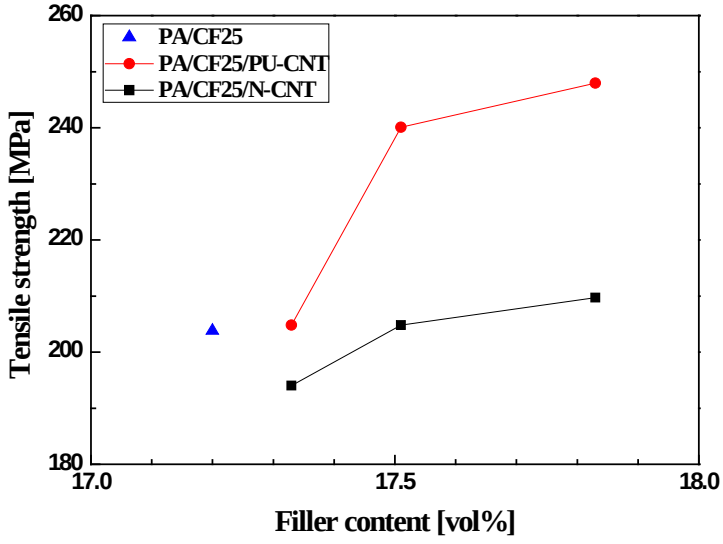

(b)

Figure 3.13. The tensile strength of PA/CF/CNT composites; (a) CF 5 wt%, (b) CF 25 wt%.

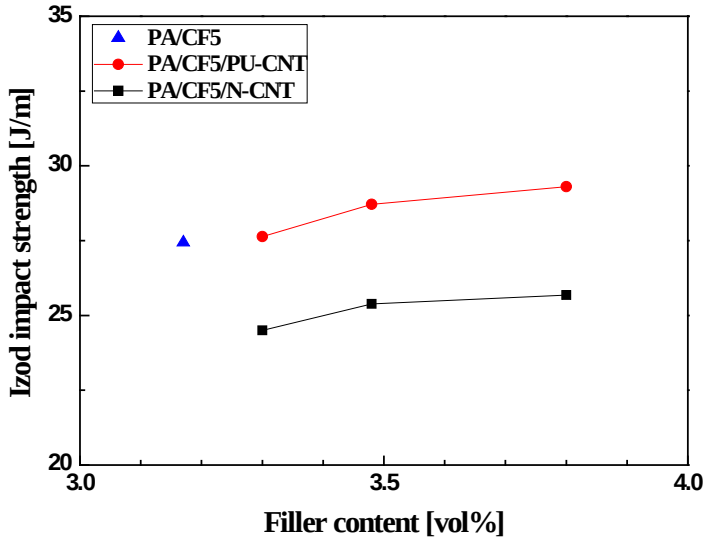

(a)

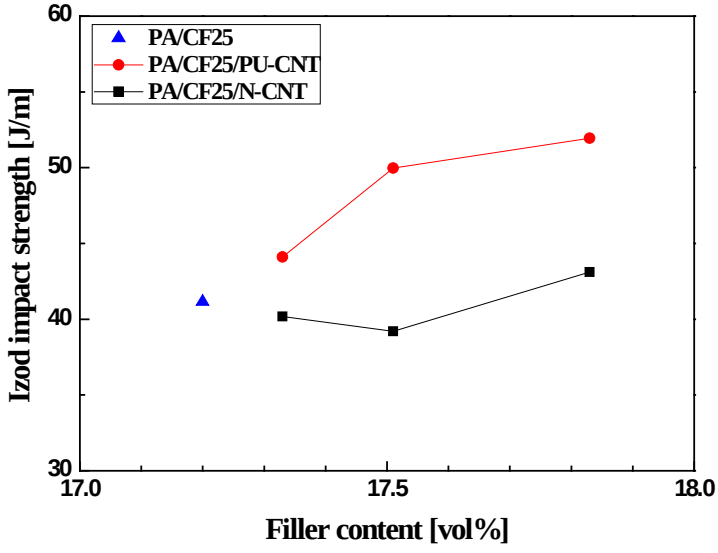

(b)

Figure 3.14. The notched Izod impact Strength of PA/CF/CNT composites; (a) CF 5 wt%, (b) CF 25 wt%.

3.4 Conclusions

The CNT morphology of PA/CF/CNT composites was observed to study the synergistic effect of CF and CNT, which are different in terms of their compatibility with the matrix, with regard to electrical conductivity. It is found that PU-CNT, which had better compatibility with the matrix within the composites than N-CNT, formed larger agglomerates. Moreover, their impregnation with the matrix was better as well, resulting in better electrical properties and mechanical properties than those of the composites with N-CNT. Moreover, CNT had a larger effective volume than CF, such that CNT helped improve the formation of conductive network of CF, thereby generating a synergistic effect when CNT and CF were mixed together. As the CF content increased, the CNT distribution was improved owing to the increase of the matrix viscosity and the physical contact between CF and CNT agglomerates, thereby increasing the synergistic effect of CF and CNT. In other words, PU-CNT, which had good dispersibility, produced a synergistic effect even at a small CF content; as the CF content increased, this synergistic effect increased. N-CNT, which had low dispersibility, had a minimal synergistic effect when the CF content was small; however, as the CF content increased, the synergistic effect was produced as soon as the N-CNT dispersibility improved.

Bibliography

[1] Balberg I.: A comprehensive picture of the electrical phenomena in carbon black–polymer composites. Carbon, 40, 139-143 (2002).

[2] Sengupta R., Bhattacharya M., Bandyopadhyay S., Bhowmick A. K.: A review on the mechanical and electrical properties of graphite and modified graphite reinforced polymer composites. Progress in Polymer Science, 361, 638-670 (2011).

[3] Heo S. I., Yun J. C., Oh K. S., Han K. S.: Influence of particle size and shape on electrical and mechanical properties of graphite reinforcedconductive polymer composites for the bipolar plate of PEM fuel cells. Advanced Composite Materials, 15, 115-126 (2006).

[4] Chung D. D. L.: Comparison of submicron-diameter carbon filaments and conventional carbon fibers as fillers in composite materials. Carbon, 39, 1119-1125 (2001).

[5] Dani A., Ogale A. A.: Electrical percolation behavior of short-fiber composites: Experimental characterization and modeling. Composites Science and Technology, 56, 911-920 (1996).

[6] Deng S. H., Zhao J. J., Lin Q. F., Fan C. J., Zhou X. D.: Formation of interfacial network structure via photo-crosslinking in carbon fiber/epoxy composites. Express Polymer Letters, 8, 505-516 (2014).

[7] Chang L., Friedrich K., Ye L.: Evaluation and visualization of the percolating networks in multi-wall carbon nanotube/epoxy composites. Journal of Material Science, 44, 4003-4012 (2009).

[8] Bauhofer W., Kovacs J. Z.: A review and analysis of electrical percolation in carbon nanotube polymer composites. Composites Science and Technology, 69, 1486-1498 (2009).

[9] Xie X. L., Mai Y. W., Zhou X. P.: Dispersion and alignment of carbon nanotubes in polymer matrix: A review. Materials Science and Engineering: R:

Reports, 49, 89-112 (2005).

[10] Auilar J. O., Bautista-Quijano J. R., Aviles F.: Influence of carbon nanotube clustering on the electrical conductivity of polymer composite films. Express Polymer Letters, 4 292-299 (2010).

[11] Song Y. S., Youn J. R.: Influence of dispersion states of carbon nanotubes on physical properties of epoxy nanocomposites. Carbon, 43, 1378–1385 (2005).

[12] Ma P., Liu M., Zhang H., Wang S., Wang R., Wang K., Wong Y., Tang B., Hong S., Paik K., Kim J.: Enhanced electrical conductivity of nanocomposites containing hybrid fillers of carbon nanotubes and carbon black. Applied Materials Interfaces, 1, 1090-1096 (2009).

[13] Zhang S. M., Lin L., Deng H., Gao X., Bilotti E., Peijs T., Zhang Q., Fu Q.: Synergistic effect in conductive netwoks constructed with carbon nanofillers in different dimensions. Express Polymer Letters, 6, 159-168 (2012).

[14] Safdari M., Al-Haik M. S.: Synergistic electrical and thermal transport propertes of hybrid polymeric nanocomposites based on carbon nanotubes and graphite nanoplatelets. Carbon, 64, 111-21 (2013).

[15] Thongruang W., Spontak R. J., Balik C. M.: Correlated electrical conductivity and mechanical property analysis of high-density polyethylene filled with graphite and carbon fiber. Polymer, 43, 2279-2286 (2002).

[16] Yang H., Gong J., Wen X., Xue J., Chen Q., Jiang Z., Tian N., Tang T.: Effect of carbon black on improving thermal stability, flame retardancy and electrical conductivity of polypropylene/carbon fiber composites. Composites Science and Technology, 113, 31-37 (2015).

[17] Shen L, Wang F. Q., Yang H., Meng Q. R.: The combined effects of carbon black and carbon fiber on the electrical properties of composites based on polyethylene or polyethylene/polypropylene blend. Polymer Testing, 30, 442-448 (2011).

[18] Peterson B. W., Jones M. L., Shah T. K., Alberding M.R.: Systems and

methods for continuously producing carbon nanostructures on reusable substrates. US patent, US20130101495 A1 (2013).

[19] Stauffer D., Aharony A.: Introduction to percolation theory. Taylor and Francis, London (1994).

[20] Ebbesen T. W., Lezec H. J., Hiura H., Bennett J. W., Ghaemi H. F., Thio T.: Electrical conductivity of individual carbon nanotubes. Nature, 382, 54-56 (1996).

[21] Jana P.B., Chaudhuri S., Pal A. K., De S. K.: Electrical conductivity of short carbon fiber-reinforced polychloroprene rubber and mechanism of conduction. Polymer Engineering & Science, 32, 448-456 (1992).

[22] Feng C., Jiang L.: Micromechanics modeling of the electrical conductivity of carbon nanotube (CNT)–polymer nanocomposites. Composites Part A: Applied Science and Manufacturing, 47, 143-149 (2013).

[23] Celzard A., McRae E., Deleuze C., Dufort M., Furdin G., Mareche J. F.: Critical concentration in percolating systems containing a high-aspect-ratio filler. Physical Review B, 53, 6209-6214 (1996).

[24] Balberg I., Anderson C. H., Alexander S., Wagner N.: Excluded volume and its relation to the onset of percolation. Physical Review B, 30, 3933-3943 (1984).

[25] Li J., Ma P. C., Chow W. S., To C. K., Tang B. Z., Kim J.: Correlations between percolation threshold, dispersion state, and aspect ratio of carbon nanotubes. Advanced Functional Materials, 17, 3207-3215 (2007).

[26] Gao L., Chou T. W., Thostenson E. T., Godara A., Zhang Z., Mezzo L.: Highly conductive polymer composites based on controlled agglomeration of carbon nanotubes. Carbon, 48, 2649-2651 (2010).

[27] Hwang G.L., Shieh Y.T., Hwang K.C.: Efficient load transfer to polymer-grafted multiwalled carbon nanotubes in polymer composites. Advanced Functional Materials, 14, 487-491 (2004).

Chapter 4. Polymer/metal filler system

4.1 Introduction

In this section, polymer/metal filler system was investigated for compensating the limitations of polymer/carbon filler system. Carbon fillers typically requires very high loadings to produce conductivity, causing increases in viscosity, poor degassing behaviour, and degradation of mechanical performance in some cases because carbon fillers remain solid state during compounding them with polymer matrix.

Metal fillers, which are good electrically conductive materials, can be used as conductive filler as well. For metal fillers, there are magnesium, aluminum, nickel, copper, silver and stainless steel, etc [1-3]. These metal fillers, except for magnesium and aluminum, tend to increase the overall weight of composites due to their high densities, and they also yield a poor processability when large amounts are added. Magnesium has a low corrosion resistance and need to be treated for corrosion protection [4]. In the case of aluminum, a dense oxidation layer formed on the surface increases the electrical resistivity of the composite [5].

An interesting approach was proposed to maintain processability at high filler loading by applying a low-melting-point metal alloy (LMA) by Zhang et. al [6]. Since LMA melts at the processing temperature of the polymer, it does not increase the viscosity of the composite due to the low viscosity of molten LMA. However, as LMA droplets were fused into large domains above melting temperature, electrical networks was not formed, resulting in a low electrical conductivity under 10^{-15} S/cm [7]. To disperse the domains of LMA, solid metal particles were combined with LMA. Small loadings of nickel particulates in a polymer, along with the LMA, prevented coalescence of the molten LMA droplets resulting in a

high conductivity of ~10^2 S/cm [8]. Imparting copper fibers and LMA with a polymer improved the dispersability of LMA and increased the filler efficiency due to large aspect ratios of LMA domains, resulting in a very high conductivity of ~10^4 S/cm [9]. The mechanisms can be suggested that the solid particle acts as a mechanical aid; the solid particle increases the viscosity of the LMA droplet and slows the coalescence process. However, LMA/solid metal particle also has a high density, the problem of increasing the weight of the polymer composite still remains.

In order to solve these problems, a polymer/LMA/elongated light metal composite is proposed in this study. LMA was designed to be mixed with the light metal overcoming the difference of the densities of LMA and the light metal. As it encapsulates the light metal in the composite, it can play the role of blocking the increase in electrical resistance due to oxidation of the surface of the light metal. And it melts at the processing temperature of polymer and maintains processability of the composites during compounding with polymer. The elongated light metal reduces the density of the metal filler to minimize the increase in the weight of the composite. It also increases the efficiency as conductive filler by presenting a fibrous form. Furthermore, it improves the dispersibility of the LMA domain by maintaining a solid state during compounding. The resulting composites exhibited high electrical conductivity and enhanced mechanical properties.

4.2 Experimental

4.2.1 Material selection

I have designed a conductive composite composed of polymer, low melting point metal alloy (LMA) and elongated light metal. Polystyrene-acrylonitrile (SAN) was used as polymer matrix and was supplied by Samsung SDI Co., Ltd. (Republic of Korea). The physical properties of SAN are as follows: The acrylonitrile content of SAN is 24.5 wt%, the weight-average molecular weight is 140,000, the melt flow index is 2.7 g/10 min in 200℃/5.86 kg condition, and the notched Izod impact strength is 21.6 J/m. Since the density of aluminum (Al) is 2.7 g/cm^3 and thus it can lower the density of conductive filler (LMA/elongated light metal), Al was selected as the light metal. Al powder having the particle size of 44~100 ㎛ was used.

As can be seen in Figure 4.1, LMA becomes the matrix of LMA/elongated light metal in the first and second processes but act as conductive filler which is dispersed in the polymer matrix during the third process. Tin (Sn) with the melting point of 230℃ is a good candidate for LMA since it has a similar melting temperature to the processing temperature of SAN. However, since the density of Sn is 7.29 g/cm^3, which is much higher than that of Al, the Al powers floated on top of the liquid Sn during the mixing process. The large difference in density made it very difficult to mix Al powders in liquid Sn. With regard to flotation and sedimentation, the particle velocity in the liquid under gravity would be Equation (1) [10];

$$v = \frac{2a^2\,(\rho_P - \rho)}{9\eta}\,g \qquad (1)$$

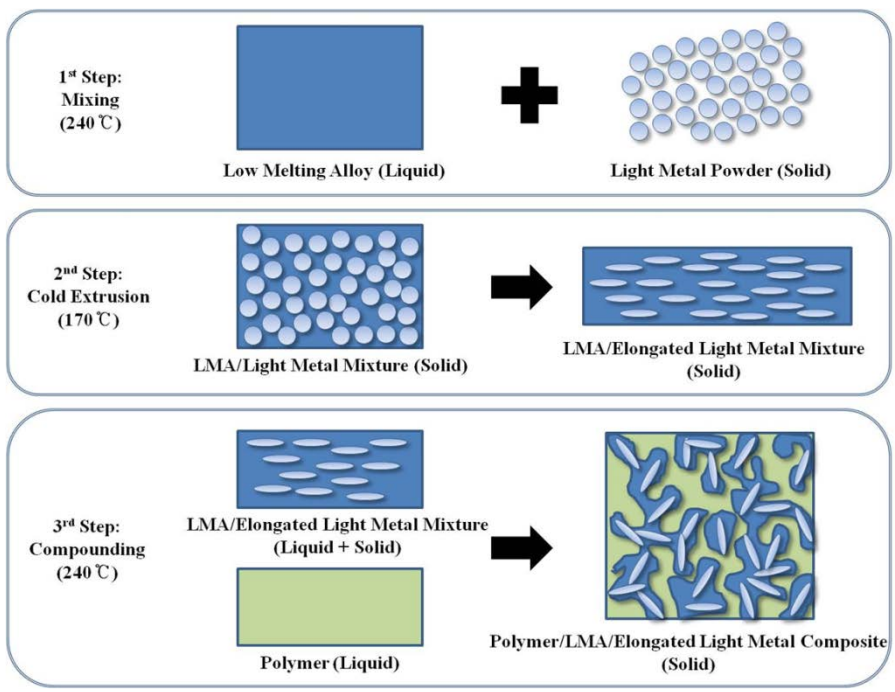

Figure 4.1. The technological process of preparing polymer/LMA/elongated light metal composite.

where v is the velocity of the particle, a is the radius of the particle, ρ_P is the density of the particle, ρ is that of the liquid, η is the viscosity of the liquid and g is the acceleration of gravity. Assuming that a is 70 ㎛, ρ_P is 2.7 g/cm^3, ρ is 7.29 g/cm^3, and η is 1.5 mPa·s [11], the floating velocity of the Al powder is 3 mm/s. The velocity is too fast to mix Al powder into liquid Sn. When the density of the liquid and particle and the radius of the particle are fixed in Equation (1), the method for lowering the floating velocity is to increase η. However, for pure metal, it is difficult to control the viscosity since the viscosity will rapidly change during the phase transition from solid to liquid as can be seen in Figure 4.2. Thus in order to increase the viscosity, a coexisting region with liquid and solid at the processing temperature of about 270℃ is needed. For a general solid-liquid suspension, the viscosity is a function of the fraction of solid. An equation which has been obtained from the empirical data can be expressed in the following Equation (2) [12];

$$\frac{\eta_s}{\eta_0} = 1 + 2.5\Phi + 10.05\Phi^2 + A\exp(B\Phi) \quad (2)$$

where η_s is the viscosity of the solid-liquid suspension, η_0 is the viscosity of the pure liquid, Φ is the volume fraction of solid in the suspension, and A and B are constants which are found to be 0.00273 and 16.6 respectively. Sn-Zn30 alloy having Sn 70 wt% with zinc (Zn) 30 wt% was selected, which has solidus temperature of 230℃, liquidus temperature of 320℃, and solid volume fraction of 0.7 at 270℃ using thermodynamic program Pandat™ as can be seen in Figure 4.3. The viscosity of suspension is 220 Pa·s from Equation (2), and the floating velocity of the Al powder is 2×10^{-5} mm/s from Equation (1). When mixing the Al powder in pure tin at 270℃, it could not be mixed and the Al powders became oxidized and blackened, and only the tin was solidified. However, when the Al powders were mixed into Sn-Zn30, it mixed well as shown in Figure 4.4.

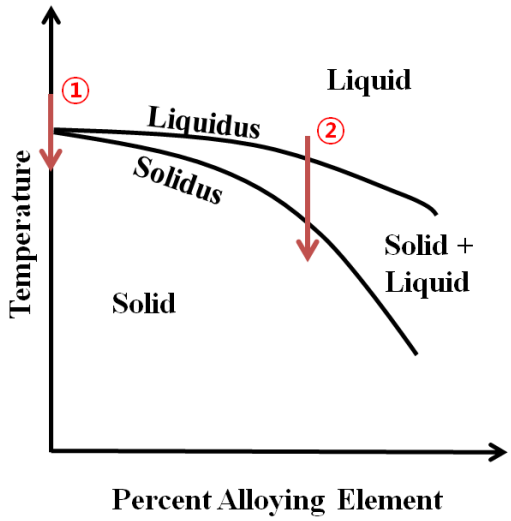

(a)

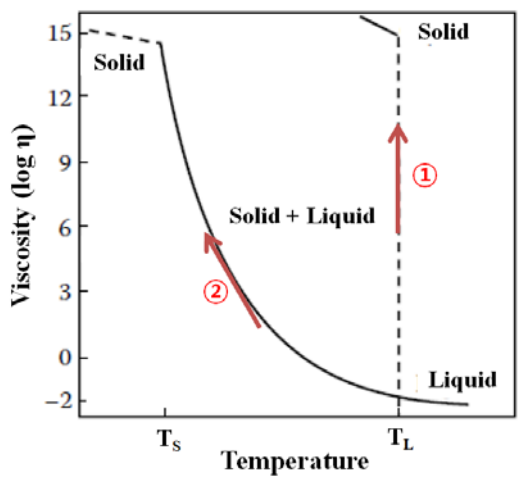

(b)

Figure 4.2. (a) Phase diagram of metal alloy, (b) viscosities of ① pure metal and ② metal alloy as a function of temperature.

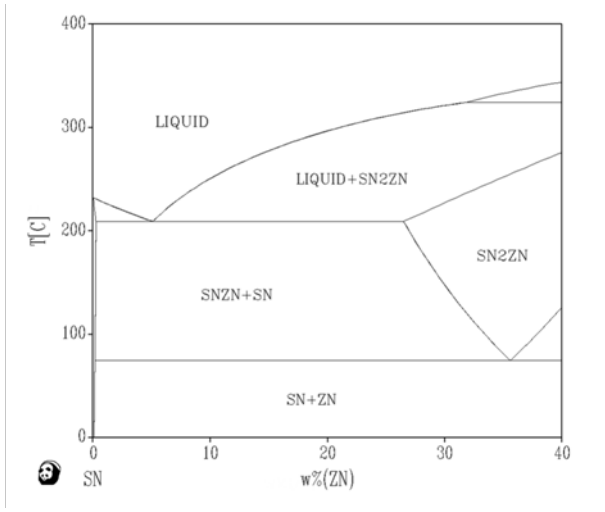

(a)

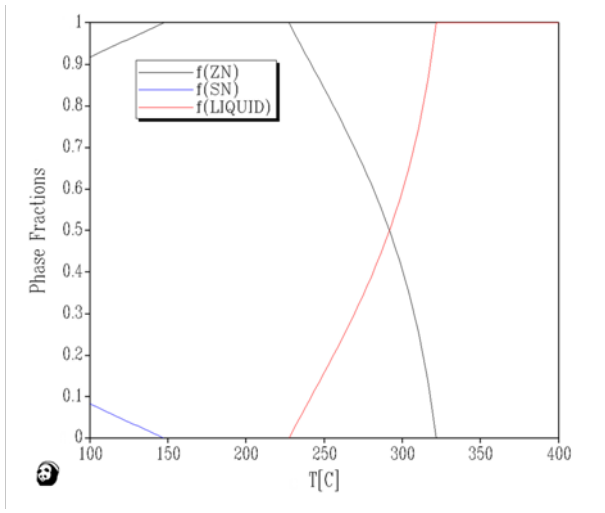

(b)

Figure 4.3. (a) Phase diagram of Sn-Zn, (b) phase fraction plot of Sn-Zn30 as a function of temperature.

(a)

(b)

Figure 4.4. Mixture after 10 min mixing under 50 rpm stirring: (a) pure tin and aluminum powder, (b) Sn-Zn30 and aluminum powder.

4.2.2 Preparation of composite samples

Composite samples were prepared through the processes in Figure 4.1. By stirring the Sn-Zn30 and Al powders with the ratio of 40 vol% and 60 vol% respectively at 50 rpm and 270℃ for 10 minutes, a cylindrical billet with a diameter of 76.2 mm and a height of 200 mm was molded. Afterwards, Sn-Zn30/elongated Al was extruded using a 600-ton extruder at 170℃ which is lower than the solidus temperature of Sn-Zn30. During the extrusions, the shape of the die was varied so that the metal fiber being generated through the extrusion process was made to have different lengths and cross-sectional shapes: circular diameter 24 mm, extrusion ratio 10; circular diameter 15.2 mm, extrusion ratio 25; and, rectangular width 26 mm, thickness 7 mm, extrusion ratio 25. The extrusion ratio is defined as the starting cross-sectional area divided by the cross-sectional area of the final extrusion. Figure 4.5 shows extrusion dies and the processing conditions and the densities of the Sn-Zn30/elongated Al prepared in such ways are organized in Table 4.1. It was found that lighter metal fillers (~4.5 g/cm^3) were fabricated than typical metal fillers (7-9 g/cm^3). Figure 4.6 shows that Al powders were elongated and thinned according to the increase in the extrusion ratio. In addition, when the shape of the extrusion die was rectangular, the width of the elongated Al increased and the thickness of the elongated Al decreased, in other words the elongated Al became flattened. From these results, it can be implied that the length of the elongated Al increases with increasing the extrusion ratio and the cross-sectional aspect ratio of the Al fiber increases using the rectangular die. Subsequently, Sn-Zn30/Al fiber filler was compounded with SAN for 5 minutes under the conditions of 270℃ at 50 rpm, using an internal mixer (HAAKE Polylab QC, Thermo Fischer Scientific, USA) with roller rotors. Samples were prepared varying the filler content of Sn-Zn30/elongated Al of 20, 40, and 60 vol%, respectively.

(a) (b) (c)

Figure 4.5. Extrusion dies: (a) circle (10), (b) circle (25), (c) rectangular (25).

Table 4.1. Processing conditions and densities of the metal fillers prepared.

Sn-Zn30/elongated Al code	Die shape	Extrusion ratio	Density (g/cm^3)
C10	Circle	10	4.48
C25	Circle	25	4.54
R25	Rectangular	25	4.55

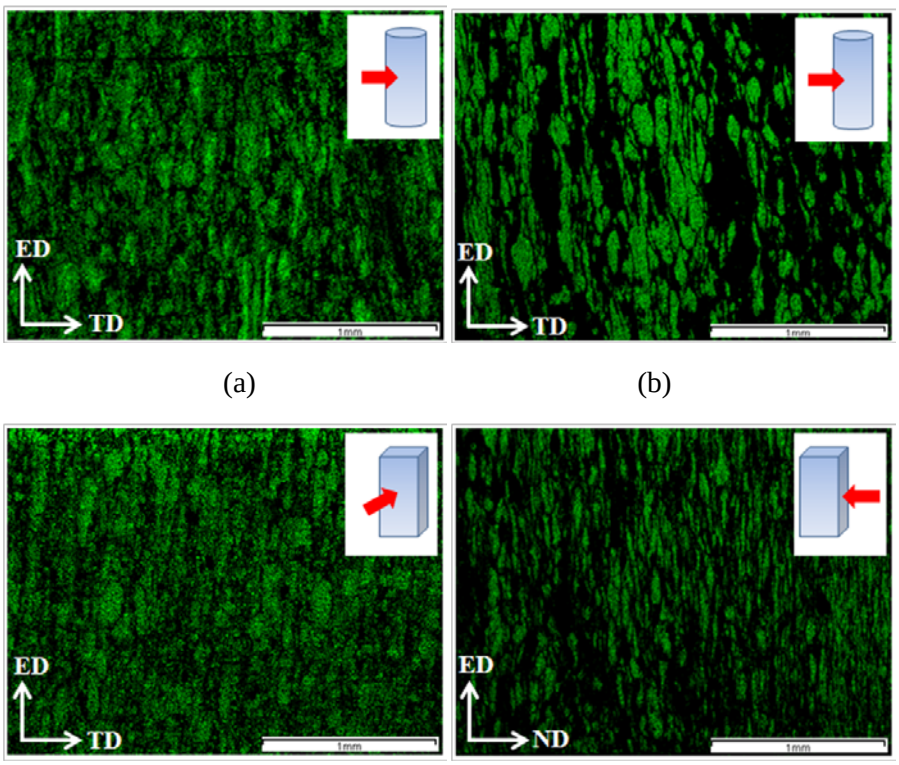

(a) (b)

(c) (d)

Figure 4.6. Aluminum (green color) EDS mapping results of extruded Sn-Zn30/elongated Al (red arrow is the direction of observation in inner picture); (a) C10, (b) C25, (c-d) R25.

And in order to see the effects of LMA on the processability, for comparative evaluation, Al powder 20, 40, and 60 vol% was compounded with SAN under the same conditions. Through hot pressing, composites and pure SAN (without fillers) produced in this way were made into a 150 mm×150 mm×3.2 mm plate, and from that, specimens were produced that had a standard dimension for measuring electrical properties and mechanical properties as shown Figure 4.7.

4.2.3 Measurements

The morphology of Sn-Zn30/Al fiber in SAN matrix was observed using field emission scanning electron microscopy (FE-SEM, SU-70, Hitachi, Japan) with energy dispersive spectroscopy (EDS, Hariba, Japan). The max torque was measured as the maximum value of torque on the rotors of the internal mixer during the compounding of each sample using the HAAKE Polysoft software package. For samples with an electrical conductivity higher than 10^{-7} S/cm, the electrical conductivity was measured by a four-point probe method at room temperature. The dimensions of the sample for electrical conductivity measurements were 60 mm×12.7 mm×3.2 mm. A constant current was applied using a source meter (2400, Keithley, USA) to the outer probes of the four contacts, and the corresponding voltage was measured between inner probes using a nanovolt meter (2182, Keithley, USA). For samples with an electrical conductivity lower than 10^{-7} S/cm, the measurements were performed by a two-point probe method using only a source meter. Electromagnetic interference shielding efficiency (EMI SE) of the composites at room temperature was measured using E8362B (Agilent, USA) according to the method described in ASTM D4935. Density was measured according to the ASTM D792 test method using a densimeter (Toyoseki, Japan). Notched Izod impact strength was measured according to the ASTM D256 test method (DG-1B, Toyoseki, Japan).

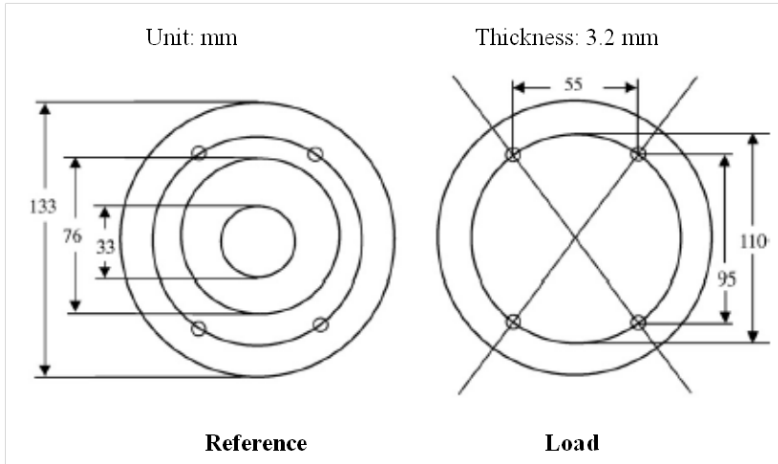

(a)

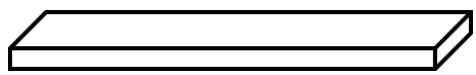

60 × 12.7 × 3.2 mm

(b)

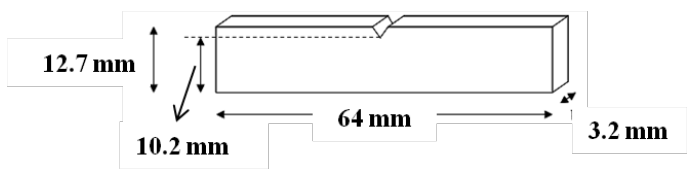

(c)

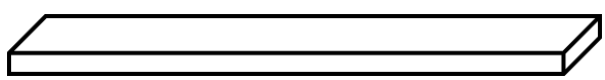

70 × 12.7 × 3.2 mm

(d)

Figure 4.7. Specimens for properties evaluation (a) EMI SE (b) electrical conductivity (c) notched Izod impact strength (d) flexural modulus

The thickness of the testing sample was about 3.2 mm. Three-point bending flexural modulus tests were conducted according to the ASTM D790 test method (UTM 3367, Instron, USA). The crosshead speed was 1.4 mm/min and the distance between the two bottom points was 50 mm. The typical dimensions of the sample beams were 70 mm×12.7 mm×3.2 mm.

4.3 Results and discussion

4.3.1 Max torque during compounding of SAN/Sn-Zn30/elongated Al composites

In order to estimate the effect of LMA on processability, the maximum value of torque on the screw of the Hakke mixer was measured during the compounding of each sample. Figure 4.8 shows a tendency for the max torque to increase as the metal filler content increased, indicating that the viscosity of the composite increases due to the metal filler. In the study of X. Zhang et al. [13], there was shown a decreasing tendency of viscosity while LMA content was increasing in polystyrene/Sn-Pb30 (Sn 70 wt% and lead (Pb) 30 wt%). While Sn-Pb30 was entirely liquid at the processing temperature of 190℃, Sn-Zn30 was coexisting with solid and liquid state and the elongated Al was solid at the processing temperature of 270℃, it was supposed that the viscosity of Sn-Zn30/elongated Al is higher than that of SAN. In addition, when the extrusion ratio was high, the max torque was slightly higher, indicating that the viscosity increased due to the extension in the excluded volume of the fiber as the length of fiber increased [14]. However, when the Sn-Zn30/elongated Al was used, it showed a significantly lower torque than using Al powders alone, indicating that the molten Sn-Zn30 mitigates the shear stress applied to the solid in the metal filler, lowers the viscosity of the metal filler, and improves the processability of the composite.

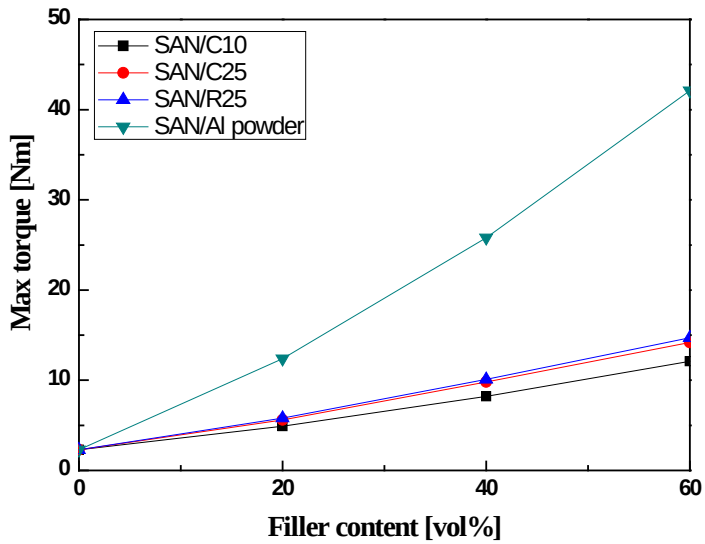

Figure 4.8. Max torque of the Hakke mixer during compounding of the SAN/Sn-Zn30/Al fiber composites.

4.3.2 Morphology of LMA/Al fiber in the SAN matrix

The morphology of Sn-Zn30/elongated Al in SAN matrix was observed using EDS. The elongated Al were wrapped around by Sn and Zn and well-dispersed as can be seen in Figures 4.9 - 4.17. Since the surface tension of Sn-Zn30 is much greater than that of SAN, a large domain must be formed through aggregating itself thermodynamically. However, the dispersibility of the metal filler improved because the solid Al played the role of physically helping the dispersion and slowing the rate of aggregation by increasing the viscosity of the filler within molten Sn-Zn30 [8]. The domains of the metal filler became elongated with the increase in the extrusion ratio of the Sn-Zn30/elongated Al, indicating that the domain shape of the filler can be controlled by the shape of elongated Al. When polymer/metal composites were prepared using LMA alone, the domains of LMA in the polymer/LMA composite generally formed large spherical droplet due to the surface tension of LMA, therefore the efficiency as conductive filler decreases [7]. In contrast, Sn-Zn30/elongated Al system can improve the efficiency as conductive filler by increasing the length of elongated Al. It can be believed that the efficiency as conductive filler relates to connectivity between metal fillers. When the extrusion ratio increased and/or the shape of the extrusion die was rectangular, as with samples C25 and R25, it can be observed that the connectivity improved since the specific surface area increased as the length and/or the cross-sectional aspect ratio of the elongated Al increased. In addition, although the domains of the metal filler became larger with increasing the filler metal content, the connectivity improved by maintaining the elongated domains due to the elongated Al. It can be concluded that the incorporation of the elongated Al is critical to dispersing the metal filler and improving the efficiency as conductive filler.

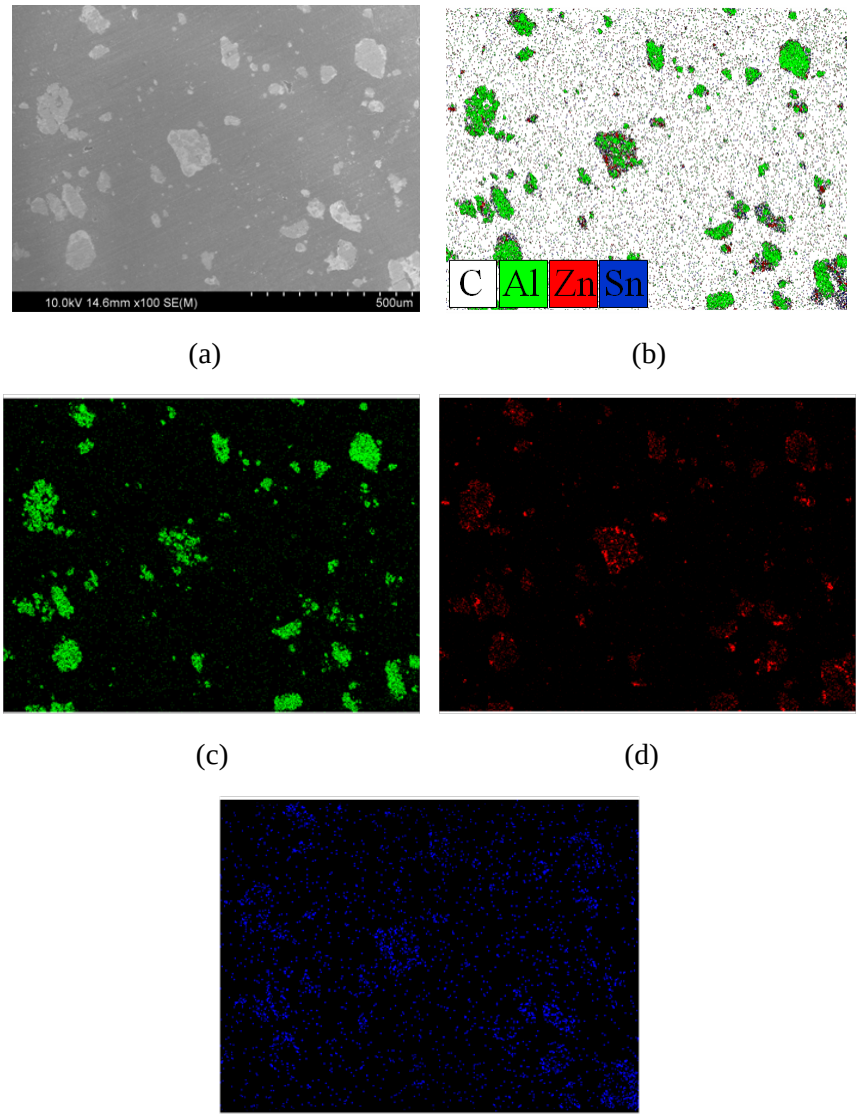

Figure 4.9. SEM and EDS mapping images of SAN/C10 20 vol%; (a) SEM image, (b) ESD image of mixed elements, (c) Al, (d) Zn,(e) Sn.

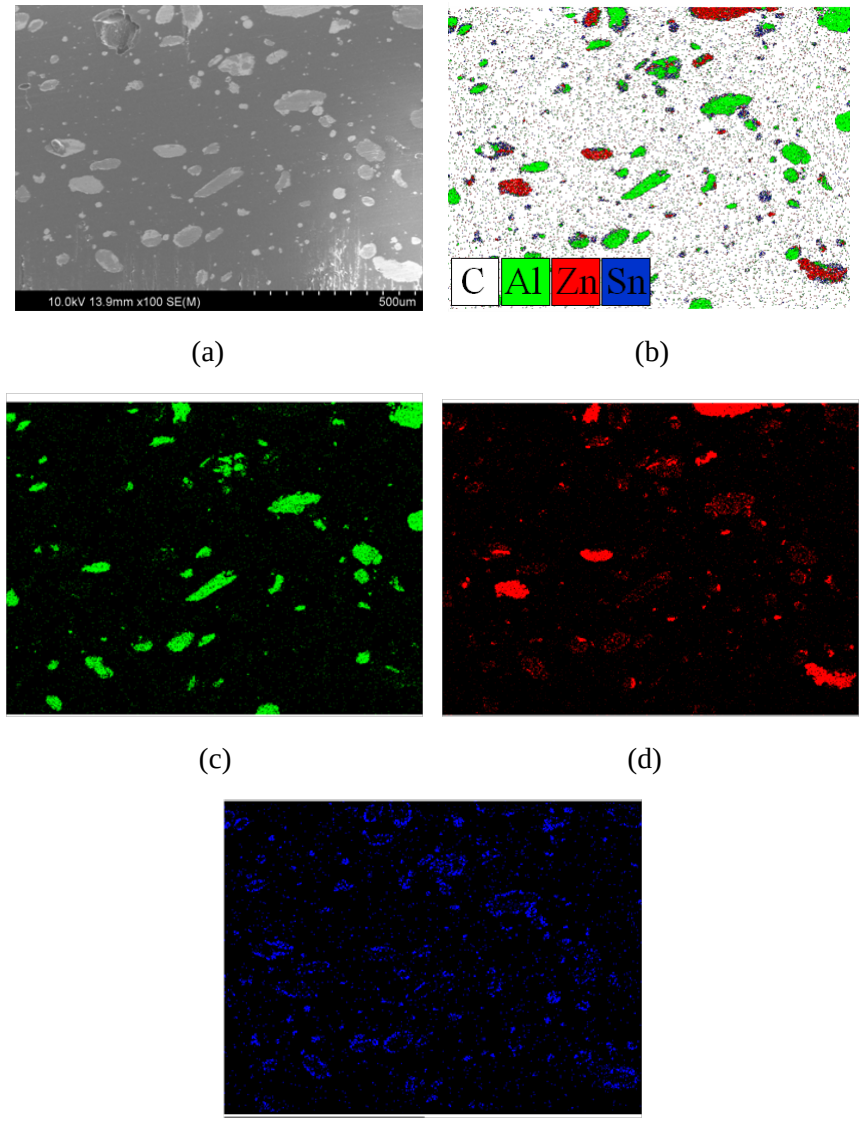

Figure 4.10. SEM and EDS mapping images of SAN/C25 20 vol%; (a) SEM image, (b) ESD image of mixed elements, (c) Al, (d) Zn,(e) Sn.

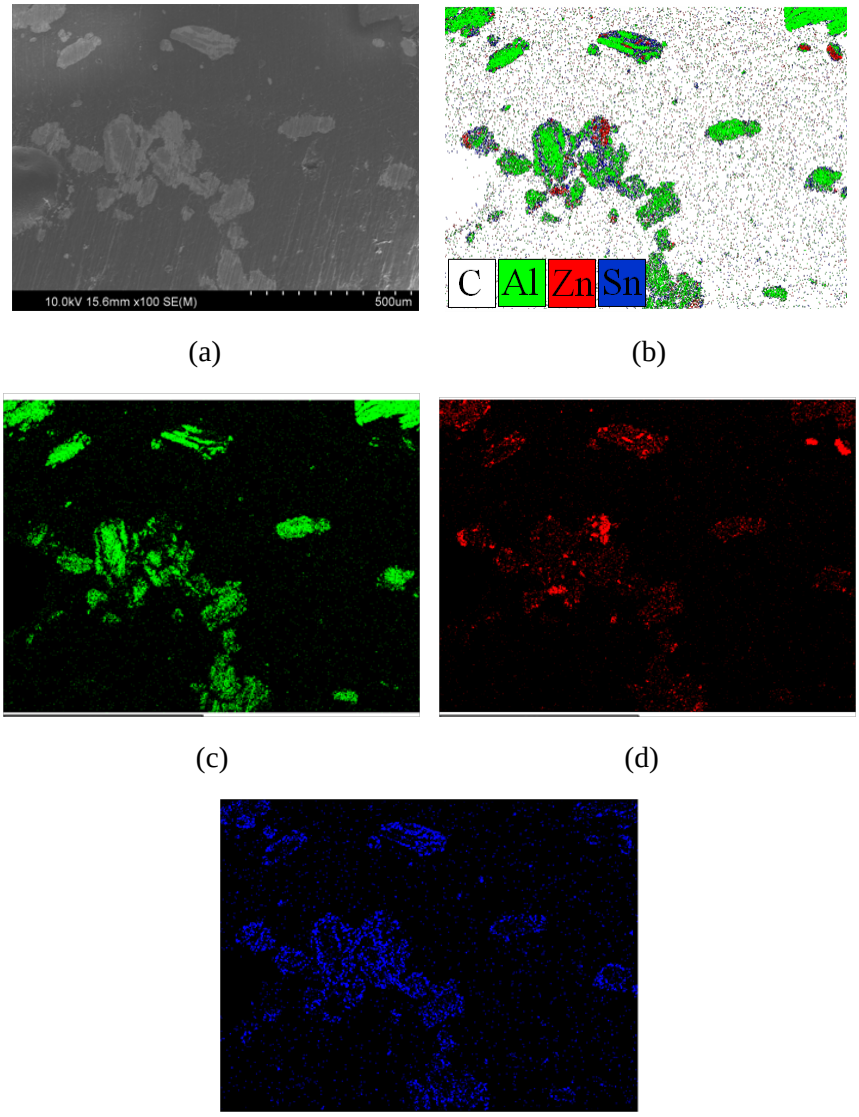

Figure 4.11. SEM and EDS mapping images of SAN/R25 20 vol%; (a) SEM image, (b) ESD image of mixed elements, (c) Al, (d) Zn,(e) Sn.

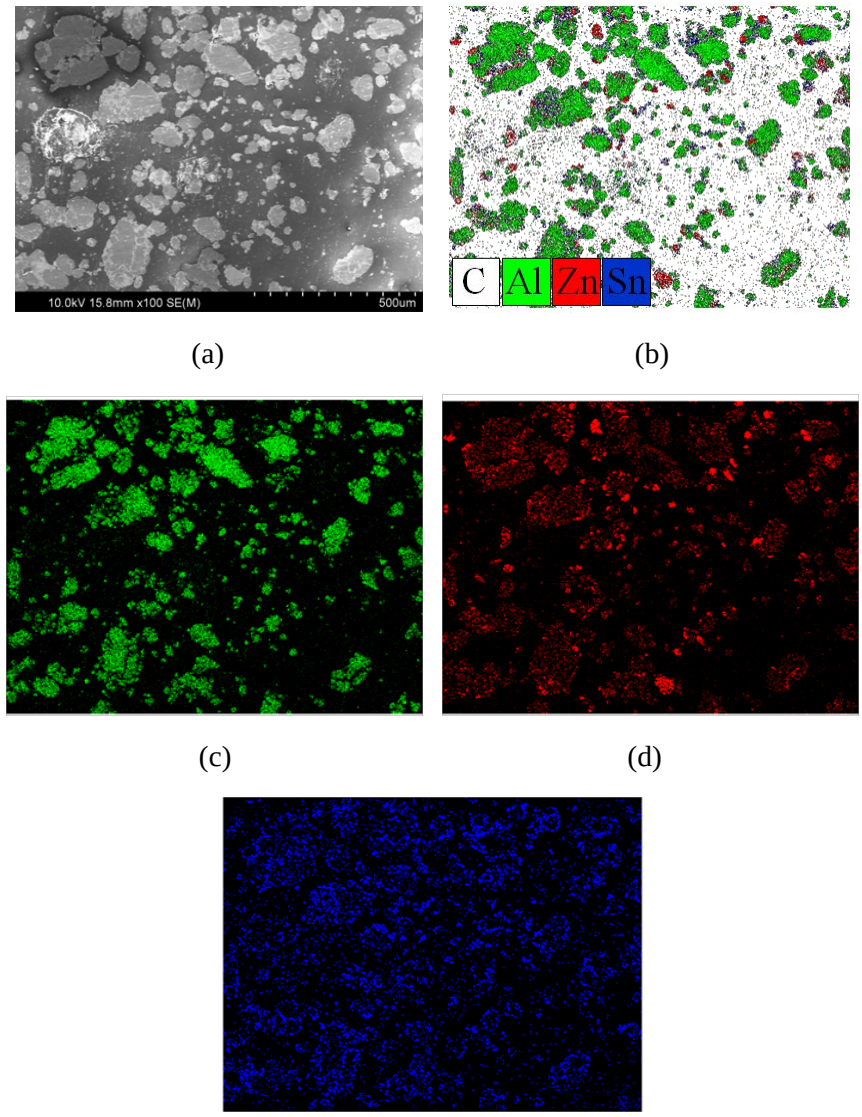

Figure 4.12. SEM and EDS mapping images of SAN/C10 40 vol%; (a) SEM image, (b) ESD image of mixed elements, (c) Al, (d) Zn,(e) Sn.

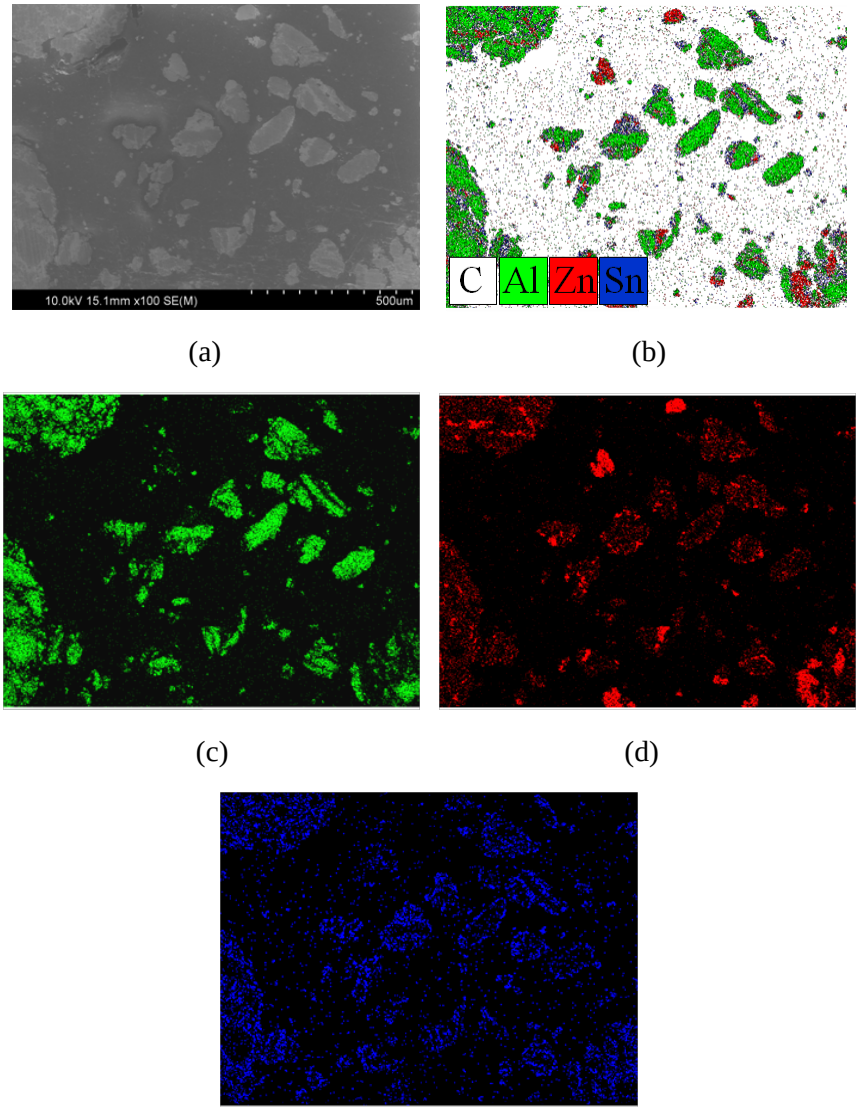

Figure 4.13. SEM and EDS mapping images of SAN/C25 40 vol%; (a) SEM image, (b) ESD image of mixed elements, (c) Al, (d) Zn,(e) Sn.

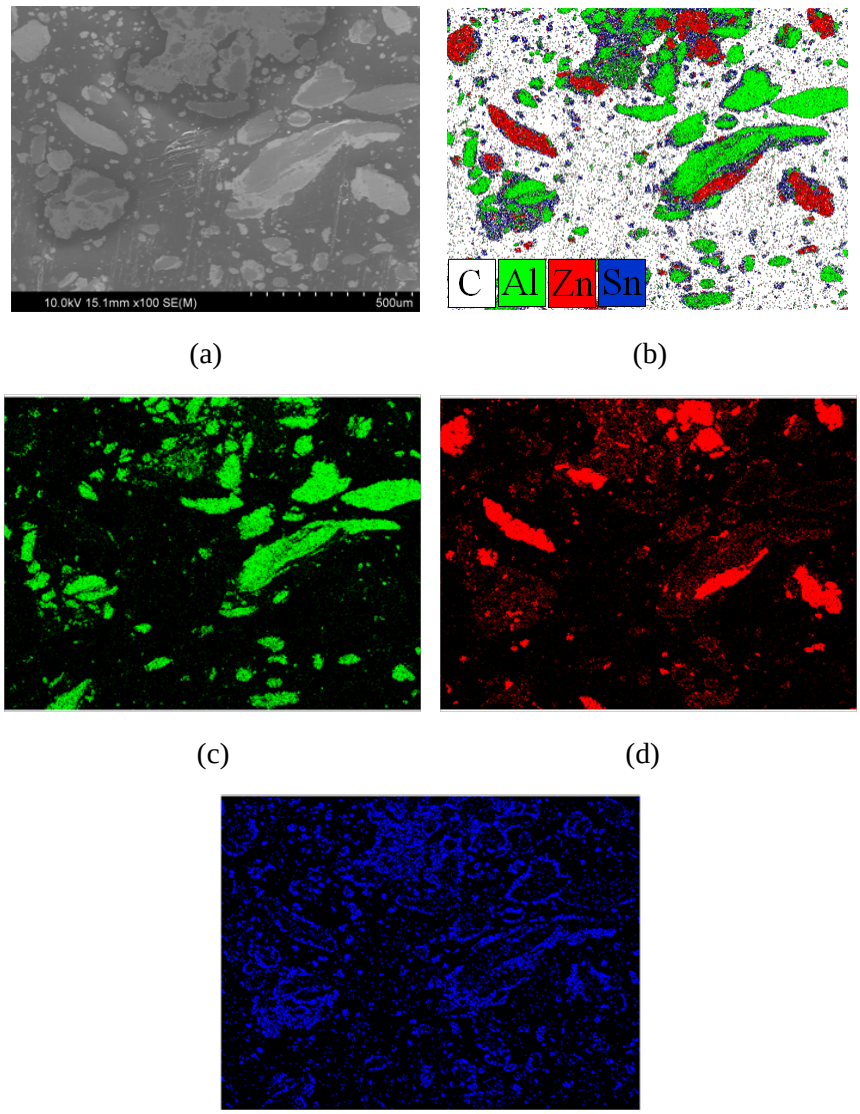

Figure 4.14. SEM and EDS mapping images of SAN/R25 40 vol%; (a) SEM image, (b) ESD image of mixed elements, (c) Al, (d) Zn,(e) Sn.

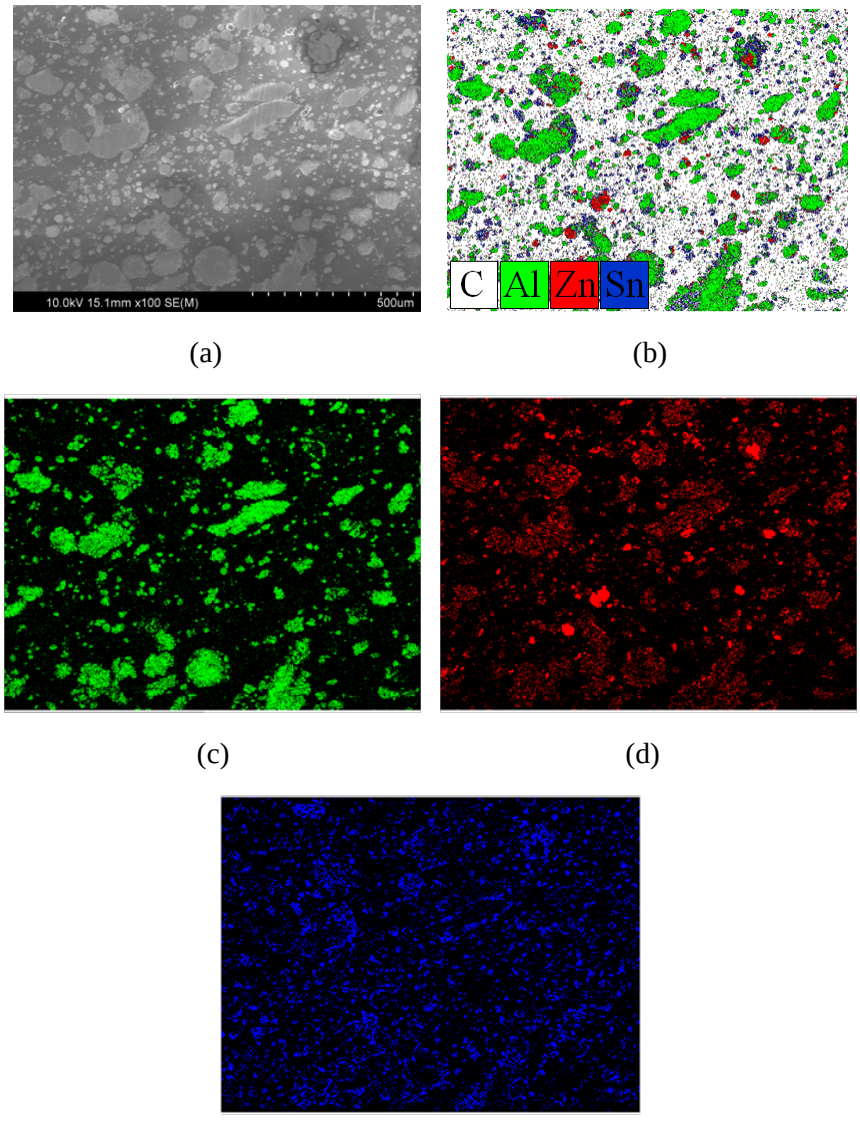

Figure 4.15. SEM and EDS mapping images of SAN/C10 60 vol%; (a) SEM image, (b) ESD image of mixed elements, (c) Al, (d) Zn,(e) Sn.

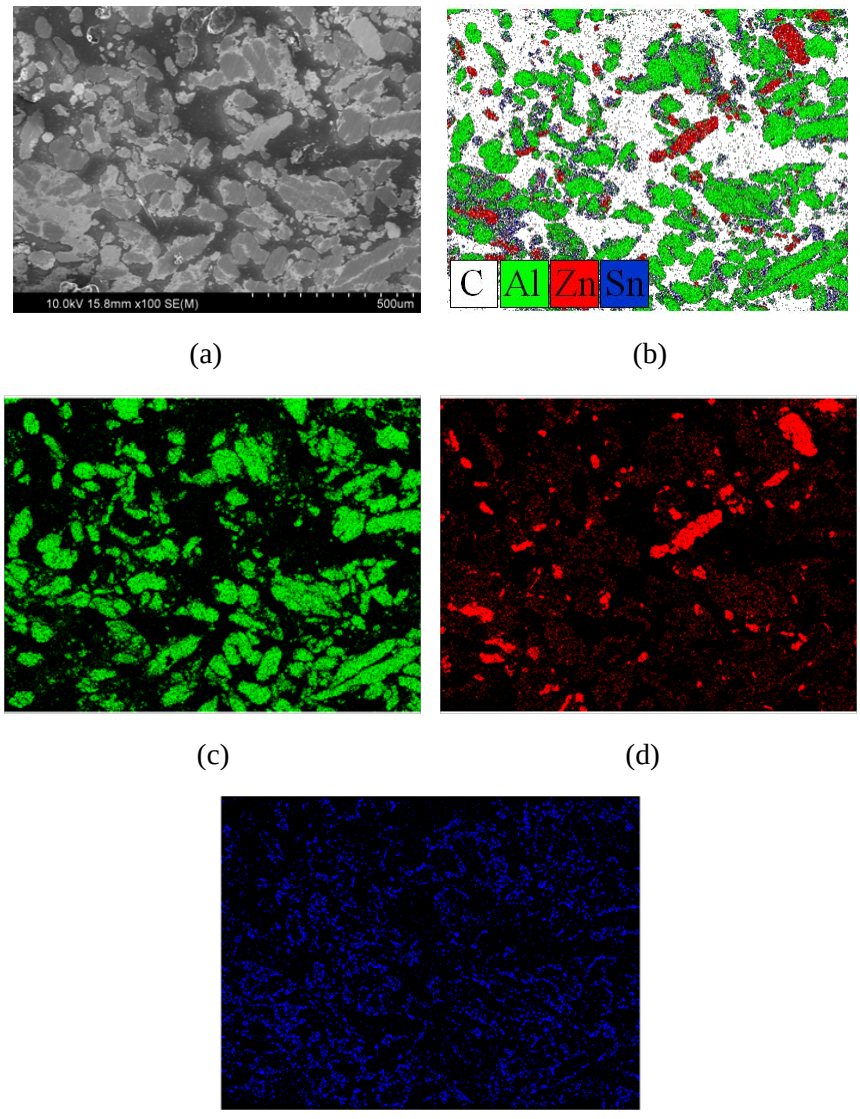

Figure 4.16. SEM and EDS mapping images of SAN/C25 60 vol%; (a) SEM image, (b) ESD image of mixed elements, (c) Al, (d) Zn,(e) Sn.

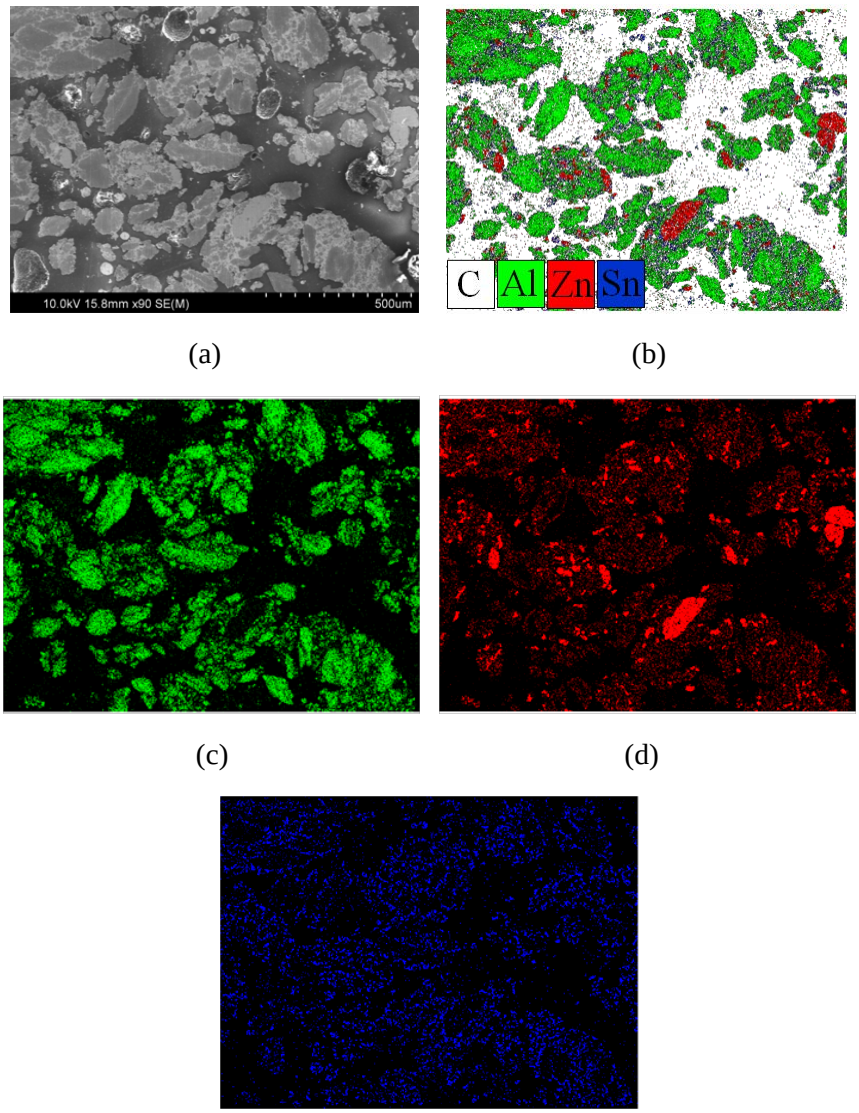

Figure 4.17. SEM and EDS mapping images of SAN/R25 60 vol%; (a) SEM image, (b) ESD image of mixed elements, (c) Al, (d) Zn,(e) Sn.

4.3.3 Electrical conductivity

Figures 4.9-4.17 showed that the connectivity between the metal fillers increased as the content of the metal filler, the length of elongated Al, and the cross-sectional aspect ratio of elongated Al increased. It is generally believed that the conductivity of the composite derives from the formation of a conducting network by the fillers in the matrix, and the increase of conductivity paths facilitates the improvement of the composite conductivity [15]. Such formation of a conducting network would improve the electrical conductivity of SAN/Sn-Zn30/elongated Al composites. Thus, Figure 4.18 shows that the electrical conductivities of the composites increased with increasing the filler content. The composites with filler at 20 vol% resulted in low conductivities of ~10^{-12} S/cm since the conducting networks were not formed, as shown in Figures 4.12-4.17. From filler content of 40 vol% and higher, the conductivities increased dramatically. In addition, the electrical conductivities of SAN/Sn-Zn30/C25 and R25 were higher than that of SAN/Sn-Zn30/C10 at the same filler content, indicating that as the domains are more elongated, the electrical conductivity increases due to improving the connectivity between the metal fillers. As the composites resulted in a good electrical conductivity, it is implied that the oxide layer on the surface of elongated Al could not impede the electrical conductivity due to the encapsulation of Sn-Zn30. For SAN/Sn-Zn30/R25, the electrical conductivity of 7900 S/cm was achieved at 60 vol% filler loading. This electrical conductivity is much higher than that (~10-15-10^{-8} S/cm) of polymer/LMA system [7, 16], higher than that (~10^{2} S/cm) of polymer/LMA/nickel particulate system [8], and lower than that (~10^{4} S/cm) of Polymer/LMA/copper fiber system [9]. It is found that the elongated Al is more effective than nickel particle due to the fiber shape and less than copper fiber due to the electrical conductivity itself.

Electromagnetic interference shielding efficiency (EMI SE) shows a similar tendency to the case of electrical conductivity in Figure 4.19. EMI SE can be divided into three elements as shown in Eqs. (3)-(6) [17];

$$\text{EMI SE} = \text{SE}_\text{R} + \text{SE}_\text{A} + \text{SE}_\text{MR} \tag{3}$$

$$\text{SE}_\text{R} = 20\log\frac{\text{Z}_0}{4\text{Z}_\text{s}} \tag{4}$$

$$\text{SE}_\text{A} = 20\log e^{d/\delta} \tag{5}$$

$$\text{SE}_\text{MR} = 20\log\left|1 - e^{-2d/\delta}\right| \tag{6}$$

where SE_R is the SE due to reflection, SE_A is the SE due to absorption, and SE_MR is the SE due to multiple reflections. Z_0 is the impedance of free space and Z_s is the impedance of the shielding material. d is the width of the medium and δ is the skin depth, of Eq. (7).

$$\delta = \frac{1}{\sqrt{\pi f \mu \sigma}} \tag{7}$$

f is the frequency of the EM wave, μ is the magnetic permeability of the medium, and σ is the electrical conductivity of the shielding material. If we assume that the shielding material is electrically conductive and the thickness of the shielding material is much thicker than the skin depth, the SE of multiple reflections can be ignored and Eqs. (3)-(6) become Eqs. (8) and (9).

$$\text{SE}_\text{R} = 39.5 + 10\log\frac{\sigma}{2\pi f \mu} \tag{8}$$

$$\text{SE}_\text{A} = 8.7d\sqrt{\pi f \mu \sigma} \tag{9}$$

As it can be seen in Equations (8) and (9), when electrical conductivity is increased SER and SEA are both increased and the total EMI SE is increased.

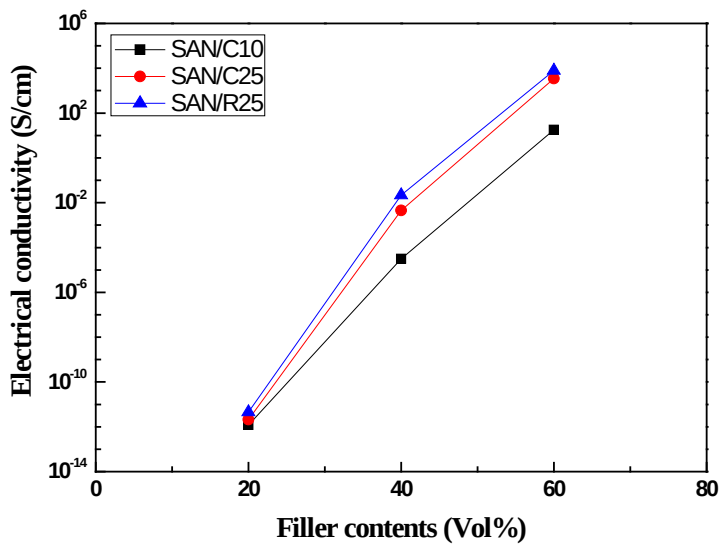

Figure 4.18. Electrical conductivity of SAN/LMA/elongated Al composites

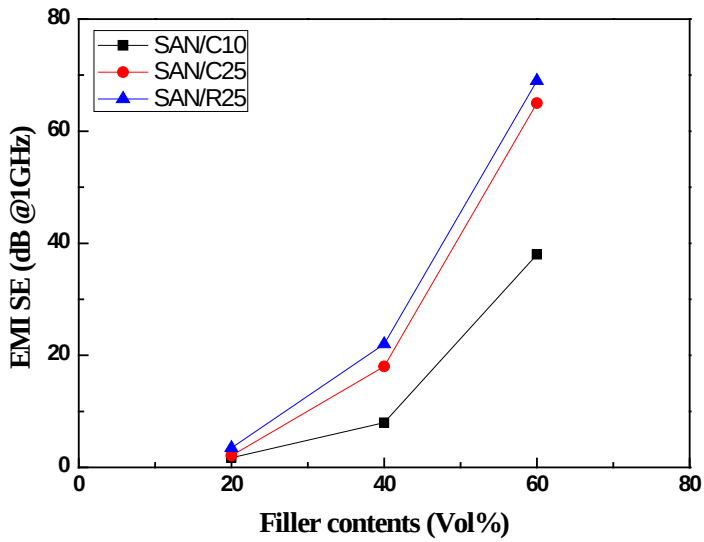

Figure 4.19. EMI shielding efficiency of SAN/LMA/elongated Al composites

4.3.4 Mechanical Properties

In order to evaluate the mechanical properties of SAN/Sn-Zn30/elongated Al composites, the notched Izod impact strength and the flexural modulus were measured. The impact strength of SAN decreases slightly with filler content of 20 vol%, but with the increase of filler content the impact strength was enhanced, as in Figure 4.20. In addition, when the extrusion ratio was increased and the shape of the extrusion die was rectangular, the growth rate was much larger. The fractured surfaces after notched Izod testing were observed through SEM as shown in Figure 4.21. It can be seen that the fracture occurred at the interface of SAN and metal filler. Since the interaction between SAN and metal filler is weak, the filler acts as a defect and reduces the notched Izod impact strength. In other words, the interfacial energy between SAN and metal filler would be a dominant factor for the impact strength of the SAN/Sn-Zn30/elongated Al composite [18]. When the length and the cross-sectional aspect ratio of the elongated Al are increased, the specific surface area of the metal filler domain will be increased more than the spherical filler domain, and this can contribute to the increase in impact strength by increasing the total interfacial energy. In addition, as the metal filler content increases, not only the surface area of the filler domain increases, but the connectivity between the metal fillers is increased, resulting in the enhancement of the impact strength.

The flexural modulus was increased as the filler content was increased, as shown in Figure 4.22. However, in contrast with the notched Izod impact strength, its growth rate was not as high even with the increase in the extrusion ratio, indicating that the flexural modulus follows the rule of mixture being influenced by the contents of the filler rather than the shape of the filler [19].

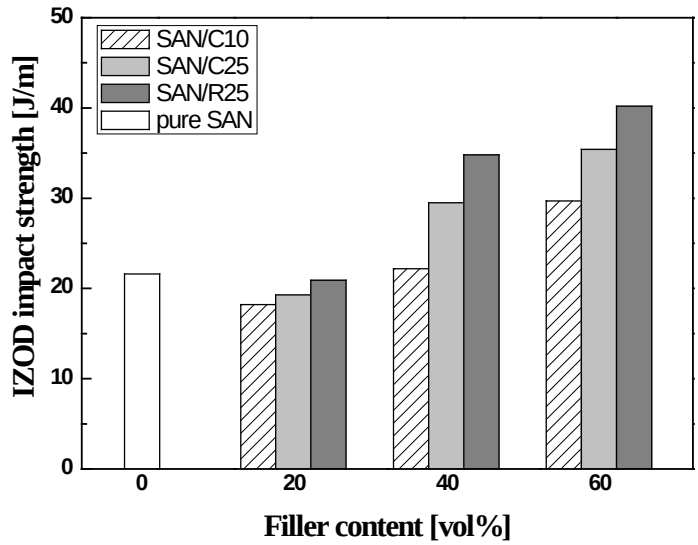

Figure 4.20. Notched Izod impact strength of the SAN/Sn-Zn30/elongated Al composites.

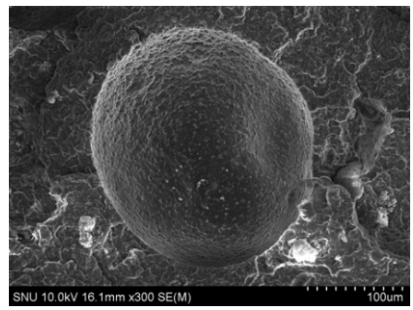

(a)

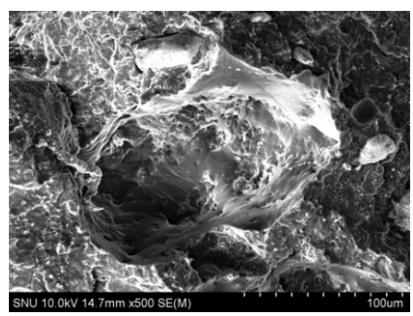

(b)

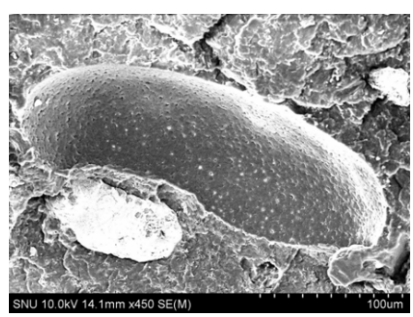

(c)

Figure 4.21. SEM images of the fractured surfaces of composites with the metal filler content of 20 vol%; (a) SAN/C10, (b) SAN/C25, (c) SAN/R25.

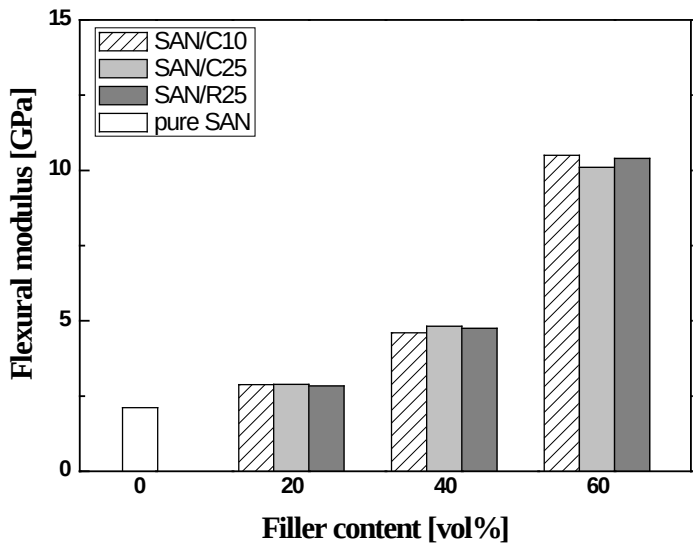

Figure 4.22. Flexural modulus of the SAN/Sn-Zn30/elongated Al composites.

4.4 Conclusions

I have established a novel method of fabricating metal filler with lightness and excellent electrical conductivity that can be compounded with polymer without degrading the processability. Using Sn-Zn30 having a coexisting region with liquid and solid at a mixing temperature, Sn-Zn30 and Al powders could be mixed. Through the cold extrusion of Sn-Zn30/Al powders, Sn-Zn30/elongated Al was fabricated to increase the efficiency as conductive filler. When Al powders were elongated, the oxidation layer of Al surface could become thin and/or be broken, resulting in the improvement of the wettability of Sn-Zn30 and Al. The results of EDS show that the elongated Al were wrapped around by Sn-Zn30 after compounding Sn-Zn30/elongated Al with polymer. When Sn-Zn30/elongated Al was compounded with polymer, the molten Sn-Zn30 maintained the processability, and the dispersibility of Sn-Zn30/elongated Al was improved due to the solid Al. As the shape of elongated Al was controlled by varying the extrusion conditions, it was found that electrical conductivity and the notched Izod impact strength are improved when the length and the cross-sectional aspect ratio of elongated Al increases. Furthermore, as Sn-Zn30/elongated Al (~4.5 g/cm^3) is relatively lighter than other LMA fillers (7-9 g/cm^3), the SAN/Sn-Zn30/elongated Al fiber composite (3.14 g/cm^3 at filler content of 60 vol%) is lighter than other polymer/LMA filler composites (5-6 g/cm^3 at same content).

Bibliography

[1] Bigg D. M.: Mechanical, thermal, and electrical properties of metal fiber-filled polymer composites. Polymer Engineering & Science, **19**, 1188-1192 (1979).

[2] Li Y. J., Xu M., Feng J. Q., Dang Z. M.: Dielectric behavior of a metal-polymer composite with low percolation threshold. Applied Physics Letters, **89**, 072902 (2006).

[3] Bloor D., Donnelly K., Hands P. J., Laughlin P., Lussey D.: A metal–polymer composite with unusual properties. Journal of physics D: Applied Physics, **38**, 2851-2860 (2005).

[4] Kumar A. M., Kwon S. H., Jung H. C., Shin K. S.: Corrosion protection performance of single and dual Plasma Electrolytic Oxidation (PEO) coating for aerospace applications. Materials Chemistry and Physics, **149-150**, 480-486 (2015).

[5] Song J. H., Nam K. S., Moon J. I., Choi Y. J., Lim D. Y.: Influence of the duty cycle on structural and mechanical properties of oxide layers on Al-1050 by a plasma electrolytic oxidation process. Metals and Materials International, **20**, 451-458 (2014).

[6] Zhang X., Pan Y., Shen L., Yi X.: Novel low melting point alloy-loaded polymer composite. II. Resistivity-temperature behavior. Journal of Applied Polymer Science, **77**, 756-763 (2000).

[7] Zhang X., Pan Y., Shen L., Zheng Q., Yi X.: A Novel low melting point alloy-loaded polymer composite. I. Effect of processing temperature on the electrical properties and morphology. Journal of Applied Polymer Science, **77**, 1044-1050 (2000).

[8] Mrozek R. A., Cole P. J., Mondy L. A., Rao R. R., Bieg L. F., Lenhart J. L.: Highly conductive, melt processable polymer composites based on nickel and low melting eutectic metal. Polymer, **51**, 2954-2958 (2010).

[9] Michaeli W., Pfefferkorn T. G.: Electrically conductive thermoplastic/metal hybrid materials for direct manufacturing of electronic components. Polymer Engineering and Science, **49**, 1511-1524 (2009).

[10] Batchelor G. K.: Sedimentation in a dilute dispersion of spheres. Journal of Fluid Mechanics, **52**, 245-268 (1972).

[11] Battezzati L., Greer A. L.: The viscosity of liquid metals and alloys. Acta Metallurgyica, **37**, 1891-1802 (1989).

[12] Thomas D. G.: Transport characteristics of suspension: VIII. A note on the viscosity of newtonian suspensions of uniform spherical particles. Journal of Colloid Science, **20**, 267-277 (1965).

[13] Zhang X., Pan Y., Cheng J., Yi X.: The influence of low-melting-point alloy on the rheological properties of a polystyrene melt. Journal of Materials Science, **35**, 4573-4581 (2000).

[14] Stary Z., Kruckel J., Weck C., Schubert D. W.: Rheology and conductivity of carbon fibre composites with defined fibre lengths. Composites Science and Technology, **85**, 58-64 (2013).

[15] Allaoui A., Bai S., Cheng H. M., Bai J. B.: Mechanical and electrical properties of a MWNT/epoxy composite. Composites Science and Technology, **62**, 1993-8 (2002).

[16] Bromashenko E., Sutovski S., Pogreb R., Sheshnev A., Bormashenko Y., Levin M., Westfrid A.: Development of novel binary and ternary conductive composites based on polyethylene, low-melting-point metal alloy and carbon black. Journal of Thermoplastic Composite Materials, **17**, 245-257 (2004).

[17] Al-Saleh M. H., Sundararaj U.: Electromagnetic interference shielding mechanisms of CNT/polymer composites. Carbon 47, 1738-1746 (2009).

[18] Wetzel B., Haupert F., Friedrich K., Zhang M. Q., Rong M. Z.: Impact and wear resistance of polymer nanocomposites at low filler content. Polymer Engineering & Science, **42**, 1919-1927 (2002).

[19] Thomason J. L., Vlug M. A.: Influence of fibre length and concentration on the properties of glass fibre-reinforced polypropylene: 1. Tensile and flexural modulus. Composites Part A: Applied Science and Manufacturing, **27**, 447-484 (1996).

Chapter 5. Conclusions

In this study, the effects of various factors on the electrical properties of the electrical conductive composites were investigated and the synergistic mechanisms of two kinds of fillers were identified. On the basis of these results, a new filler system was proposed, and the electrical conductive polymer composite can be fabricated with enhancement of the electrical and mechanical properties without degrading the processability of the composites.

The cause of differences in EMI SE of PA/CF and PC/CF composites according to their CF content was explored. As the CF content increased, EMI SE of PA/CF continuously increased but the increase in EMI SE of PC/CF slowed down from a CF content of 25 wt%. Theoretically electrical conductivity and magnetic permeability effect on EMI SE, the magnetic permeability of PA/CF is similar to that of PC/CF, however, the electrical conductivity of PA/CF is higher than that of PC/CF at CF content over 25wt%. The fiber length and fiber orientation structure within the composites were observed to identify the differences in the electrical conductivity increase in PA/CF and PC/CF. It was found that compared to PA/CF, PC/CF showed a shorter fiber length and fewer domains in which the fiber orientation was random, and this resulted in less electrical conductivity increase in PC/CF.

The CNT morphology of PA/CF/CNT composites was observed to study the synergistic effect of CF and CNT, which are different in terms of their compatibility with the matrix, with regard to electrical conductivity. It is found that PU-CNT, which had better compatibility with the matrix within the composites than N-CNT, formed larger agglomerates. Moreover, their impregnation with the matrix was better as well, resulting in better electrical properties and mechanical properties than those of the composites with N-CNT. Moreover, CNT had a larger effective volume than CF, such that CNT helped improve the formation of

conductive network of CF, thereby generating a synergistic effect when CNT and CF were mixed together. As the CF content increased, the CNT distribution was improved owing to the increase of the matrix viscosity and the physical contact between CF and CNT agglomerates, thereby increasing the synergistic effect of CF and CNT. In other words, PU-CNT, which had good dispersibility, produced a synergistic effect even at a small CF content; as the CF content increased, this synergistic effect increased. N-CNT, which had low dispersibility, had a minimal synergistic effect when the CF content was small; however, as the CF content increased, the synergistic effect was produced as soon as the N-CNT dispersibility improved.

A novel method of fabricating metal filler has been established with lightness and excellent electrical conductivity and it can be compounded with polymer without degrading the processability. I designed an LMA that can impregnate light metal powder and extruded the mixture of LMA/light metal powder into LMA/elongated light metal. When this metal filler is compounded with polymer, the LMA becomes melted without worsening the processability and the dispersibility of the metal filler is improved as it contains the solid light metal. As the shape of the elongated light metal was controlled by varying the extrusion conditions, it was found that electrical conductivity and the notched Izod impact strength are improved when the length and the cross-sectional aspect ratio of elongated light metal increases.

초 록

최근 전자책, 스마트폰, 평판 TV 및 디지털 카메라 같은 IT 기기들이 박막화 및 집적화 되고, 자동차에도 여러 전자기기들을 탑재함으로써 전자기파 간섭 및 전자기파 인체 유해성이 이슈화 되고 있다. 금속 소재의 경우 전기 전도성과 전자기파 차폐 성능이 우수하지만 고비중이며 재료의 가공에 드는 비용과 복잡한 성형이 힘들어 디자인에 제약을 갖는 단점이 있다. 고분자의 경우 경량성과 가공용이성 등의 장점이 있지만, 일반적으로 전기적 성질이 없기 때문에 그 사용이 제한되고 있다. 고분자에 전기 전도성과 전자기파 차폐성을 부여하는 경우가 고분자의 적용영역을 획기적으로 넓히는 데 있어 그 중요성이 매우 크다 하겠다.

고분자에 전기적 성질을 부여하는 방법의 하나로 절연성인 고분자에 전기적 성질이 있는 충진제를 복합화 함으로써 고분자 복합체가 전기적 성질을 가지게 하는 방법이 있다. 전기 전도성 충진제로 알루미늄, 구리, 니켈, 은, 스테인레스 스틸 등의 금속계 충진제와 흑연, 탄소 섬유, 탄소 나노튜브 등의 탄소계 충진제로 구분할 수 있다. 금속계 충진제의 경우 자체적으로 높은 전기적 물성을 가지지만 알루미늄을 제외하고는 고분자 대비 비중이 매우 높아 부품의 무게를 증가시키는 문제점이 있다. 그리고 알루미늄의 경우 표면에 밀한 산화층이 형성되어 있는데 알루미늄의 산화나 부식을 막는 역할을 하지만 고분자와의 복합화가 가능한 크기가 작은 알루미늄 입자에서는 전자의 흐름을 방해하여 충진제의 효율을 떨어뜨리는 문제점이 있다. 탄소계 충진제로 흑연이나 탄소 섬유의 경우 사용 가능한 비중과 전기적 물성을 지니는 장점이 있지만 많은 함량을 넣을 경우 점도가 상승하여 공정성이 나빠지고

복합체의 충격 강도 등의 기계적 물성을 떨어지는 문제점이 있다. 최근에 연구가 활발하게 이루어지고 있는 탄소 나노튜브는 나노 수준의 직경과 큰 종횡비로 적은 함량을 넣어도 큰 효과를 볼 수 있지만, 높은 원가와 반데르 발스 힘 때문에 고분자 기지 내에 분산이 잘 되지 않는 문제점이 있다.

고분자 기지의 특성을 최대한 유지하면서 전기적 성질을 부여하기 위해서는 최소의 함량으로 최대의 효과를 내는 충진제의 효율화가 중요하다 할 수 있다. 이러한 충진제의 효율화를 향상시키기 위해서는 충진제가 전기적 물성을 구현하는 기구를 이해하고 충진제의 각 요소들이 전기적 물성에 미치는 효과를 파악하여야 한다. 또한, 충진제들을 혼용하였을 때 얻게 되는 상승효과와 그 효과 발현 기구에 대한 이해 역시 충진제의 효율을 증가시키는 데 중요한 요소라 할 수 있다. 이에 고분자/탄소 섬유 복합체에 대한 실험을 통해 전기적 성질 발현 기구에 대해 연구하였으며, 고분자/탄소 섬유/탄소 나노튜브 복합체에 대한 실험을 통해 충진제 상승효과 기구에 대한 연구를 진행하였다. 이를 바탕으로 고분자/전도성 충진제 복합체의 공정성을 훼손시키지 않으면서 전기적 성질이 우수한 고분자/저융점 금속/경량 금속 섬유 복합체를 새로이 고안한 연구를 진행하였다.

먼저 폴리아미드/탄소 섬유와 폴리카보네이트/탄소 섬유 복합체를 탄소 섬유 함량에 따라 제조하여 전자기파 차폐성을 관측하였는데, 폴리아미드/탄소 섬유 복합체의 경우 탄소 섬유의 함량이 증가함에 따라 전자기파 차폐성이 일정하게 증가하는 반면, 폴리카보네이트/탄소 섬유 복합체의 경우 탄소 섬유 함량이 증가함에 따라 전자기파 차폐성이 증가하나 탄소 섬유 함량이 일정 함량 이상에서는 그 증가폭이 감소하는 현상을 확인하였다. 이론적으로 물질의 전기 전도도는 전자기파 반사

차폐성과 흡수 차폐성 모두 증가시키는 효과가 있지만 물질의 투자율의 경우 전자기파 반사 차폐성을 감소시키고 흡수 차폐성을 증가 시키는 특성이 있다. 이에 두 복합체들의 전기 전도도와 투자율을 측정하여 이론적 수식을 통해 각각이 미치는 효과를 보았는데, 폴리카보네이트/탄소 섬유 복합체가 폴리아미드/탄소 섬유 복합체 대비 탄소 섬유 함량이 높을 경우 전기 전도도가 낮아 이와 같은 현상이 발생한 것으로 판단하였다. 이에 두 복합체의 전기 전도도에 영향을 미치는 요소로 탄소 섬유의 길이와 배향 구조에 대한 연구를 진행하였다. 폴리카보네이트가 폴리아미드보다 높은 용융 점도를 가지기 때문에 전단 응력에 의해 탄소 섬유의 단사가 더 많이 발생하여 복합체내의 잔류 탄소 섬유의 길이가 짧은 것을 확인하였다. 그리고 복합체 시편 내부에 탄소 섬유들이 표면 부분에서는 시편 성형시 흐름방향으로 배향되나, 중심 부분에서는 흐름방향에 수직하여 배향되는 것을 확인하였다. 이러한 탄소 섬유 배향 구조가 고분자 기지의 용융 점도와 유리 전이 온도에 의해 다르게 나타났는데, 폴리카보네이트/탄소 섬유 복합체가 폴리아미드/탄소 섬유 복합체 대비 용융 점도와 유리 전이 온도가 높아 탄소 섬유가 배향되는 정도가 더 강하고 그 변화도 급격하여 무질서한 배향을 이루고 있는 영역이 더 적었다. 탄소 섬유의 배향이 무질서할 경우 탄소 섬유 간의 접촉이 더 잘 이루어져 전기 전도도가 향상되는데 폴리카보네이트/탄소 섬유 복합체는 폴리아미드/탄소 섬유 복합체 대비 그 영역이 적어 전기 전도도가 낮은 것으로 사료된다. 이러한 탄소 섬유 길이와 배향 구조가 전기전도도에 미치는 영향성을 기존의 모델들을 통해 파악하고자 하였으나 정확히 일치하는 모델이 없었다. 이에 연속 몬테카를로 전산모사를 통해 탄소 섬유 길이, 배향, 함량 등의 인자가 탄소 섬유 연결에 미치는 영향을 파악하였다.

다음으로 고분자/탄소 섬유/탄소 나노튜브 복합체에 관한 연구를 통해 상승효과의 기구를 파악하였다. 이 연구에서 폴리아미드 기지와 친화성이 있는 물질인 폴리우레탄으로 사이징한 탄소 나노튜브와 아무런 처리를 하지 않은 탄소 나노튜브 두 종류를 사용하였다. 사이징한 탄소 나노튜브의 경우 사이징 하지 않은 탄소 나노튜브보다 더 크고 성긴 상을 이루고 있었으며, 전기 전도도 역시 우수하였다. 퍼컬레이션 이론을 통해 탄소 나노튜브의 퍼컬레이션 임계 함량을 계산하였는데 이론치보다 매우 낮은 값을 보이는 것으로 보아 탄소 나노튜브의 경우 전자 도약 현상에 의해 실제 크기보다 더 큰 효과 부피를 갖는 것으로 판단된다. 이러한 큰 효과 부피를 통해 탄소 섬유와의 혼용에 있어 전도 연결 구조를 형성하는데 도움을 주어 상승효과가 발생하는 것으로 사료된다. 또한 탄소 섬유의 함량이 증가함에 따라 탄소 나노튜브의 분산성이 향상되는데 이는 탄소 섬유에 의한 고분자 기지의 점도 상승 및 탄소 섬유와 탄소 나노튜브의 물리적 접촉에 의한 것이다. 이러한 탄소 나노튜브의 큰 효과 부피에 의한 전도 연결 구조 형성을 용이하게 하는 효과와 탄소 섬유에 의한 탄소 나노튜브의 분산성 향상의 효과에 의해 상승효과가 발생하는 것을 밝혀내었다.

마지막으로 신규 고분자/저융점 금속/신장된 경량 금속 복합체에 관한 연구를 진행하였다. 저융점 금속이 고분자와의 복합화시 용융되어 흐름으로써 점도 향상을 막아 공정성을 유지하고 경량 금속으로 사용한 알루미늄의 표면을 감싸 알루미늄 표면의 산화층이 전기 전도를 방해하지 못하도록 하여 충진제의 전기 전도성을 향상시키는 역할을 하며, 신장된 경량 금속은 저비중으로 충진제의 비중을 낮추고 섬유상을 띰으로써 큰 비표면적을 가져 충진제의 효율을 증가시킴과 동시에 고분자와의 복합화시 용융된 저융점 금속 내에서 고상으로 존재함으로써

저융점 금속이 뭉치는 현상을 방해하여 분산성이 향상되도록 하는 역할을 하도록 이러한 시스템을 고안하였다. 대표적인 저융점 금속인 주석을 알루미늄 분말과 혼합하였는데 큰 비중 차에 의해 혼합이 불가능하였다. 이에 혼합시 액상 저융점 금속의 점도를 상승시키기 위해 혼합 온도인 230도에서 액상-고상 공역을 갖도록 주석-아연30 합금을 디자인하여 알루미늄 분말과 혼합에 성공하였다. 이렇게 제조한 주석-아연30/알루미늄 분말을 냉각 압출을 통해 주석-아연30/신장된 알루미늄 충진제를 제조하였는데, 압출비와 다이 형태를 다르게 하여 신장된 알루미늄의 길이, 단면 효과를 보고자 하였다. 이를 함량에 따라 폴리스타이렌아크릴로나이트릴과 복합화하였으며, 복합화 과정에서 고상 금속 분말을 적용한 경우보다 로터에 걸리는 토크가 낮은 것을 통해 공정성을 훼손하지 않음을 확인하였다. 충진제의 함량이 증가할수록, 압출비가 증가할수록, 섬유 단면이 이형성을 띨 수록 충진제의 연결성이 좋아지는 것을 주사전자현미경을 통해 관찰하였으며, 이러한 효과에 의해 전기 전도도와 전자기파 차폐성이 향상되었다. 또한 동일한 경향성으로 충격 강도의 향상이 있었는데 이는 비표면적의 증가로 인한 표면 에너지 증가에 기인한 것으로 판단된다.

본 연구를 통해 충진제의 전기적 물성 발현에 미치는 요소들을 파악하고 새로운 모델을 제시하였으며, 서로 다른 충진제를 혼용하였을 때 발생하는 상승효과에 대한 기구를 규명하였다. 이를 바탕으로 신규 충진제 시스템을 고안하였으며, 이를 통해 전기적 물성과 기계적 물성이 우수한 고분자 복합체를 복합화하였다.

주요어: 고분자, 충진제, 탄소 섬유, 탄소 나노튜브, 저융점 금속, 경량 금속 섬유, 전자기파 차폐, 전기 전도성
학 번: 2012-30160